Study of CdTe/$Mg_xCd_{1-x}Te$ Double Heterostructures and Their Application in High Efficiency Solar Cells and in Luminescence Refrigeration

by

Xinhao Zhao

A Dissertation Presented in Partial Fulfillment
of the Requirements for the Degree
Doctor of Philosophy

Approved November 2016 by the
Graduate Supervisory Committee:

Yong-Hang Zhang, Chair
Shane Johnson
Zachary Holman
Srabanti Chowdhury
Ximin He

ARIZONA STATE UNIVERSITY

December 2016

ABSTRACT

$CdTe/Mg_xCd_{1-x}Te$ double heterostructures (DHs) have been grown on lattice-matched InSb (001) substrates using Molecular Beam Epitaxy. The $Mg_xCd_{1-x}Te$ layers, which have a wider bandgap and type-I band edge alignment with CdTe, provide sufficient carrier confinement to CdTe, so that the optical properties of CdTe can be studied. The DH samples show very strong Photoluminescence (PL) intensity, long carrier lifetimes (up to 3.6 μs) and low effective interface recombination velocity at the $CdTe/Mg_xCd_{1-x}Te$ heterointerface (~1 cm/s), indicating the high material quality. Indium has been attempted as an n-type dopant in CdTe and it is found that the carriers are 100% ionized in the doping range of 1×10^{16} cm^{-3} to 1×10^{18} cm^{-3}. With decent doping levels, long minority carrier lifetime, and almost perfect surface passivation by the $Mg_xCd_{1-x}Te$ layer, the $CdTe/Mg_xCd_{1-x}Te$ DHs are applied to high efficiency CdTe solar cells. Monocrystalline CdTe solar cells with efficiency of 17.0% and a record breaking open circuit voltage of 1.096 V have been demonstrated in our group.

$Mg_{0.13}Cd_{0.87}Te$ (1.7 eV), also with high material quality, has been proposed as a current matching cell to Si (1.1 eV) solar cells, which could potentially enable a tandem solar cell with high efficiency and thus lower the electricity cost. The properties of $Mg_{0.13}Cd_{0.87}Te/Mg_{0.5}Cd_{0.5}Te$ DHs and solar cells have been investigated. Carrier lifetime as long as 0.56 μs is observed and a solar cell with 11.2% efficiency and open circuit voltage of 1.176 V is demonstrated.

The $CdTe/Mg_xCd_{1-x}Te$ DHs could also be potentially applied to luminescence refrigeration, which could be used in vibration-free space applications. Both external luminescence quantum efficiency and excitation-dependent PL measurement show that the

best quality samples are almost 100% dominated by radiative recombination, and calculation shows that the internal quantum efficiency can be as high as 99.7% at the optimal injection level (10^{17} cm^{-3}). External luminescence quantum efficiency of over 98% can be realized for luminescence refrigeration with the proper design of optical structures.

This work is dedicated to my parents, Baohai Zhao and Shumin Shi, and my girlfriend Xinmeng Wang, who have always been supportive to me over the years.

ACKNOWLEDGEMENTS

First of all, I am very grateful for the guidance provided by my professor Dr. Yong-Hang Zhang over the last 5 years. He is very open minded and gives me flexibility on my research. At the same time, he is also prudent and rigorous, which helps to drive me towards perfection so that I can fully achieve the most significant results from many of our research projects. I would also like to thank Dr. Su Lin who spent a lot of time helping me get started with time-resolved photoluminescence measurements. I am also thankful to all the previous and current group members, Dr. Michael DiNezza, Dr. Shi Liu, Dr. Xiao-Meng Shen, Zhi-Yuan Lin, Zhao-Yu He, Jacob Becker, Yuan Zhao, Ying-Shen Kuo, Calli Campbell, Maxwell Lassise, Cheng-Ying Tsai et al, who are dedicated and hardworking, without whom I could never achieve so many important results.

This work was partially supported by Air Force Office of Scientific Research (Grant No. FA9550-12-1-0444), Science Foundation Arizona (Grant No. SRG 0339-08), National Science Foundation (Grant No. 1002114), Department of Energy (DOE) FPACE II program (Contract No. DE-AC36-08GO28308), and DOE/Bay Area Photovoltaic Consortium program (Award No. DE-EE0004946).

TABLE OF CONTENTS

Page

CHAPTER Page

LIST OF TABLES

Table Page

LIST OF FIGURES

Figure Page

Figure Page

Figure Page

Figure Page

Figure Page

Figure Page

Chapter 1

INTRODUCTION

1.1 History of CdTe Solar Cell

A complete review of the history of CdTe solar cell can be found in Ref. [1]. Here a shorter review is given, with a focus based on our own studies. CdTe is an ideal material for solar cell applications. It has a direct bandgap of 1.50 eV, which is an excellent match to our sun which has an effective black-body temperature of 5700 K. CdTe also has a large absorption coefficient which enables its application in thin film solar cells. The large absorption coefficient, for photons with $E > E_g$ translates into 99% absorption of the absorbable AM1.5G photons within 2 μm of film thickness. The record CdTe solar cell efficiency of 22.1% was demonstrated by First Solar in February 2016 [2]. However, the Shockley-Queisser limit of CdTe is much higher, ~ 32% under AM1.5G spectral radiation based on detailed balance model [3], which means that there is still much room for improvement.

CdTe was first proposed for photovoltaic solar energy conversion by Loferski in 1956 [4]. Some early work demonstrated p-n homojunction cells with efficiency up to 10.5% [1]. Following that, CdTe solar cells have been widely investigated using heterojunction structures since 1960, proceeding along two paths, according to CdTe's conductivity type (n and p-type). For n-type CdTe absorbers, extensive work was carried out on heterojunctions with p-type Cu_2Te. However, due to the difficulty in controlling the Cu_2Te formation process, poor device stability in Cu_2Te/CdTe cells, and a lack of a transparent p-type conductor, the research ultimately shifted to heterojunction structures employing a p-type CdTe absorber.

P-type CdTe single-crystal heterojunction solar cells were investigated in the 1970s and 80s using p-type CdTe wafers, and stable oxides such as In_2O_3:Sn (ITO), ZnO, SnO_2 and CdS. In 1987, Nakazawa reported cells made by reactive deposition of In_2O_3 on p-type CdTe (111) wafers with an efficiency of 13.4%, V_{oc}=892 mV, J_{sc}=20.1 mA/cm^2, and FF=74.5% [5]. The efficiency of 13.4% was also the highest reported for single-crystal CdTe solar cells. The CdTe wafer surface was treated (etched in bromine methanol) prior to loading into vacuum for In_2O_3 deposition, which is believed to be the key factor that improved the interface quality between CdTe and In_2O_3 and thus the cell efficiency.

Despite the extensive studies with p-type heterostructure single-crystal CdTe solar cells, little subsequent work has been reported since the 1990s. Meanwhile, the research on thin-film p-type heterojunction CdTe solar cells were advancing fast, with n-CdS/p-CdTe being the most studied CdTe solar cell heterostructures. Thin-film CdS/CdTe solar cells have been fabricated in two different configurations, referred to as substrate and superstrate structures. In a substrate structure, CdTe was deposited onto a suitable substrate and followed by the deposition of CdS and TCO layers. In a superstrate structure, TCO, CdS and CdTe are sequentially deposited onto a glass substrate. The glass substrate not only acts as a mechanical supporting layer, but also as a window layer to allow light to enter the solar cell. In the 1980s and 1990s, the thin-film CdS/CdTe superstrate solar cell was improved by refinements in device design, post deposition treatment and the formation of low-resistance contacts. It was found that the CdTe cell performance was greatly enhanced, after being coated with $CdCl_2$, followed by a post deposition air-heat treatment. In 1993, cell efficiency of 15.8% was reported by J. Britt and C. Ferekides [6], with post deposition heat treatment using $CdCl_2$ and graphite paste containing Hg as the back contact. The

V_{oc}=0.8429 V, J_{sc}=25.09 mA/cm^2, and FF=74.48%. With further refinement in the window-layer and employing vapor $CdCl_2$ treatment, additional improvement was made by Wu, with 16.5% efficiency, V_{oc}=0.845 V, J_{sc}=25.9 mA/cm^2, and FF=75.5% [7-8].

1.2 Recent Progress and Challenges

The record efficiency of CdTe solar cells has been increasing rapidly in the past few years, from 17.3% in 2011 to 22.1% in 2016 [9], which was mainly pushed forward by First Solar and GE Global Research. The highest efficiency cell uses the traditional CdS/CdTe combination on a superstrate structure. Over the years, the short circuit current of CdTe solar cells has improved significantly, while the open circuit voltage remains almost unchanged [10]. This has been the biggest challenge for CdTe solar cells. The low open circuit voltage, about 0.5 V below the bandgap, is a result of the poor material quality of polycrystalline CdTe. Table 1.1 below lists the performance of the record efficiency CdTe solar cells from the past 2 decades.

Table 1.1. The Performance of Record Efficiency CdTe Solar Cells from the Past 2 Decades. Data from Ref. [10-12].

Year	**Team**	**Efficiency (%)**	**V_{oc} (mV)**	**J_{sc} (mA/cm^2)**	**FF (%)**
1993	USF	15.8	843	25.1	74.5
1997	Matsushita	16	840	26.1	73.1
2001	NREL	16.4	848	25.9	74.5
2001	NREL	16.7	845	26.1	75.5
2011	FSLR	17.3	845	27	75.8

2012	GE	18.3	857	27	79
2013	FSLR	18.7	852	28.6	76.7
2013	FSLR	19	872	28	78
2013	GE	19.6	857.3	28.59	80
2014	FSLR	21	875.9	30.25	79.4

There are a few ways of improving the open circuit voltage [13]. One is to improve the minority carrier lifetime in polycrystalline CdTe, which is now on the order of only a few nanoseconds. It is also important to understand the recombination mechanisms (or carrier loss mechanisms) in a solar cell structure, that can decrease the minority carrier lifetime. For example, the recombination inside the CdTe grain or at the grain boundaries, the recombination near the CdTe/back contact interface, and the recombination at the CdS/CdTe p-n junction interface. Another challenge is the p-type doping in traditional CdS/CdTe superstrate solar cells. In this cell structure, the CdTe absorber only has around 2×10^{14} cm^{-3} p-type background doping concentration, which prevents the formation of high built-in voltage between CdS and CdTe. Higher p-type doping concentrations are needed, while maintaining good material quality (with decent carrier lifetimes) to ensure the highest internal quantum efficiency. The third challenge is to find a surface passivation layer for the CdTe absorber. The surface passivation layer can be either between the CdS/CdTe interface or between the CdTe/back contact interface, to reduce the surface recombination of CdTe.

In this dissertation, although the traditional CdS/CdTe superstrate cell structure was not studied directly, the problems associated with it were overcame and understood by

studying mono-crystalline CdTe/$Mg_xCd_{1-x}Te$ DHs on lattice-matched InSb (001) substrates. The carrier lifetime of monocrystalline CdTe achieved (on the order of a few microseconds) is much longer than that of polycrystalline materials, due to its much lower defect density and the almost perfect surface passivation by $Mg_xCd_{1-x}Te$ [14-17]. The interface recombination, and the thermionic emission and tunneling effects at the CdTe/$Mg_xCd_{1-x}Te$ interface are now well understood [17]. The CdTe/$Mg_xCd_{1-x}Te$ DHs are also doped n-type with In, and its optical properties are studied for the design of solar cells. The carrier lifetimes are decent (~100 ns) with moderate doping levels (10^{16} cm^{-3} - 10^{17} cm^{-3}), which are beneficial for high efficiency solar cells [18]. With a decent carrier lifetime, moderate doping level and surface passivation, a CdTe solar cell based on CdTe/$Mg_xCd_{1-x}Te$ DHs was demonstrated with 17.0% efficiency, which is the highest ever for monocrystalline CdTe solar cells [19]. The open circuit voltage of 1.096 V for this device is the highest for any CdTe solar cells reported at the time of writing, and it is very possible that with better window layer designs and improved short circuit current, greater than 22% efficient cells can be made.

1.3 Market Share of CdTe Solar Cell

Photovoltaic (PV) energy is becoming a more and more important energy source with each passing year. In Germany, PV covered 7% of the total electricity demand in 2014 and in the US, about 1% of the total electricity is contributed by PV. With many different types of solar cells in the research community, the PV market however is dominated by only three of them, i.e. thin film, mono-Si, and multi-Si solar cells, with Si solar cells contributing around 90% of the market [20]. In thin film solar cells, there are three types

of cells: CdTe, CIGS and a-Si solar cells, and the percentage of the thin-film solar cell market share has not changed much since 2000, since the total market is also growing fast. However, the CdTe and CIGS solar cells are playing a bigger and bigger role in the thin film PV market, while the market share of a-Si solar cells is declining [20].

Today CdTe solar cells have become the third most abundant PV technology in the world marketplace after mono- and multi-crystalline silicon. CdTe thin-film solar cells can be manufactured quickly and inexpensively, providing a lower-cost alternative to conventional silicon-based technologies. The performance of the CdTe solar cell is also already competitive with other PV technologies. The current record efficiency for a laboratory CdTe solar cell is 22.1% by First Solar, while First Solar recently reported its record module efficiency to be 18.6% [21].

Chapter 2

CDTE/MG_XCD_{1-X}TE DOUBLE HETEROSTRUCTURES: GROWTH AND CHARACTERIZATION

2.1 Growth Optimization: Molecular Beam Epitaxy

$CdTe/Mg_xCd_{1-x}Te$ double heterostructures (DHs) are grown on InSb (001) substrates using Molecular Beam Epitaxy (MBE), and a schematic diagram of the samples is shown in Fig. 2.1. The bandgap energy vs. lattice constant diagram is shown in Fig. 2.2 [22]. It is found that CdTe is closely lattice-matched to the InSb substrate, and thus high quality CdTe eiplayers can be grown with minimum dislocation densities. MgTe is also relatively lattice-matched to CdTe and InSb. It also has a much wider band gap and is in type-I band alignment with CdTe, which can provide sufficient carrier confinement for CdTe [23]. A schematic band edge diagram is shown in Fig. 2.3. The study of different recombination mechanisms in the DH will be discussed in the next chapter.

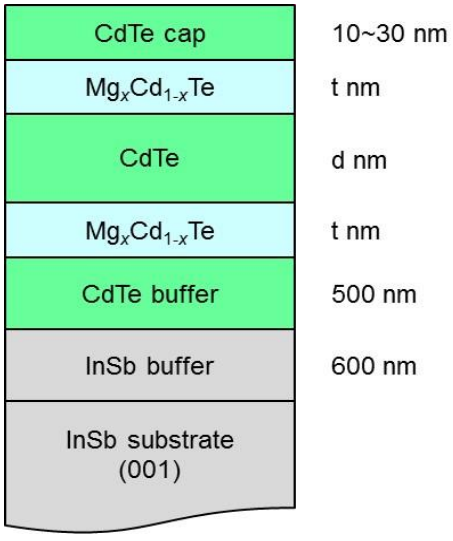

Fig. 2.1. Sample Structure of $CdTe/Mg_xCd_{1-x}Te$ Double Heterostructures.

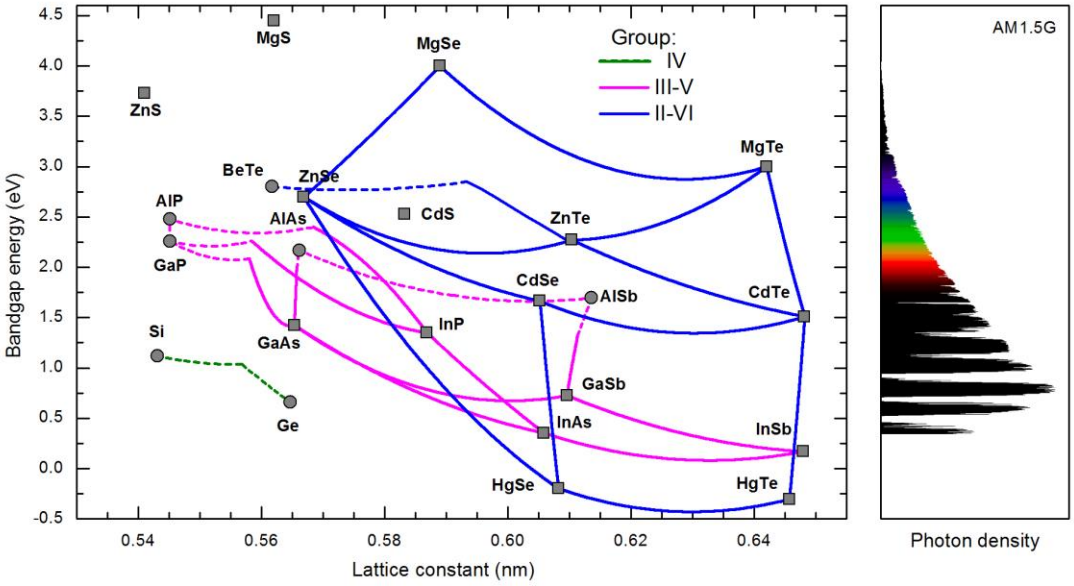

Fig. 2.2. Bandgap Energy vs. Lattice Constant for Different Semiconductors [22].

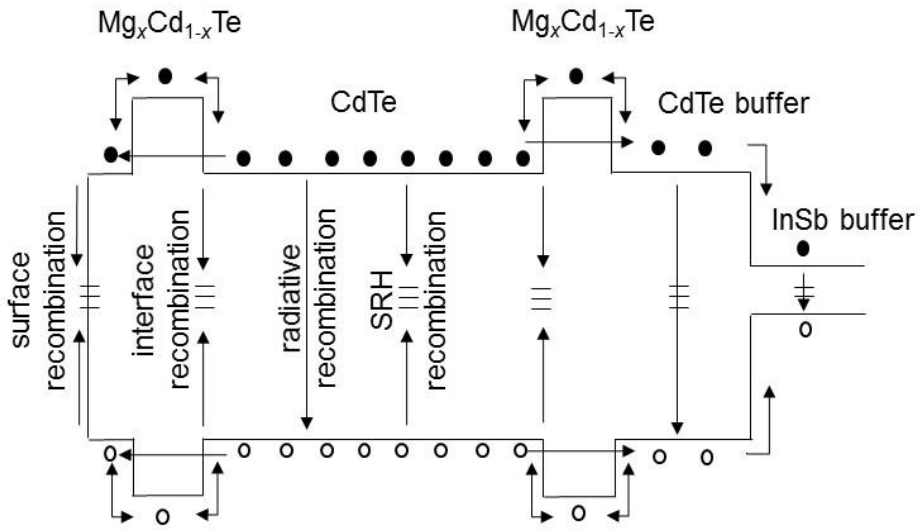

Fig. 2.3. Schematic Band Edge Alignment for CdTe/$Mg_xCd_{1-x}Te$ Double Heterostructures. The Solid and Open Circles Represent Excess Electrons and Holes Respectively When the Samples Are Excited by a Laser. Different Recombination Processes Are Also Shown.

The growth of CdTe/$Mg_xCd_{1-x}Te$ DHs is carried out using a dual-chamber VG V80H MBE system equipped with two separate III-V and II-VI growth chambers and an ultrahigh vacuum (UHV) transfer chamber as shown in Fig. 2.4. The purity of all source materials is at least 7N, with the exception of Mg which is 6N. Effusion cells are used for the group-II materials, and a valved effusion cell is used for Te. The surface reconstruction during growth is monitored by reflection high energy electron diffraction (RHEED), and the substrate temperature is measured using a 1550 nm infrared pyrometer for the InSb wafers. RHEED oscillations observed during the growth of CdTe are used to calibrate the 1:1 Cd/Te flux ratio based on the saturation of the growth rate with increasing Cd flux [14].

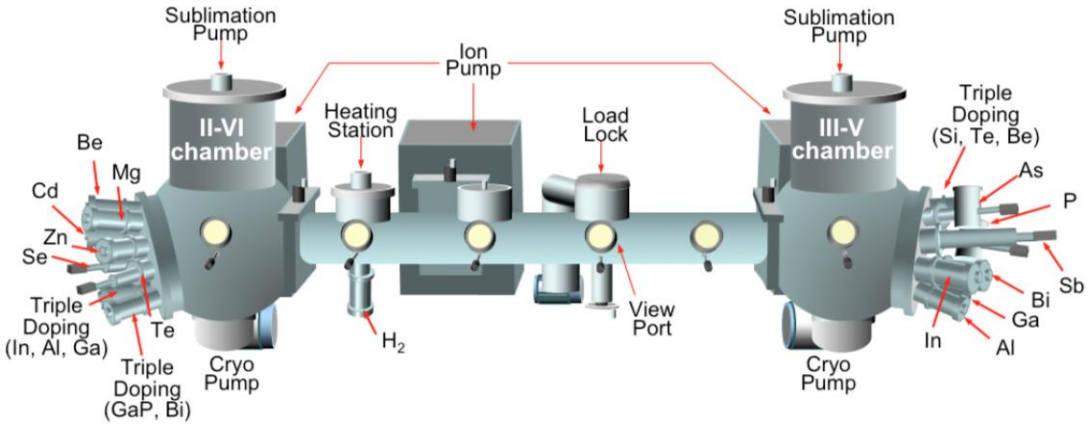

Fig. 2.4. The Lay-out of the Dual Chamber MBE System

The growth procedure starts with thermal deoxidation of the InSb substrates in the III-V chamber under a group-V overpressure, followed by the growth of a 500 nm thick InSb buffer layer. The substrate temperature and Sb/In flux ratio are 390 ˚C and 1.5 respectively for the growth of InSb layers, and streaky RHEED reconstructions are observed. Then the

samples are transferred directly to the II-VI growth chamber under UHV after the InSb buffer layer growth. Immediately prior to CdTe growth, InSb surfaces are exposed to a Cd flux for several minutes to prevent the formation of a group III-VI alloy at the interface. A CdTe buffer layer is then grown using an initial Cd/Te flux ratio of 3.5 in order to further prevent the formation of In_3Te_2 at the interface. After 2 mins of growth, the flux ratio is then reduced to 1.5. Upon initiation of CdTe growth on InSb, the RHEED pattern becomes slightly hazy as the surface reconstruction transitions from InSb to CdTe. After 10 min of growth the pattern becomes streaky. Both (2×1) and c(2×2) RHEED reconstructions are observed which indicate a Cd-rich growth condition. The optimal substrate temperature is 265 ˚C and the growth rate is 9.6 nm/min. as determined by RHEED oscillations. The Cd and Te fluxes are kept constant during the $Mg_xCd_{1-x}Te$ layer growth, since Mg has a larger sticking coefficient and will displace the excess Cd [14].

The growth conditions for the CdTe epilayers were optimized by trying different flux ratios and substrate temperatures, as summarized in Table 2.1. Fig. 2.5 and Fig. 2.6 show the PL intensity and minority carrier lifetime of CdTe/$Mg_{0.24}Cd_{0.76}Te$ DHs as a function of substrate temperature and the Cd/Te flux ratio, respectively. It is found that when the substrate temperature is at 265 ˚C and the flux ratio is 1.5, both PL intensity and the carrier lifetime are maximized, indicating the highest material quality.

Table 2.1. Growth Conditions Attempted for CdTe Epilayers.

Cd/Te Flux Ratio	**Substrate temperature (°C)**				
	235	250	265	280	295
1.8			X		
1.5	X	X	X	X	X
1.2			X		

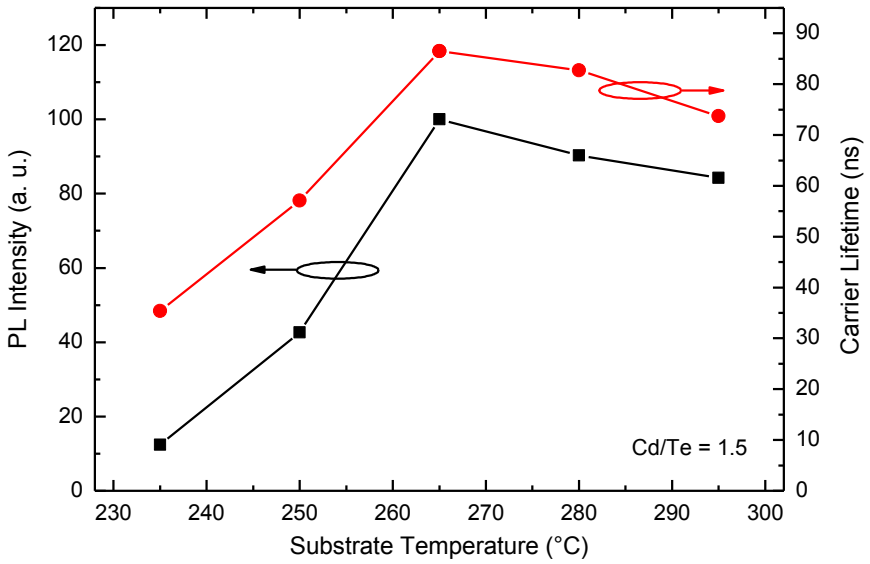

Fig. 2.5. Photoluminescence Intensity and Minority Carrier Lifetime vs. Substrate Temperature. The Cd/Te Flux Ratio Is Fixed at 1.5.

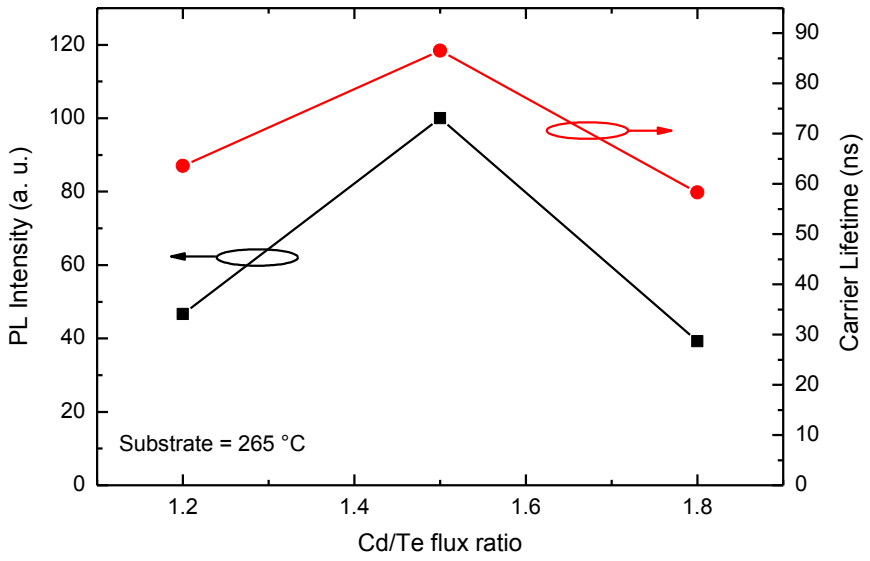

Fig. 2.6. Photoluminescence Intensity and Minority Carrier Lifetime vs. Cd/Te Flux Ratio. The Substrate Temperature Is Fixed at 265 ˚C.

2.2 High Resolution X-Ray Diffraction

High Resolution X-Ray Diffraction (HRXRD) is an efficient way of determining the composition, strain and layer thickness of single crystalline semiconductor materials. It can also be used to evaluate the crystalline qualities with a diffraction peak's intensity and Full-Width at Half Maximum (FWHM) [24]. It is called "high-resolution" for the following reasons: 1). a monochromator is used in front of the X-ray source, so that the incident beam is monochromatic and parallel; 2). A monochromator is also placed in front the X-ray detector (triple axis detector), so that the receiving angle is limited; 3). The sample stage (goniometer) and detector has high precision during the angular movement (0.0001˚). A schematic diagram is shown in Fig. 2.7. In the graph, ω is the incident beam angle (angle between incident beam and the sample surface), and 2θ is the diffracted beam angle (angle between the incident beam and the diffracted beam). The angle ψ and φ represent the tilting

and rotating of the sample plate respectively. All the HRXRD experiments in this dissertation are carried out using a PANalytical X'Pert PRO Diffractometer, using Cu Kα1 radiation with a wavelength of 1.540598 Å.

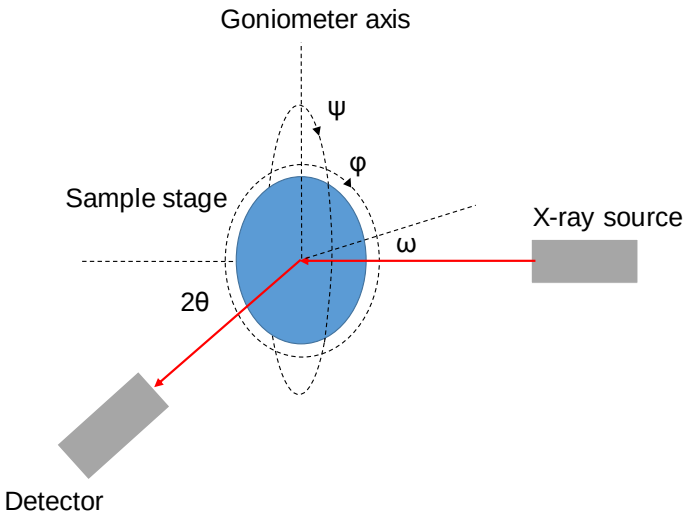

Fig. 2.7. Schematic Representation of High-Resolution X-ray Diffraction Measurements.

Bragg's Law is the basic of X-ray diffraction and can be expressed as follows:

$$2d \sin\theta = n\lambda \tag{2.1}$$

where d is the distance between diffraction planes, θ is the incident and diffracted beam angle, n is an integer representing the diffraction order, and λ is the wavelength of the X-ray beam. The geometry of Bragg diffraction in real space is shown in Fig. 2.8. The path difference of the two beams should be multiples of λ so that constructive interference is created, which is the physical meaning of Bragg's Law.

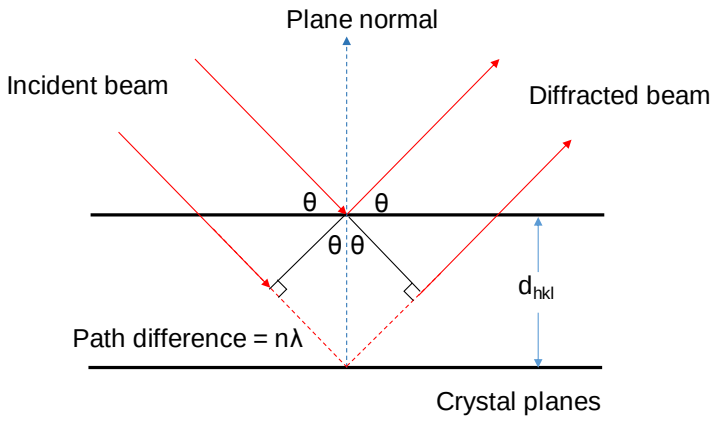

Fig. 2.8. Bragg Diffraction Geometry in Real Space.

Satisfying Bragg's Law is a necessary but not sufficient condition for constructive interference. That's because, the atomic arrangement on each lattice plane may be different resulting in a different phase shift of the incident beams, and the diffraction can be canceled even though the Bragg's Law condition is met. This phenomenon is called extinction. Structure factor *F*, which is the sum of atomic scattering amplitudes multiplied by the phase factors from each of the atoms in a unit cell, is used to calculate weather a diffraction plane will give constructive interference or not. The structure factor F_{hkl} is represented by the following equation:

$$F_{hkl} = \sum_j f_j e^{2\pi i(hx_j + ky_j + lz_j)}, \tag{2.2}$$

where f_j is the atomic scattering factor (proportional to the atomic number), *h*, *k*, *l* are the lattice plane indices, and x_j, y_j, z_j are the coordinates of atoms in a unit cell. For a binary alloy AB with zinc blende crystal structure (which are the materials used in our studies), the basis consists of A atoms located on an fcc lattice, and B atoms are displaced by 1/4 of a unit cell diagonal from the A atoms. Thus, for a zinc blende crystal, equation (2.2) is

equal to:

$$F_{hkl} = (f_A + f_B e^{\frac{\pi i}{2}(h+k+l)})(1 + e^{\pi i(h+k)} + e^{\pi i(h+l)} + e^{\pi i(k+l)}) \qquad (2.3)$$

Then we can determine *F* for all of the *hkl* indices:

$F = 0$ if *h*, *k*, and *l* are a mix of even and odd integers.

$F = 4(f_A \pm i f_B)$ if *h*, *k*, and *l* are all odd integers.

$F = 4(f_A - f_B)$ if *h*, *k*, and *l* are all even integers and $h+k+l=2N$, where *N* is odd.

$F = 4(f_A + f_B)$ if *h*, *k*, and *l* are all even integers and $h+k+l=2N$, where *N* is even.

When $F = 0$, the diffraction will be forbidden. It is therefore concluded that for AB binary Zinc Blende structure crystals, the allowable diffraction planes are those with all even or all odd plane index. A list of allowable diffraction planes (low *hkl* index) for an AB binary Zinc Blende structure is listed below.

Table 2.2. Allowable Diffraction Planes in AB Binary Zinc Blende Crystals.

Plane	111	002	022	113	222	004	133	024	224	115
F/4	$f_A - if_B$	$f_A - f_B$	$f_A + f_B$	$f_A + if_B$	$f_A - f_B$	$f_A + f_B$	$f_A - if_B$	$f_A - f_B$	$f_A + f_B$	$f_A - if_B$

The traditional X-ray diffraction measurement uses the ω-2θ scan, where the incident beam angle ω changes by $\Delta\theta$, accompanied by the diffracted beam angle 2θ changing by $2\Delta\theta$. When Bragg's Law condition is satisfied, a diffraction peak will appear during the ω-2θ scan for allowable diffraction planes. A more advanced understanding of X-ray diffraction should come from the reciprocal space point of view. Reciprocal space is the Fourier Transform of the real space, i.e. it represents the spatial periodicity in real space. As shown in Fig. 2.9, the reciprocal lattice constant $d^* = 1/d$, and a reciprocal lattice point represents a set of periodic planes in real space. The incident beam and diffracted beam are

represented by two reciprocal space vectors, K_o and K_H, whose amplitude are equal to $1/\lambda$. Vector Q is defined as the difference between K_o and K_H, and it represents the position where the reciprocal space is being probed. When vector Q lies between the origin and a reciprocal lattice point, a diffraction peak is observed. From the figure, it can be seen that in reciprocal space, the diffraction condition $d^* = |Q| = 2sin\theta|K_o|$ is consistent with the Bragg's Law condition in real space.

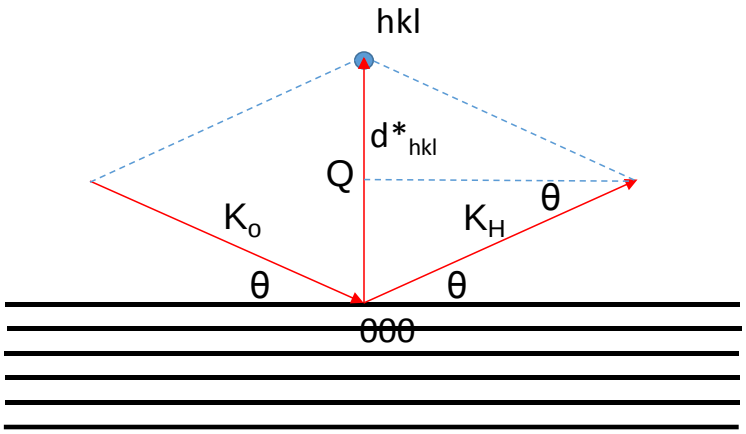

Fig. 2.9. Bragg Diffraction Geometry from Reciprocal Space Point of View.

When the ω-2θ scan is carried out, the tip of the Q vector in reciprocal space is moving forward along its direction. In Fig. 2.10, the upper two figures show the movement of Q, when the diffraction crystal plane is parallel to the sample surface, where $\omega = \theta$. The lower two figures show the movement of Q, when the diffraction crystal plane is not parallel to the sample surface, and thus $\omega \neq \theta$. In both cases, the tip of Q is moving away from the reciprocal space origin during ω-2θ scans. Another case is the Rocking-Curve scan or ω scan (not shown in the figure here), where only the sample is rotated, which is equivalent to that the sample is fixed while Q is rotating. In other words, in a Rocking-Curve scan, the

tip of vector Q will move in a direction perpendicular to that in a ω-2θ scan. Thus the FWHM of a diffraction peak in a ω-2θ scan and a Rocking-Curve scan is related to the broadening of the peak in different directions.

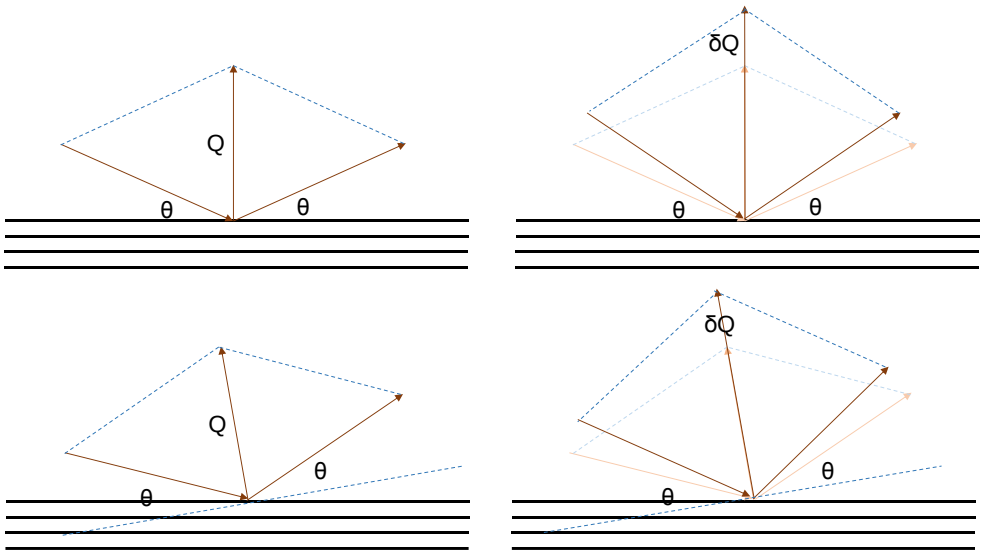

Fig. 2.10. ω-2θ Scan in Reciprocal Space.

The ω-2θ scans alone may not be able to determine the compositional or strain properties of an epilayer. For example, when a ternary alloy $A_xB_{1-x}C$ with a cubic crystal structure and unknown composition is measured, the lattice constants in both the x (in-plane) and the z direction have to be determined to calculate the free lattice constant (lattice constant when the epilayer is completely relaxed), and thus the composition and strain as shown by the following equations [24].

$$\varepsilon_z = -D\varepsilon_x \tag{2.4}$$

$$\varepsilon_x = \frac{a_x - a_{free}}{a_{free}},\ \varepsilon_z = \frac{a_z - a_{free}}{a_{free}} \tag{2.5}$$

$$D = \frac{2C_{12}}{C_{11}} \text{ (for cubic (001) direction)} \tag{2.6}$$

where ε_x and ε_z are strains in the x and z direction, and D is the deformation constant. In the case of a pseudomorphic epilayer, as shown in Fig. 2.11 left, its reciprocal lattice points are in vertical alignment with the substrate's, since their in-plane (xy direction) lattice constants are the same. Thus, only the ω-2θ scan along a (00h) diffraction is needed to calculate the z lattice constant and, therefore the compositional and strain properties. For a partially relaxed epilayer, however, the lattice constants in both the x and the z direction are unknown. Therefore both the ω-2θ scan along a (00h) diffraction, and reciprocal space mapping (RSM) near a (11k) diffraction have to be measured.

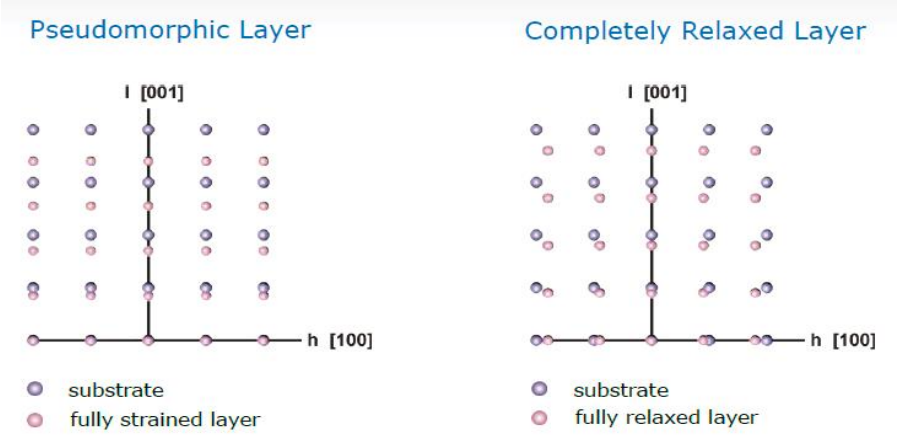

Fig. 2.11. Reciprocal Lattice of Pseudomorphic vs. Completely Relaxed Epilayers [25].

In an RSM scan, the tilting (if any) of the epilayers can be directly observed. In Fig. 2.12, the left shows that the epilayer's lattice is tilted relative to the substrate by a certain number of degrees, and the right shows that the reciprocal lattice of the epilayer is rotated by the same number of degrees. By measuring a (004) RSM, for example, the tilting can

be immediately seen and the tilting angle can be calculated.

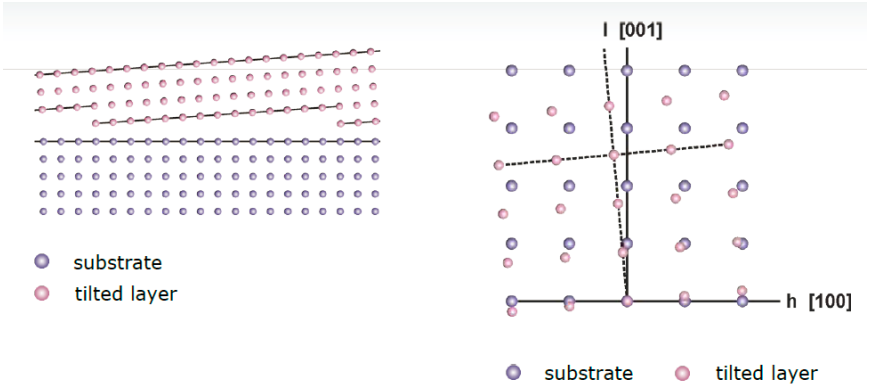

Fig. 2.12. Reciprocal Space Lattice of a Tilted Epilayer [25].

RSM can also show the broadening of a peak in all directions in reciprocal space. As discussed earlier, the ω-2θ scan and the Rocking-Curve scan can only show the FWHM of a peak in the Q direction and the direction perpendicular to the Q direction, respectively. Thus RSM could give more information on the material quality. The broadening of a diffraction peak can be due to multiple reasons: e.g. thin layer thickness; defects such as dislocations, precipitation and mosaic blocks. All broadening effects are essentially due to one reason: reduced periodicity in real space.

Both the ω-2θ and RSM scans are carried out to study the structural properties of CdTe/$Mg_xCd_{1-x}Te$ DHs. Shown in Fig. 2.13 is the ω-2θ scan along the 004 diffraction of a CdTe/$Mg_{0.24}Cd_{0.76}Te$ DH, which has a very narrow FWHM for the CdTe peak indicating high crystalline quality. The Pendellösung fringes from the CdTe layer and the thickness fringes from the $Mg_{0.24}Cd_{0.76}Te$ barrier layer are clearly seen, indicating high interface sharpness. The main $Mg_{0.24}Cd_{0.76}Te$ peak was used to simulate the Mg composition and

the thickness fringes are used to verify the $Mg_{0.24}Cd_{0.76}Te$ layer thickness. A software called Expert Epitaxy was used for the simulation.

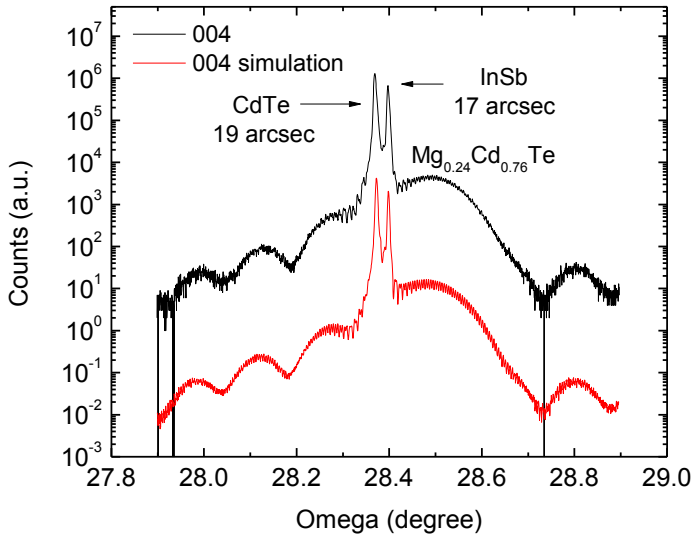

Fig. 2.13. ω-2θ Scan Around the (004) Peak of a CdTe/$Mg_{0.24}Cd_{0.76}Te$ Double Heterostructure.

Fig. 2.14 shows the RSM of the same DH around the (004) and (115) diffractions. From the (004) mapping, it is clearly seen that the epilayer's peaks are vertically aligned with the substrate peak, which means that the epilayers are not tilted. The (115) mapping also shows the epilayer's peaks are vertically aligned with the substrate peak, indicating that the epilayers are 100% constrained to the substrate (pseudomorphic). The small size of the reciprocal lattice spot for CdTe (comparable to the substrate), indicates the great crystalline quality.

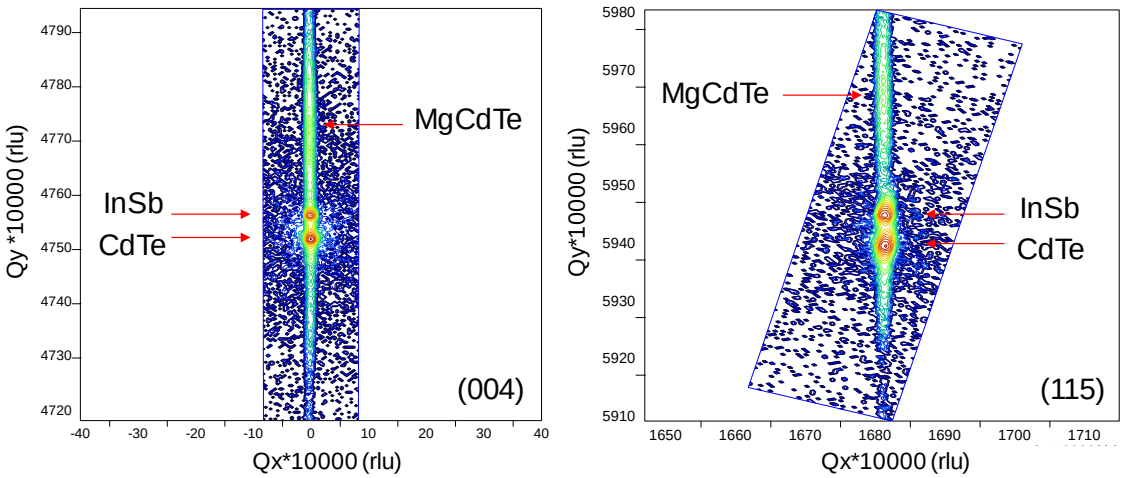

Fig. 2.14. Reciprocal Space Mapping of the (004) and (115) Peak of a $CdTe/Mg_{0.24}Cd_{0.76}Te$ Double Heterostructure.

2.3 Photoluminescence Spectroscopy

Photoluminescence (PL) spectroscopy measurements are very important to the analysis of direct bandgap optoelectronic materials such GaAs and CdTe, since they can give information about material quality, bandgap energy and defect states energy levels. The measurements in this dissertation are carried out based on a SPEX 1404 spectrometer system as shown below.

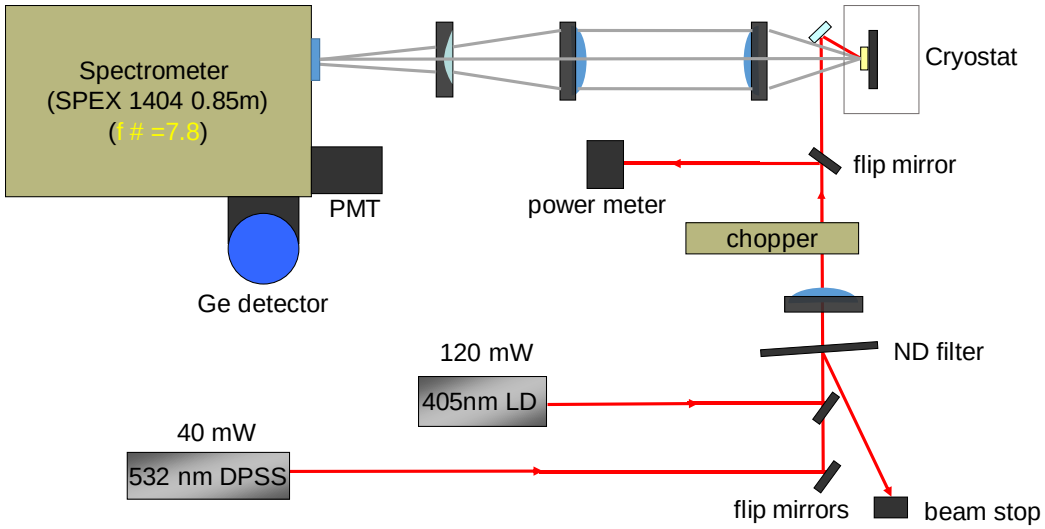

Fig. 2.15. Photoluminescence Spectroscopy System.

In this system, there are two lasers available with wavelengths at 532 nm and 405 nm respectively. For the study of CdTe/$Mg_xCd_{1-x}Te$ DHs the 532 nm laser is used. The laser beam is first focused and modulated by a chopper before it is incident on the samples. PL emitted from the sample surface is collected by several lenses and coupled into the SPEX 1404 spectrometer. The collecting optics has to be designed so that the PL light is focused on the entrance slit of the spectrometer and that the *f* number has to match that of the spectrometer (*f* = 7.8). The spectrometer has two gratings and a large focal length of 0.85 m, which can be used for high spectrum resolution measurements. The two detectors, a photomultiplier (PMT) and a Ge detector, are suitable for measurements in the visible and near IR regions, respectively. The output signal from the detector is connected to a lock-in amplifier, and at the same time the chopper sends a reference signal to the lock-in amplifier so that very weak signals can be extracted from the background. Low temperature measurement can be carried out using a closed-cycle He cooled cryostat down to 10 K.

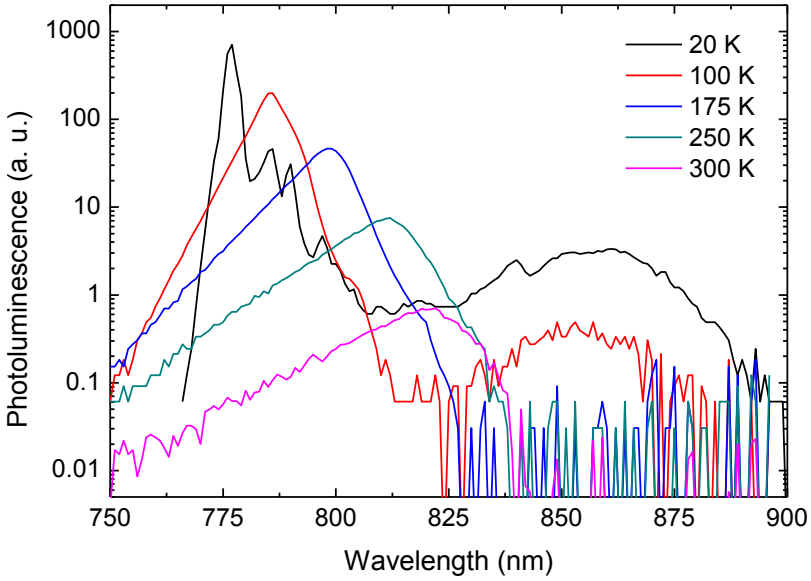

Fig. 2.16. Temperature Dependent Photoluminescence Spectra of a CdTe/$Mg_{0.24}Cd_{0.76}Te$ Double Heterostructure [26].

Fig. 2.16 shows an example of the temperature dependence of PL spectra for a CdTe/$Mg_{0.24}Cd_{0.76}Te$ DH [26]. At room temperature, the PL peak is at 820 nm which corresponds to a bandgap energy of 1.49 eV, considering that the PL peak is kT higher than the bandgap. As temperature decreases, the PL intensity increases due to reduced non-radiative recombination and increased radiative recombination (which will be discussed in the next chapter). The slope of the peak on the high energy side (Planck tail) becomes steeper as temperature decreases, due to the change of carrier distributions. The main peak blue shifts at lower temperatures. At 20 K, the sharp peak at 777 nm is believed to be a free exciton peak [27]. The nature of the weaker peaks near the 777 nm peak, which is not the focus of this work, may be attributed to excitons bound to defects or defect impurity

complexes. A broad peak, centered around 860 nm, appears when temperature is below 100 K, which is believed to be related to deep defect states. At higher temperatures, carriers are more likely to recombine non-radiatively through these defect states due to the interaction with phonons. Thus, this broad peak only shows up at very low temperatures. The intensity of the broad peak is more than two orders of magnitude weaker than that of the band edge emission, indicating low defect density in the CdTe layer and at the CdTe/$Mg_{0.24}Cd_{0.76}Te$ interfaces.

2.4 External Luminescence Quantum Efficiency Measurements

The PL spectra alone may not provide enough information about the quality of a material or a device structure, and absolute PL intensity is sometimes needed in order to predict device performances. The absolute PL intensity is directly proportional to the front surface external luminescence quantum efficiency ($\eta_{ext,f}$), which is defined as follows:

$$\eta_{ext,f} = \frac{\#\ photons\ emitted\ from\ the\ front\ surface\ into\ free\ space}{\#\ carriers\ generated\ in\ the\ active\ region}. \tag{2.7}$$

The $\eta_{ext,f}$ is a figure of merit for both solar cells and LEDs, and according to Ref. [28, 29], the implied open circuit voltage ($V_{i,OC}$) of a solar cell is directly related to $\eta_{ext,f}$ of the absorber layer:

$$V_{i,OC} = V_{DB} - \frac{kT}{q}\left|\ln(\eta_{ext,f})\right|, \tag{2.8}$$

where V_{DB} is the detailed-balance open circuit voltage, when $\eta_{ext,f}$ is 100%. Thus knowing the absolute PL intensity and $\eta_{ext,f}$ is helpful in predicting the open circuit voltage of a solar cell structure. To measure $\eta_{ext,f}$, the set up shown in Fig. 2.17 has been proposed [30].

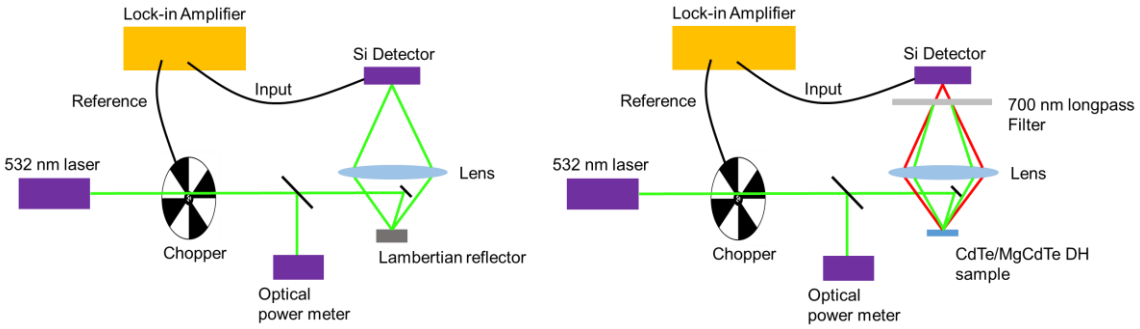

Fig. 2.17. External Luminescence Quantum Efficiency Measurement Setup. Left Shows the Measurement of a Lambertian Reflector with Calibrated Reflectance. Right Shows the Measurement of a CdTe/$Mg_xCd_{1-x}Te$ Double Heterostructure Sample [30, 31].

The left figure shows the measurement of a Lambertian reflector with calibrated reflectance. A 532 nm laser is sent through a chopper and incident onto the reflector. The reflector can scatter the laser light into a Lambertian distribution in space and the diffused light is then collected by a Si detector, the signal of which is amplified using a lock-in amplifier to improve signal-noise ratio. Using the same setup, CdTe/$Mg_xCd_{1-x}Te$ DHs are positioned at exactly the same position. The PL of the samples are collected by the Si detector and a 700 nm long-pass filter is used to block any light from the laser. Since the distribution of PL is the same as the Lambertian distribution, the signals from the Lambertian reflector and the sample can be compared. The front surface external luminescence quantum efficiency can then be calculated based on the comparison.

2.5 Time-Resolved Photoluminescence

Time-resolved photoluminescence (TRPL) is an important method to measure carrier lifetime, which is closely related to material qualities and determines device performances.

The experiments are carried out using a Time-Correlated Single-Photon-Counting (TCSPC) system as shown in the figure below.

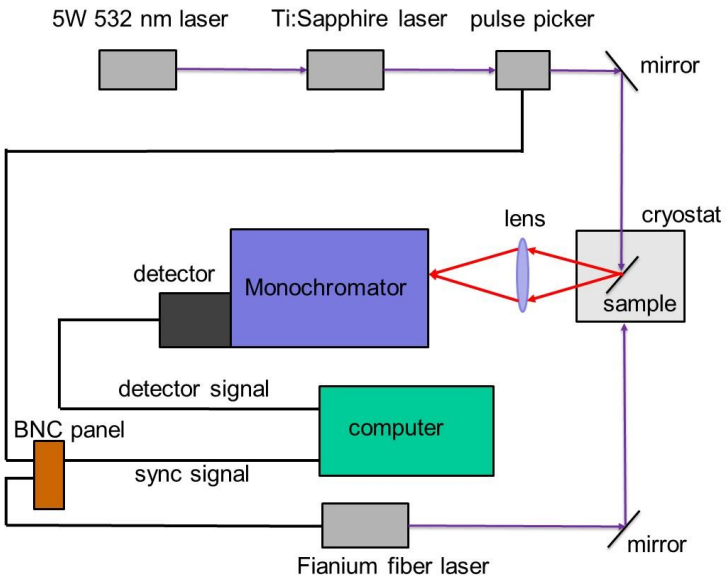

Fig. 2.18. Schematic Diagram of a Time-correlated Single-photon-counting System.

Two ultra-fast pulsed lasers are available as the excitation source: a Fianium fiber laser and a mode-locked Ti:Sapphire laser, which can emit laser light in the wavelength range of 450 nm - 750 nm and 700 nm - 950 nm respectively. The repetition rate of the Ti:Sapphire laser (0.4 MHz ~ 80 MHz) and the Fianium laser (0.1 MHz ~ 20 MHz) can be adjusted accordingly. A monochromator is used to collect the PL from the sample at a specific wavelength and a high speed PMT detector is used to detect the photons. The detector will then send the signal to a single-photon-counting card (Model SPC-830 [32]) installed on a computer. The SPC card also receives a reference signal from the excitation laser so that the arrival time of each single photon can be measured. Temperature-

dependent lifetime measurements can also be carried out down to 77 K by using a liquid nitrogen cooled cryostat.

2.6 Conclusions

The MBE growth and the material characterization techniques used in this study are summarized in this chapter. The successful growth of the high quality CdTe/$Mg_xCd_{1-x}Te$ double heterostructures are dependent upon careful preparation of the substrate, the growth temperature and the flux ratio optimization. High-Resolution X-Ray Diffraction can provide information about the material crystalline quality, composition, strain and thickness properties. The method of Reciprocal Space Mapping is reviewed and applied to our samples. Photoluminescence spectroscopy measurements can be used to evaluate the material quality, band gap energy and also the defect states at low temperatures. External luminescence quantum efficiency measurements are useful for the prediction of solar cell performance. Time-Resolved Photoluminescence measurement by Time-Correlated Single-Photon-Counting technique is reviewed and it is extremely important for the study of carrier lifetime and recombination properties of CdTe/$Mg_xCd_{1-x}Te$ double heterostructures as will be discussed in the following chapter.

Chapter 3

CARRIER LIFETIME ANALYSIS

3.1 Recombination Mechanisms in Semiconductors

There are three types of recombination mechanisms in a semiconductor: Shockley-Read-Hall, radiative, and Auger recombination, as shown in Fig. 3.1. The following paragraphs will give a short review of the characteristics of each recombination mechanism.

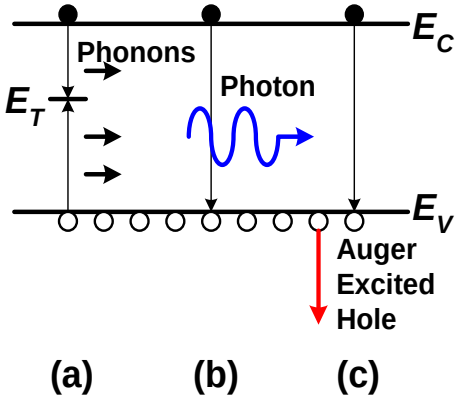

Fig. 3.1. (a) Shockley-Read-Hall Recombination. (b) Radiative Recombination. (c) Auger Recombination.

3.1.1 Shockley-Read-Hall Recombination

Shockley-Read-Hall (SRH) recombination is a process in which carriers recombine non-radiatively through trap states located within the bandgap, as shown in Fig. 3.1(a). The SRH recombination lifetime τ_{SRH} is derived as follows using rate equations [33][34]:

$$\tau_{SRH} = \frac{\tau_p(n_o+n_1+\Delta n)+\tau_n(p_o+p_1+\Delta p)}{p_o+n_o+\Delta n}, \tag{3.1}$$

$$n_1 = n_i e^{(E_T-E_i)/kT},\ p_1 = n_i e^{-(E_T-E_i)/kT}, \tag{3.2}$$

$$\tau_p = \frac{1}{\sigma_p v_{th,p} N_T},\ \tau_n = \frac{1}{\sigma_n v_{th,n} N_T}, \tag{3.3}$$

where τ_n and τ_p are SRH electron and hole minority carrier lifetimes, n_o and p_o are equilibrium electron and hole carrier concentrations, n_1 and p_1 are related to the defect state level E_T, σ_n *and* σ_p are electron and hole capture cross sections, $v_{th,n}$ and $v_{th,p}$ are the thermal velocity of electrons and holes, and N_T is the trap density.

SRH recombination is most effective when the trap energy level is close to the intrinsic Fermi level [35,36], which means that the corresponding n_1 and p_1 are much smaller than the majority carrier concentration. Now let's take CdTe as an example for the following discussions. Assuming CdTe is n-type doped, its intrinsic carrier concentration is on the order of 10^6 cm^{-3}, therefore $p_o << n_o$. Assuming the E_T level is close to the middle of the bandgap (n_1, $p_1 << n_o$), SRH lifetime is simplified to the following equation:

$$\tau_{SRH} = \frac{\tau_p(n_o+\Delta n)+\tau_n \Delta n}{n_o+\Delta n}. \tag{3.4}$$

At high injection levels, where $\Delta n >> n_o$

$$\tau_{SRH} \approx \tau_n + \tau_p \tag{3.5}$$

At low injection levels, where $\Delta n << n_o$

$$\tau_{SRH} \approx \tau_p \tag{3.6}$$

It is a little bit counter intuitive to understand that the high injection lifetime is even longer than the low injection lifetime. The physical meaning is that, at high injection levels, since the conduction band and valance band edge have high electron and hole concentrations, the middle gap states are filled with both electrons and holes and the recombination process depends on the capture of both electrons and holes. The lifetime therefore is $\tau_n+\tau_p$. At low injection levels, however, the middle gap states are filled mostly

with the majority carriers (electrons here), and thus the recombination process is determined by the capture of minority carriers (holes here) by the trap states and the lifetime is τ_p.

3.1.2 Radiative Recombination

Radiative recombination is the direct band to band recombination of electrons and holes near the band edges as shown in Fig. 3.1(b). Its rate equation is:

$$R = Bnp, \tag{3.7}$$

where B is the material radiative recombination coefficient. In a real semiconductor structure, however, the photon recycling effect can reduce the radiative recombination rate, by recycling photons before they are emitted into free space. The rate equation considering photon recycling factor γ_r is then as follows:

$$R = (1 - \gamma_r)Bnp, \tag{3.8}$$

where γ_r is the average probability of photons being recycled and it is calculated using the ray-tracing method depicted in Ref. [37]. For an n-type doped semiconductor such as CdTe and GaAs, the radiative recombination lifetime is expressed as follows:

$$\tau_{rad} = \frac{1}{(1-\gamma_r)B(n_o+\Delta n)} \tag{3.9}$$

$$\tau_{rad} \approx \frac{1}{(1-\gamma_r)B\Delta n} \quad \text{(high injection)} \tag{3.10}$$

$$\tau_{rad} \approx \frac{1}{(1-\gamma_r)Bn_o} \quad \text{(low injection)} \tag{3.11}$$

3.1.3 Auger Recombination

Auger recombination is another kind of non-radiative recombination with three particles involved in this process. They can be two electrons and one hole, or one electron and two holes as shown in Fig. 3.1(c). For the latter case, an electron recombines with one hole and the recombination energy is used to excite another hole to a higher energy level. Then the hole at the higher energy level will release its energy by thermal relaxation. The rate equations for Auger recombination are expressed as follows:

$$R_{eeh} = C_n n^2 p, \; R_{ehh} = C_p n p^2 \tag{3.12}$$

where C_n and C_p are Auger recombination coefficients.

3.2 ABC Model

This section will discuss the use of the ABC model to study different recombination mechanisms in several CdTe/$Mg_{0.24}Cd_{0.76}Te$ DHs [26], where *A*, *B*, and *C* are the SRH, radiative and Auger recombination coefficient respectively. A 532 nm laser is used for the excitation of the CdTe layer, and PL intensity is measured as a function of excitation power density. The samples measured have structure similar to that shown in Fig. 2.1, with 30 nm thick $Mg_{0.24}Cd_{0.76}Te$ barrier layers, a 1 μm thick CdTe middle layer and a 30 nm CdTe cap. During steady-state PL measurements, the generation rate (*G*) is equal to the recombination rate (*R*) inside the CdTe layer as described by [26]:

$$G = R = A\Delta n + (1 - \gamma_r)B\Delta n^2 + C\Delta n^3, \tag{3.13}$$

where $A\Delta n$, $(1\text{-}\gamma_r)B\Delta n^2$ and $C\Delta n^3$ are SRH, radiative, and Auger recombination rate, respectively. The relation in Eq. (3.13) is valid when photo-generated carrier density Δn is much larger than the equilibrium carrier density n_o. The samples studied here are undoped with a back ground carrier concentration on the order of 10^{14} cm^{-3}, and it is estimated that

Δn is much larger than n_o during the excitation dependent measurements. As discussed above, γ_r is the photon recycling factor and it is calculated to be 0.85 for the 1 μm thick CdTe middle layer in the DHs. The generation rate (G) is estimated based on the absorption of the pump laser beam in the 1 μm CdTe layers, taking into account the reflection loss and loss in the front cap and barrier layers. It is also assumed that carriers are distributed uniformly in the CdTe layer, due to the long diffusion length and confinement by $Mg_{0.24}Cd_{0.76}Te$ layers on both sides. The measured PL intensity (I) is proportional to the net radiative recombination rate and can be expressed as [26]

$$I = \eta(1-\gamma_r)B\Delta n^2, \tag{3.14}$$

where η is a proportionality factor, which is affected by the collection efficiency of the spontaneous emission from the sample surface by the PL system. From equation (3.13) and (3.14), the power law relation between the PL intensity (I) and generation rate (G) is given by [26]

$$G = A_0 I^{0.5} + B_0 I^1 + C_0 I^{1.5}, \tag{3.15}$$

where $A_0 = A/\sqrt{\eta(1-\gamma_r)B}$, $B_0 = 1/\eta$, and $C_0 = C/(\sqrt{\eta(1-\gamma_r)B})^3$. Excitation-dependent PL results of three samples are shown in Fig. 3.2 [26], where the generation rate (G) is plotted as a function of PL intensity (I) using a log–log scale. The samples are grown under different conditions and their lifetimes are different indicating different material qualities. The lifetimes are measured under low injection levels and were believed to be dominated by SRH recombination lifetime. However, later on it is found that the carrier lifetime of these set of samples are dominated by thermionic emission induced interface recombination (will be discussed in the next section). Nevertheless, both lifetimes can be assumed to be constant in this study and they will not affect the ABC

model. For easy discussion, the non-radiative lifetime, either contributed by SRH or thermionic emission induced interface recombination lifetime, is called SRH lifetime in this section.

As shown in the figure, the sample with the longer SRH lifetime has a stronger PL intensity and therefore, higher internal quantum efficiency compared to others at the same excitation density. For sample A1561, the slope of the curve is 0.52 in the low excitation range, which indicates that SRH recombination dominates at low injection according to the power law relation between *G* and *I*. As the generation rate becomes greater, the slope increases to 0.96, indicating that radiative recombination becomes dominant. No feature of Auger recombination was observed, which is expected since a relatively moderate PL pump power is used.

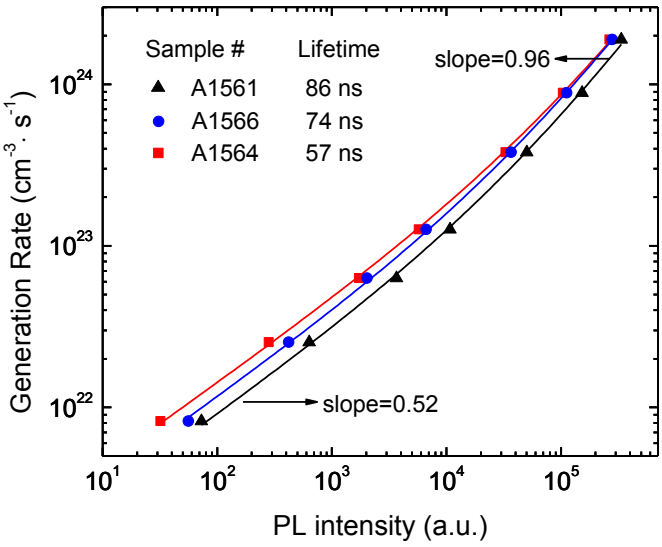

Fig. 3.2 Generation Rate vs. PL Intensity for Three CdTe/$Mg_{0.24}Cd_{0.76}Te$ Double Heterostructure Samples Grown under Different Conditions [26].

All other CdTe samples, grown under different conditions, demonstrated a similar behavior. Values of A_0 and B_0 are obtained by fitting the excitation-dependent PL curves with (3.15). The SRH recombination coefficient A is the inverse of the measured lifetime, i.e., $A = 1/\tau_{SRH}$. Therefore, the radiative recombination coefficient (B) can be calculated using the relationship

$$B = \frac{A^2 B_0}{A_0^2(1-\gamma_r)}. \tag{3.16}$$

The published experimental values of the radiative recombination coefficient (B) are scattered according to the literature. Two references reported the values of B (2×10^{-9} $cm^3 \cdot s^{-1}$ and 3×10^{-9} $cm^3 \cdot s^{-1}$) extracted from experimental results, without considering the photon recycling effect [38][39]. Thus, their reported B values are also related to the sample structure and may vary from sample to sample. In our work, the radiative recombination coefficient is defined as a material parameter, which is independent of sample geometry, since the geometry is accounted for by the photon recycling factor γ_r as defined above.

Table 3.1 summarizes the fitting results for six DH samples grown under different conditions. The optimal growth temperature and Cd/Te flux ratio are 265 ˚C and 1.5, respectively, as determined by TRPL. As expected, similar values for material radiative recombination coefficient B are obtained despite different material qualities (i.e., different SRH lifetimes). The average radiative recombination coefficient of all the studied samples is then determined to be $4.3\pm0.5\times10^{-9}$ $cm^3 \cdot s^{-1}$ for the MBE grown CdTe epilayers. It is worth mentioning that accurate determination of the radiative recombination coefficient, and the inclusion of the photon recycling effect are critically needed for the modeling of CdTe solar cells.

Table 3.1. Radiative Recombination Coefficient Study for CdTe/$Mg_{0.24}Cd_{0.76}Te$ Double Heterostructure Samples Grown under Different Conditions.

Sample #	Growth Temperature (°C)	Flux ratio (Cd/Te)	Lifetime (ns)	A_0 ($cm^{-3}\cdot s^{-1}$)	B_0 ($cm^{-3}\cdot s^{-1}$)	B ($cm^3\cdot s^{-1}$)
A1561	265	1.5	86	8.78×10^{20}	3.74×10^{18}	4.3×10^{-9}
A1571	280	1.5	83	8.69×10^{20}	3.99×10^{18}	5.1×10^{-9}
A1566	295	1.5	74	1.12×10^{21}	4.63×10^{18}	4.5×10^{-9}
A1567	265	1.2	64	1.32×10^{21}	4.12×10^{18}	3.8×10^{-9}
A1568	265	1.8	58	1.45×10^{21}	3.95×10^{18}	3.7×10^{-9}
A1564	250	1.5	57	1.39×10^{21}	4.24×10^{18}	4.5×10^{-9}

3.3 *B* from van Roosbroeck Model

The material radiative recombination coefficient *B* can also be calculated using the van Roosbroeck Model. The basic idea of this model is to use the detailed balance condition of photons: that is the absorption rate of photons must be equal to the radiative recombination rate at equilibrium [33]. Equation (3.17) represents the radiative recombination rate, where n_i is the intrinsic carrier density which is estimated to be 9×10^5 cm^{-3} from the effective mass and bandgap energy parameters of CdTe as listed in Table 3.2 [40]. Equation 3.18 represents the photon absorption rate, where $\bar{n}$ is the average refractive index near the band edge, *E* is the photon energy and α is the energy dependent absorption coefficient.

$$R = Bn_i^2 \tag{3.17}$$

$$A = \frac{8\pi\bar{n}^2}{h^3c^2}\int_0^\infty \frac{E^2}{\exp\left(\frac{E}{kT}\right)-1}\alpha(E)dE \tag{3.18}$$

The absorption coefficients and average refractive index are taken from Ref. [41]. The calculated radiative recombination coefficient *B* is 4.6×10^{-10} $cm^3\cdot s^{-1}$ based on the van Roosbroeck Model. This value is much smaller than the one extracted from the ABC model experiment. It is believed that the van Roosbroeck Model gives more reasonable results,

since it only uses a few simple material parameters, such as the absorption coefficient, bandgap energy etc., which are easy to measure. The ABC model methods are much more complicated, since they have many assumptions. For example, it assumes SRH lifetime is not dependent on the excess carrier density, which may not be true. As discussed above, the SRH lifetime under high injection level is longer than that under low injection level.

Table 3.2. The Bandgap Energy and Effective Mass Used for the Calculation of Intrinsic Carrier Concentration of CdTe.

E_g (eV)	m_e^* (m_0)	m_{hh}^* (m_0)	m_{lh}^* (m_0)	$m_h^* = (m_{hh}^{1.5} + m_{lh}^{1.5})^{2/3}$ (m_0)
1.5	0.09	0.76	0.144	0.80

3.4 Interface (Surface) Recombination Velocity

Reducing surface and interface recombination is very important for optoelectronic devices such as solar cells. GaAs and CdTe are two popular materials for high efficiency solar cells. It has been found that many materials, such as AlGaAs and GaInP [42-46], provide sufficient carrier confinement to GaAs with high interface qualities. The interface recombination velocity (IRV) of a high quality GaAs/$Al_{0.5}Ga_{0.5}As$ and GaAs/$Ga_{0.5}In_{0.5}P$ interface has been demonstrated to be as low as 18 cm/s and 1.5 cm/s respectively [43, 46], whereas the surface recombination velocity of a GaAs free surface is on the order of 10^7 cm/s [47]. Similarly, the surface recombination velocity of CdTe is found to be on the order of 10^5 cm/s [48]. Research efforts of reducing CdTe surface recombination include using chemical passivation which reduces the surface recombination velocity down to 200 cm/s [39] and using a CdS/CdTe heterojunction with an interface recombination velocity in the range of 10^3 cm/s ~ 10^6 cm/s [49, 50]. It has been reported that $Mg_xCd_{1-x}Te$ and CdTe form

a type-I band edge alignment [23], suggesting that $Mg_xCd_{1-x}Te$ is good for electron and hole confinement and has the potential to passivate the surface of CdTe.

The figure below shows the effectiveness of $Mg_xCd_{1-x}Te$ in confining carriers and improving PL intensity of CdTe. A 532 nm laser is used and its penetration depth in CdTe is 0.13 μm. All the samples have 30 nm thick $Mg_{0.24}Cd_{0.76}Te$ barrier and a 1 μm thick CdTe active layer. For the sample with only a bottom barrier, the PL intensity is the weakest even though the laser excitation density is 2.4 W/cm^2, which suggests strong non-radiative recombination at the CdTe surface. For the sample with only one top barrier, the PL intensity is stronger at only 0.1 W/cm^2 laser excitation, since the surface recombination is greatly reduced by $Mg_{0.24}Cd_{0.76}Te$ layer. However, carriers can still diffuse to the substrate and recombine there. The strongest PL intensity is achieved when the CdTe has barriers on both sides.

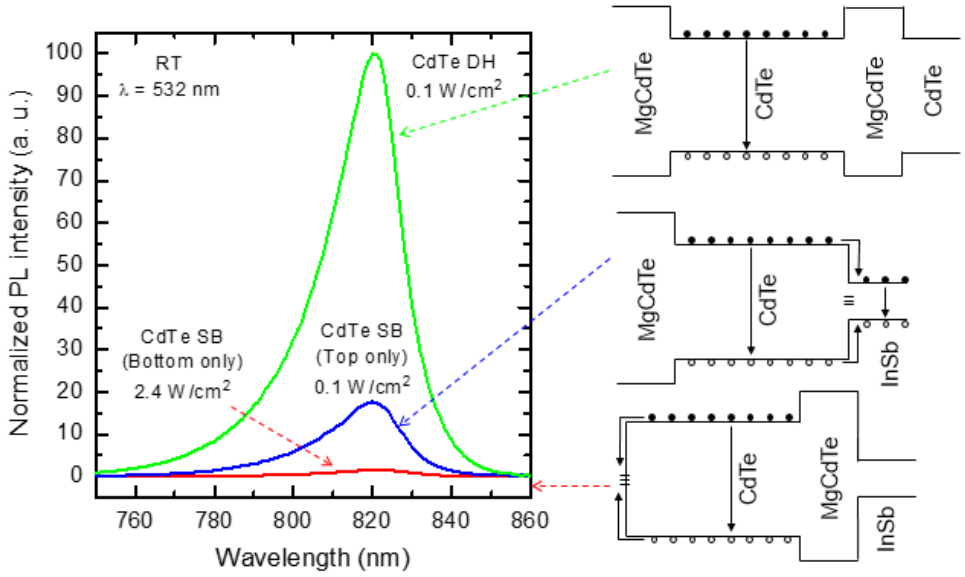

Fig. 3.3. Photoluminescence Spectra of CdTe/$Mg_{0.24}Cd_{0.76}Te$ Double Heterostructures.

The strong PL intensity observed in CdTe/$Mg_{0.24}Cd_{0.76}Te$ DHs suggests that: 1) $Mg_{0.24}Cd_{0.76}Te$ provides good carrier confinement; 2) The interface quality between CdTe and $Mg_{0.24}Cd_{0.76}Te$ is high. To determine the interface recombination velocity, a set of CdTe/$Mg_{0.24}Cd_{0.76}Te$ DHs are designed, all with 30 nm $Mg_{0.24}Cd_{0.76}Te$ barriers but with different thicknesses (0.3 μm, 0.5 μm, 1 μm, and 2 μm) for the middle CdTe layer.

Assuming that the excess carriers can distribute uniformly in CdTe due to the long diffusion length of minority carriers and the confinement by $Mg_{0.24}Cd_{0.76}Te$, the effective carrier lifetime (measured lifetime) τ_{eff} of a CdTe/$Mg_{0.24}Cd_{0.76}Te$ DH sample can be expressed using the following equation [51]:

$$\frac{1}{\tau_{eff}} = \frac{1}{\tau_{bulk}} + \frac{1}{\tau_{interface}} = \frac{1}{\tau_{bulk}} + \frac{2S}{d}, \tag{3.19}$$

where τ_{bulk} is the bulk carrier lifetime, $\tau_{interface}$ is the interface recombination lifetime, S is the interface recombination velocity, and d is the thickness of the sample. The above equation is valid when S is relatively small [51] and the diffusion length of minority carriers is much longer than the middle layer thickness.

Traditionally the bulk carrier lifetime is treated as thickness independent at low injection levels. However, it can vary with thickness of the sample, as it consists of both SRH ($\tau_{SRH,b}$) and radiative lifetime (τ_{rad}), and the latter is related to the photon recycling factor γ_r as shown below:

$$\frac{1}{\tau_{bulk}} = \frac{1}{\tau_{SRH,b}} + \frac{1}{\tau_{rad}} = \frac{1}{\tau_{SRH,b}} + (1-\gamma_r)Bn_o, \tag{3.20}$$

With a thicker CdTe layer in the middle, the photon recycling effect is stronger, and thus radiative lifetime is longer. In order to extract the interface recombination velocity S

more accurately, radiative lifetime has to be estimated and subtracted from the effective lifetime, shown in the following equation:

$$\frac{1}{\tau_{non}} = \frac{1}{\tau_{eff}} - \frac{1}{\tau_{rad}} = \frac{1}{\tau_{SRH,b}} + \frac{2S}{d}, \tag{3.21}$$

Fig. 3.4 shows the room temperature PL decays of the CdTe/$Mg_{0.24}Cd_{0.76}Te$ DHs with different CdTe middle layer thicknesses, where the initial PL intensity has been normalized. The carrier lifetime is determined by fitting near the tail of the decay curve. It is found that the thinner samples have shorter decay times, suggesting a non-zero recombination rate at the CdTe/$Mg_{0.24}Cd_{0.76}Te$ interface. The longest lifetime measured at room temperature is 179 ns for the sample with a 2 μm thick middle layer.

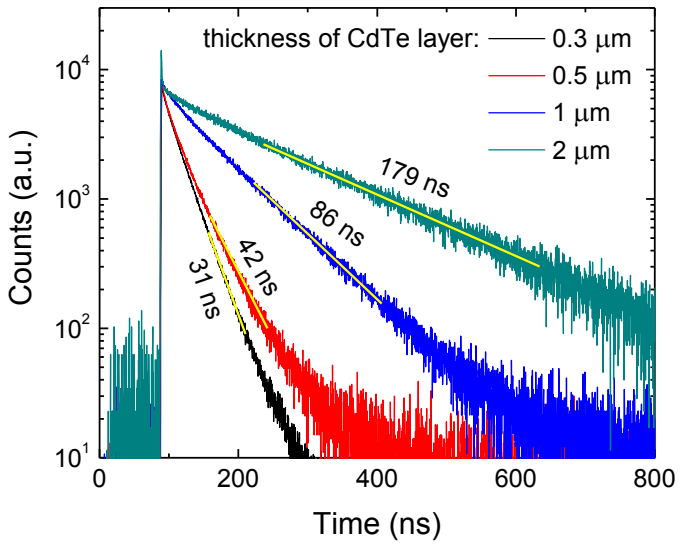

Fig. 3.4. Time-resolved Photoluminescence Decay of CdTe/$Mg_{0.24}Cd_{0.76}Te$ Double Heterostructures with Different Middle CdTe Layer Thicknesses [15].

High-resolution XRD measurements show that all the CdTe layers in the studied samples are coherently strained even when the thickness reaches 2 μm. Thus, it can be

assumed that the bulk SRH carrier lifetime is the same for samples with different CdTe layer thicknesses. Temperature-dependent and excitation-dependent PL measurements, show that non-radiative recombination dominates at room temperature and under low injection levels. Therefore, radiative lifetime has a negligible impact on the total lifetime and equation (3.19) can be used directly to extract interface recombination velocity.

As shown in Fig. 3.5, the interface recombination velocity at the CdTe/$Mg_{0.24}Cd_{0.76}Te$ interfaces and the bulk SRH lifetime of CdTe are extracted to be $(4.7\pm0.4)\times10^2$ cm/s and 0.5 μs, respectively. This interface recombination velocity is much smaller than that of a free CdTe surface and comparable to that of a typical GaAs/$Al_xGa_{1-x}As$ interface, suggesting that $Mg_xCd_{1-x}Te$ is an excellent barrier and surface passivation layer for CdTe based solar cells. The long bulk SRH carrier lifetime indicates that the CdTe epilayer grown on InSb substrates is of high quality, which is in agreement with the low defect densities of 10^4 cm^{-2} measured using confocal PL mapping [27]. It should be noted that the extracted bulk SRH lifetime is very sensitive to this fitting method and 0.5 μs is only a rough estimation.

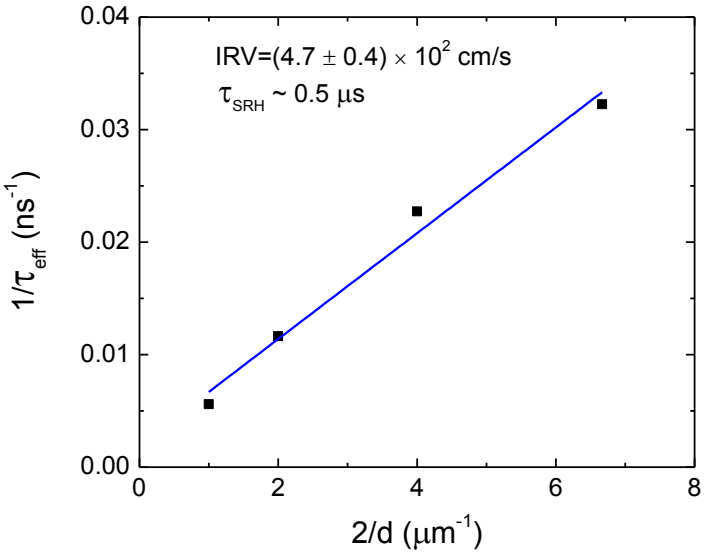

Fig. 3.5. The Inverse of Measured Lifetime vs. the Inverse of CdTe Layer Thickness for CdTe/$Mg_xCd_{1-x}Te$ Double Heterostructures [15].

3.5 Thermionic Emission & Tunneling

In this section, the term "effective interface recombination" will be used, since it is found that the measured interface recombination in a CdTe/$Mg_xCd_{1-x}Te$ DH can come from three different carrier loss mechanisms: 1) SRH recombination through trap states at the interface; 2) Thermionic emission of carriers over the barriers; 3) Tunneling of carriers through the barriers.

Table 3.3 shows the measured effective carrier lifetime (τ_{eff}) and extracted IRV (S_{eff}) for all different CdTe/$Mg_xCd_{1-x}Te$ DH samples grown and studied. For each set of samples (with the same $Mg_xCd_{1-x}Te$ barrier layers), the effective carrier lifetime increases as a function of the thickness of the middle CdTe layer, which implies a reduced equivalent interface recombination as the CdTe layer gets thicker. The IRV is fitted by using equation (3.21) [16,17].

Table 3.3. Measured Carrier Lifetime of CdTe/$Mg_xCd_{1-x}Te$ Double Heterostructures with Different Designs.

$Mg_xCd_{1-x}Te$ Barrier	Sample #	d (μm)	τ_{eff} (μs)	S_{eff} (cm/s)
t=30 nm 24% Mg	1	0.3	0.031	470±40
	2	0.5	0.042	
	3	1	0.086	
	4	2	0.18	
t=30 nm 36% Mg	5	0.2	0.24	54±32
	6	0.33	0.28	
	7	0.5	1.1	
t=30 nm 46% Mg	8	0.2	2.2	1.4±0.6
	9	0.25	2.2	
	10	0.33	2.8	
	11	0.5	3.6	
t=22 nm 46% Mg	12	0.2	2.0	1.2±0.7
	13	0.25	2.2	
	14	0.33	2.8	
	15	0.5	3.0	
t=15 nm 46% Mg	16	0.2	0.18	30±10
	17	0.25	0.31	
	18	0.33	0.47	
	19	0.5	0.83	
	20	1	0.75	
t=20 nm 36% Mg	21	0.25	0.15	61±14
	22	0.33	0.18	
	23	0.5	0.30	
	24	1	0.40	

Table 3.4 summarizes the effective IRV as a function of barrier layer thickness and Mg composition. It is found that for samples with 30 nm thick barriers, as the Mg composition increases from 24% to 46%, the effective IRV decreases dramatically from 470 cm/s to only 1.4 cm/s. For the same Mg (46%) composition, the IRV increases to 30 cm/s when the barrier thickness is reduced to 15 nm.

It is proposed that for samples with barriers with lower Mg compositions (24% and 36%), but still with sufficient thickness (20~30 nm), the effective IRV is mainly attributed

to the carrier loss due to thermionic emission of excess carriers over the barriers. For samples with thinner barriers (15 nm), but still with high Mg composition (46%), the effective IRV is mainly attributed to the excess carriers tunneling through the barrier layers. When both thermionic emission and tunneling effects are suppressed, the measured IRV (~1 cm/s) is purely due to recombination through interface trap states, i.e. SRH interface recombination. Such a low IRV indicates that the interface quality between CdTe and $Mg_xCd_{1-x}Te$ is close to perfection.

Table 3.4. CdTe/$Mg_xCd_{1-x}Te$ Effective Interface Recombination Velocity (S_{eff}) vs. the Barrier Thickness t and the Mg Composition in the Barrier [17].

S_{eff}(cm/s) Mg (%) / t (nm)	24	36	46
15	NA	NA	30
20~22	NA	61	1.2
30	470	54	1.4

Temperature dependent lifetime measurements are used to distinguish the different recombination mechanisms. As shown in (3.22), radiative lifetime is proportional to $T^{1.5}$ and it decreases with decreasing temperatures, since $B=B_{300K}(300K/T)^{1.5}$ has larger values at lower temperatures. Here N_D is assumed to be a constant, since the activation energy of the possible background dopants (indium) is only 14 meV [52]. The photon recycling factor is also assumed to be a constant, since the absorption coefficient near the band edge is insensitive to temperature changes [53]. The SRH recombination lifetime, both in the bulk $\tau_{SRH,b}$ and at the interfaces $\tau_{SRH,i}$, shown in (3.23) and (3.24), increases with decreasing

temperature, since the thermal velocity (v_{th}) of carriers is slower at lower temperatures and carriers are less likely to be captured by defects (with density of N_T or N_{iT} and capture cross section of σ_p or σ_{ps}). In (3.25), the thermionic emission induced interface recombination lifetime τ_{therm} is proportional to $T^{-0.5}$ and exp($\Delta E/kT$), where the ΔE term is related to the conduction and valance band offsets between CdTe and $Mg_xCd_{1-x}Te$ (Please see Appendix for detailed derivations). The thermionic emission induced interface recombination lifetime increases with decreasing temperatures, and it is very sensitive to temperature changes.

$$\tau_{rad} = \frac{1}{(1-\gamma_r)B_{300K}(\frac{300K}{T})^{1.5}N_D} \propto T^{1.5} \tag{3.22}$$

$$\tau_{SRH,b} = \frac{1}{\sigma_p v_{th} N_T} = \frac{1}{\sigma_p N_T}\sqrt{\frac{\pi m^*}{8kT}} \propto T^{-0.5} \tag{3.23}$$

$$\tau_{SRH,i} = \frac{d}{2S_{SRH}} = \frac{d}{2\sigma_{ps} v_{th} N_{iT}} \propto T^{-0.5} \tag{3.24}$$

$$\tau_{therm} = \frac{d}{2S_{therm}} = \frac{dexp(\frac{\Delta E}{kT})}{2(\frac{kT}{2\pi m^*})^{0.5}} \propto T^{-0.5}\exp(\frac{\Delta E}{kT}) \tag{3.25}$$

Temperature dependent TRPL measurements are carried out for samples # 2, 7 and 11, which have 30 nm thick barrier layers, but with different Mg composition (i.e. barrier potential), and a 500 nm thick CdTe middle layer. The tunneling induced interface recombination can be ignored in these samples due to the thick barrier layers. Fig. 3.6 shows the results for the 3 samples, and Fig. 3.7~3.9 show the carrier lifetime fitting using different recombination mechanisms.

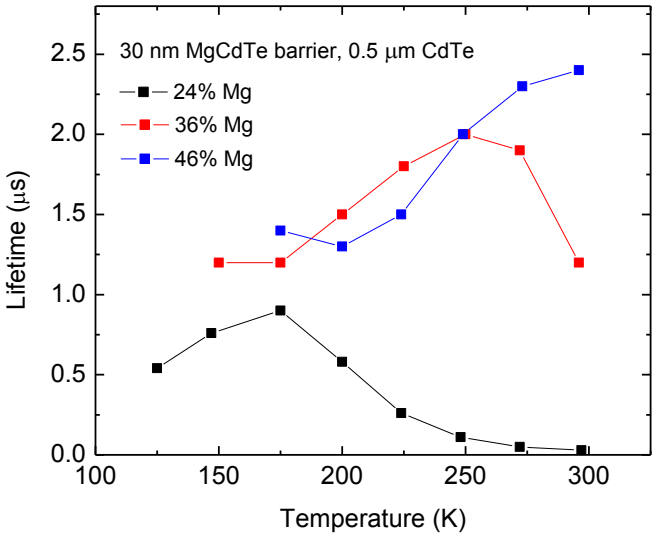

Fig. 3.6. Temperature Dependent Carrier Lifetime of CdTe/$Mg_xCd_{1-x}Te$ DHs with 30 nm Barriers and 0.5 μm CdTe Middle Layer [17].

The sample in Fig. 3.7 has the lowest Mg composition (24%) and thus the lowest barrier potential. At higher temperatures, the carrier lifetime can be fitted very well by the thermionic emission induced interface recombination lifetime. An activation energy of 170 meV is achieved for the thermionic emission process, which is between the value of conduction band offset, 252 meV, and valance band offset, 108 meV, at the CdTe/$Mg_{0.24}Cd_{0.76}Te$ interface. It indicates that the theriomic emission induced recombination process is dependent on the emission of both electrons and holes. Once the temperature is reduced below 150 K, radiative recombination starts to dominate. The fitted room temperature radiative lifetime is 2.4 μs.

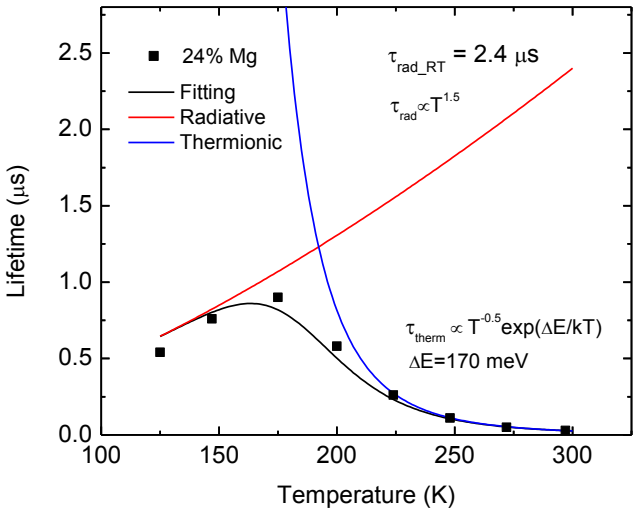

Fig. 3.7. Fitting of Temperature Dependent Carrier Lifetime of CdTe/$Mg_{0.24}Cd_{0.76}Te$ DH with 30 nm Barriers [17].

Fig. 3.8 shows the carrier lifetime of the sample with higher Mg composition (36%). A higher activation energy (280 meV) is fitted for the thermionic emission process, which is also between the conduction band (378 meV) and valance band offset (162 meV) values. Since the barrier height is higher than the sample in Fig. 3.7, the room temperature carrier lifetime is greatly enhanced. Radiative lifetime starts to dominate at temperatures below 220 K, which is also higher than the previous sample. A similar room temperature radiative lifetime is fitted.

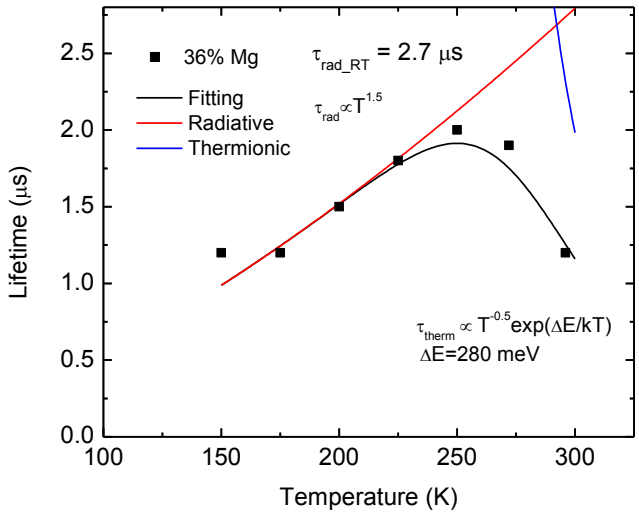

Fig. 3.8. Fitting of Temperature Dependent Carrier Lifetime of CdTe/$Mg_{0.36}Cd_{0.64}Te$ DH with 30 nm Barriers [17].

The sample in Fig. 3.9 has the highest Mg composition (46%) in the barrier, and thus starting from room temperature, radiative recombination dominates. The lifetime decreases with decreasing temperature just as the radiative lifetime model predicts. A similar room temperature radiative lifetime is fitted, indicating the consistency of this method. Excitation dependent PL measurements also show that the sample is dominated by radiative recombination at room temperature.

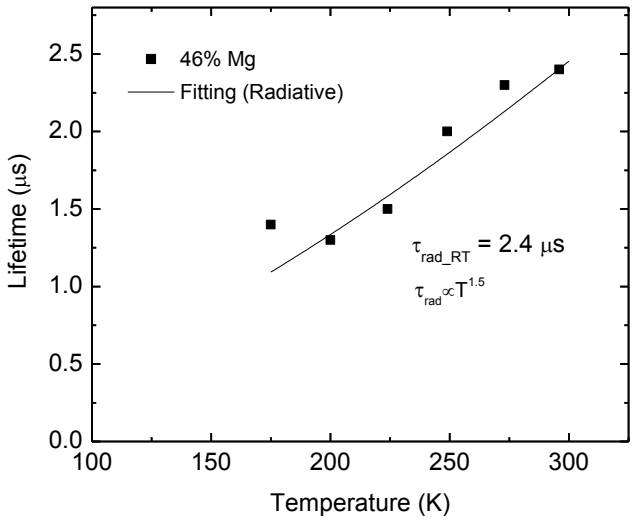

Fig. 3.9. Fitting of Temperature Dependent Carrier Lifetime of CdTe/$Mg_{0.46}Cd_{0.54}Te$ DH with 30 nm Barriers [17].

In Fig. 3.7~3.9, SRH lifetimes were not used in the fitting, since the feature of it is not obvious. It indicates that the SRH lifetime for the above samples (both at the CdTe bulk layer and CdTe/$Mg_xCd_{1-x}Te$ interfaces) must be much longer than the measured effective lifetime. It again proves that the material quality of CdTe/$Mg_xCd_{1-x}Te$ DHs is very high.

3.6 Conclusions

Carrier lifetimes in CdTe/$Mg_xCd_{1-x}Te$ double heterostructures (DHs) have been extensively studied by time-resolved photoluminescence measurements (TRPL). The DHs are designed with different $Mg_xCd_{1-x}Te$ barriers and with different thickneses in the middle CdTe layers. Effective interface recombination velocity between CdTe and $Mg_xCd_{1-x}Te$ can be fitted with thickness dependent carrier lifetime. It is found that when the barriers are low or thin, the thermionic emission and tunneling induced interface recombination

velocity will contribute to the effective interface recombination velocity. The actually interface recombination veclocity, which is purely due to interface recombination through trap states, is only ~ 1 cm/s, when the thermionic emission and the tunneling effect are greatly suppressed. The low interface recombination velocity and long carrier lifetime (~3.6 μs) indicate that CdTe/$Mg_xCd_{1-x}Te$ DHs have very high material quality, both at the interface and in the bulk region, which can enable its successful application in CdTe based solar cells.

Chapter 4

DOPING IN CDTE AND ITS APPLCIATION IN SOLAR CELLS

Although it has been found that p-type doping is hard to achieve in CdTe, various studies have shown the possibility of efficient n-type doping in CdTe by using In, grown by Molecular Beam Epitaxy (MBE) [52, 54-57]. In this chapter, CdTe/$Mg_{0.46}Cd_{0.54}Te$ double heterostructures (DHs) are doped with In and the doping vs. carrier concentrations are studied. The carrier lifetime and external photoluminescence quantum efficiency are measured and their impact on device efficiency is discussed. Finally, the DHs are successfully used in solar cells, which enabled a record high 17.0% efficiency and V_{oc}=1.096 V [19]. By the time of writing this dissertation, the record cell efficiency has reached 18.5%.

4.1 Indium Doped CdTe/$Mg_xCd_{1-x}Te$ Double Heterostructures

The designed layer structure of an In-doped CdTe/$Mg_{0.46}Cd_{0.54}Te$ DH is shown in Fig. 4.1. The CdTe/$Mg_{0.46}Cd_{0.54}Te$ DH region is doped at concentrations from 1×10^{16} cm^{-3} to 7×10^{18} cm^{-3}. It has been discussed in the above chapters that the $Mg_{0.46}Cd_{0.54}Te$ layer can provide sufficient carrier confinement, and also passivate the surface of CdTe. The Mg composition of 46±1% is determined by High-Resolution X-ray Diffraction (HRXRD) measurements. The 30 nm thick CdTe cap layer is used to prevent the top $Mg_{0.46}Cd_{0.54}Te$ layer from oxidizing in the air.

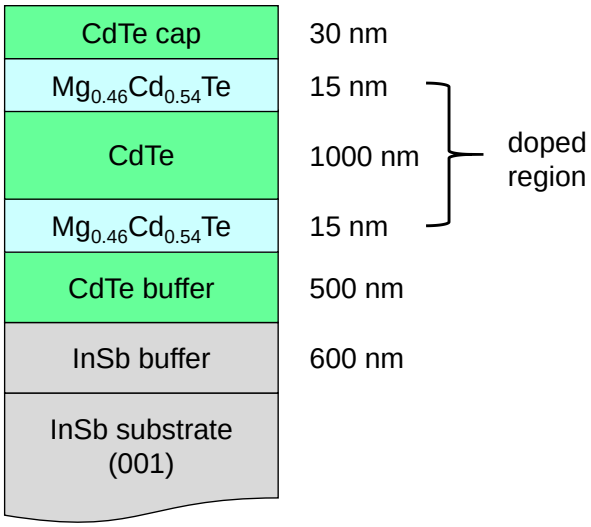

Fig. 4.1. Designed Layer Structure of In-Doped CdTe/$Mg_{0.46}Cd_{0.54}Te$ Double Heterostructures.

The desired In cell temperature for each doping level is determined by the In doping calibration curve as shown in Fig. 4.2. The data points in the figure are from a standard sample quantified by Secondary Ion Mass Spectroscopy (SIMS) measurements, with various doping concentrations at different depths, and the straight line is fitted from the data points. The flux ratio of Cd/Te is 1.5 during the CdTe layer growth, which is believed to be favorable for the effective activation of In dopants [52,56].

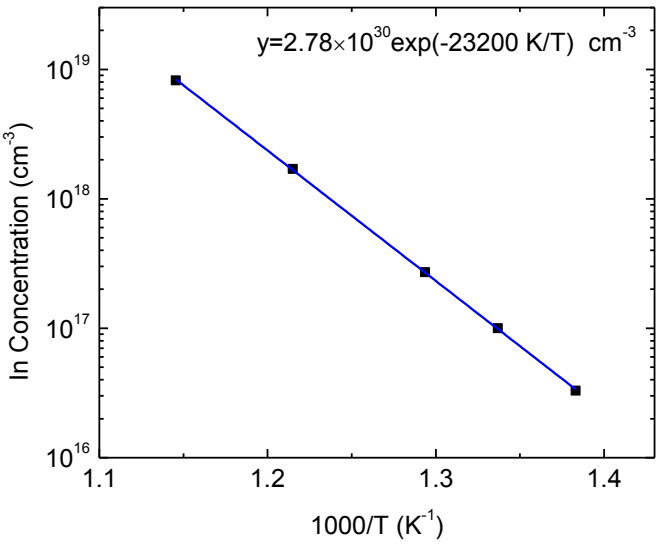

Fig. 4.2. In Concentration in CdTe vs. In Cell Temperature [18].

4.2 Carrier Concentration vs. Doping Concentration

In a semiconductor the carrier concentration may not necessarily be equal to the doping concentration, as the dopants can be compensated by other types of dopants or defects. In this study, SIMS and Capacitance-Voltage (CV) measurements are used to determine the doping and carrier concentrations, respectively.

A Cameca IMS 6f spectrometer is used for SIMS measurement. The primary ion beam is O_2+ and the vacuum level is kept at 2×10^{-9} Torr in the chamber. The quantification of In concentration is realized by using a standard sample previously measured at Evans Analytical Group (EAG). Since ^{115}CdH and ^{115}In have the same mass, an undoped CdTe/$Mg_{0.46}Cd_{0.54}$Te DH reference sample is measured in order to know the ^{115}CdH background level and to eliminate the mass interference. For each sample, the In and Te counts are measured and the In/Te ratio is calculated. The In/Te background due to the ^{115}CdH mass interference is subtracted. Thus with the absolute In/Te ratio, and a standard

sample, the In doping concentration in each sample can be calibrated. For all the samples, the In doping concentrations are very close to the designed values, indicating the effective guidance of the calibration curve in Fig. 4.2.

Fig. 4.3 shows a typical SIMS profile, measured for a sample doped with 1×10^{18} cm^{-3} In. The Mg and Te are plotted as marker species and their curves correspond to the secondary ion intensity on the right axis. The In curve corresponds to the doping concentration on the left axis. It is found that the In concentration is constant within the DH, indicating a uniform doping profile, and that In can also diffuse from the substrate into the CdTe buffer layer. The magenta line from 1.20 μm to 1.44 μm represents the fitted In concentration, assuming a one dimensional diffusion model with a constant source at one end of an infinite long specimen. The analytical equation for this model is shown in equation (4.1) [58]. The diffusion length $\sqrt{Dt}$ is fitted to be 0.1 μm and the corresponding diffusion coefficient D is extracted to be 1×10^{-14} cm^2/s, by assuming 2 hours of diffusion at the growth temperature of 265 ˚C. All the samples have a similar In profile, except for the 4×10^{18} cm^{-3} and 7×10^{18} cm^{-3} doped samples, in which In also tends to diffuse strongly from the doped CdTe layer to the bottom CdTe buffer.

$$C(x,t) = C_O\left(1 - \mathrm{erf}\left(\frac{x}{2\sqrt{Dt}}\right)\right) \tag{4.1}$$

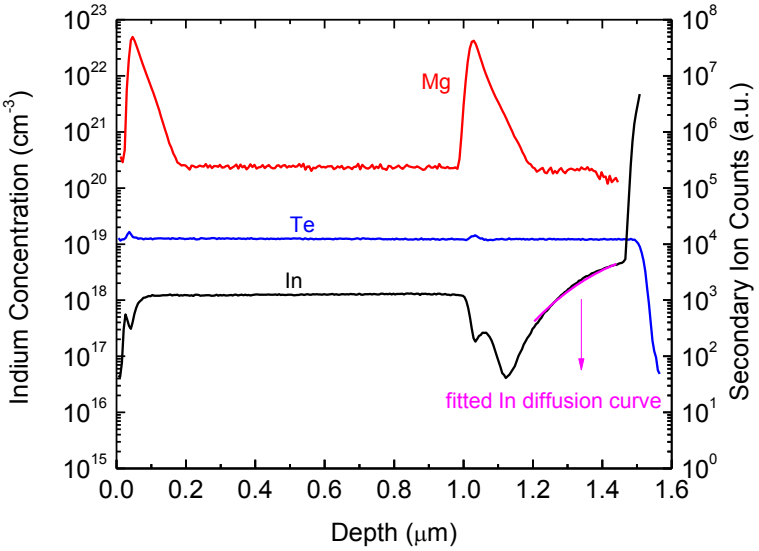

Fig. 4.3. SIMS Profile of a CdTe/$Mg_{0.46}Cd_{0.54}Te$ Double Heterostructure Sample Doped with 1×10^{18} cm^{-3} In. [18]

C-V measurements are carried out using a mercury probe station with a precision LCR meter. The ac frequency of the bias is 100 kHz and the amplitude is 25 mV. Both the mercury probes are in contact with the top surface of the sample as shown in Fig. 4.4 (a). The smaller contact has an area of 4.56×10^{5} μm^2 and the area ratio between the two contacts is 48.6:1. With a reverse bias applied to the smaller contact and a forward bias applied to the bigger contact, the measured capacitance across the sample is determined by the smaller contact as shown in Fig. 4.4 (b). Thus the carrier concentrations near the smaller contact can be probed.

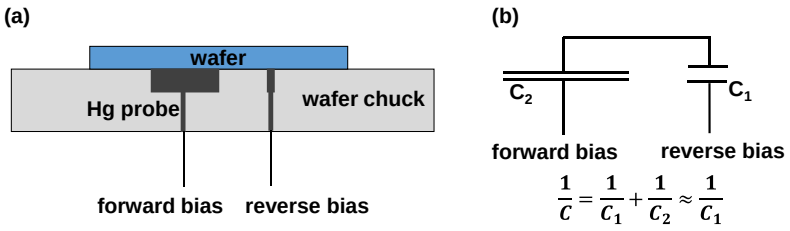

Fig. 4.4. (a) Schematic Diagram of Capacitance-voltage Measurement Using the Mercury Probe Method. (b) The Equivalent Circuit. [18]

C-V measurements show that the carrier concentration of the undoped DH is about 5×10^{14} cm^{-3}. For the In-doped samples, with doping concentrations from 1×10^{16} cm^{-3} to 1×10^{18} cm^{-3}, the carrier concentration is almost the same as the atomic doping concentration, indicating 100% ionization as shown in Fig. 4.5. The slight difference between the data points and the dashed 100% ionization line is probably due to the errors in both SIMS and C-V measurements. The standard sample measured by EAG has ± 10% error bars for the doping concentrations, thus it is reasonable to assume that the error bar is ± 10% for the quantification of the rest of the samples. The mercury probe station was calibrated using n-type silicon wafers with known carrier concentrations, however the actual size of the mercury contact is dependent upon the surface tension between CdTe and mercury and the applied vacuum level, which can introduce error bars to the calculated carrier concentrations as shown in (4.2). The carrier concentration error bar shown in Fig. 4.5, is calculated assuming ±12.5% error bars for the mercury probe contact area.

$$N_D(W) = \frac{C^3}{qK_s\varepsilon_0 A^2 dC/dV} \tag{4.2}$$

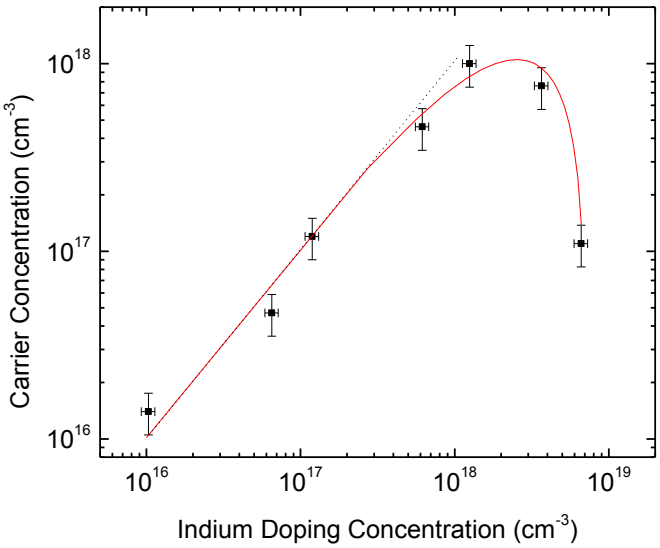

Fig. 4.5. Carrier Concentration vs. In Doping Concentration in the CdTe Layer. [18]

When the doping concentration increases to 4×10^{18} cm^{-3} and 7×10^{18} cm^{-3}, the carrier concentration reduces to only 8×10^{17} cm^{-3} and 1×10^{17} cm^{-3}, respectively, which indicates strong compensation at higher doping levels. It was mentioned that Cd over pressure during the CdTe layer growth is favorable for the activation of In dopants, since it prevents the formation of Cd vacancies (p-type) when In is present [52]. Based on our observation, it is possible that below 1×10^{18} cm^{-3} doping level, Cd/Te flux ratio of 1.5 is enough for the effective activation of In, however beyond that doping level, higher Cd/Te flux ratio may be needed.

4.3 Photoluminescence Intensity and Carrier Lifetime

Fig. 4.6 shows the room temperature PL spectra of the above CdTe/$Mg_{0.46}Cd_{0.54}Te$ DHs measured under the same conditions. CdTe shows a PL peak position at 820 nm at room temperature, which corresponds to a bandgap of 1.49 eV, considering the *kT* difference

between the PL peak and the band gap energy. It is expected that with higher doping concentrations the radiative recombination rate is faster and thus the PL intensity is stronger. However, this is not the case when the doping concentration is higher than 1×10^{17} cm^{-3}, which suggests that non-radiative recombination also becomes much stronger when the doping concentration is above this level. Non-radiative recombination is closely related to the defect states located within the bandgap. As can be seen in the PL spectra, when the doping concentration reaches 6×10^{17} cm^{-3}, not only does the PL intensity become weaker but also the spectrum becomes broader, indicating increased defect states within the bandgap and degraded crystalline quality. When the doping concentration is even higher, a shoulder peak appears next to the CdTe peak, indicating an impurity band within the bandgap.

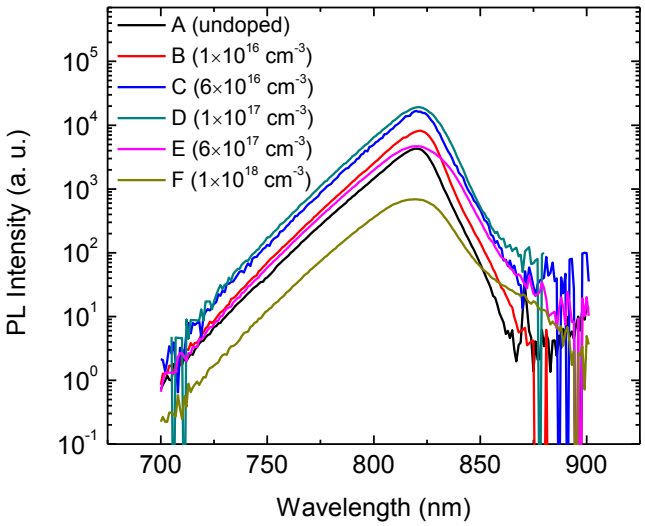

Fig. 4.6. Photoluminescence Spectra of CdTe/$Mg_{0.46}Cd_{0.54}Te$ Double Heterostructures with Different Doping Concentrations [18].

Fig. 4.7 shows the PL decay of the DHs with different doping concentrations. For some of the curves, the decay process is non-single-exponential, and becomes very slow at the tail of the decay, the reason for which is not very clear at this moment. For comparison the carrier lifetimes are fitted using the initial decay part of each curve, where the excess carrier density is about 1×10^{15} cm^{-3}. It is noted that the carrier lifetime decreases with increasing doping concentration, which is due to the decrease of both radiative and non-radiative lifetimes.

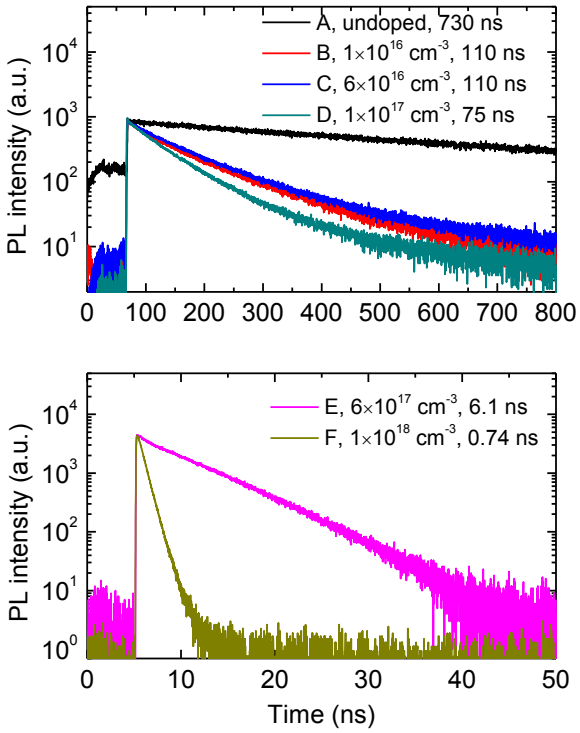

Fig. 4.7. Photoluminescence Decay of CdTe/$Mg_{0.46}Cd_{0.54}Te$ Double Heterostructures with Different Doping Concentrations [18].

The carrier lifetime and PL peak intensity together as a function of carrier concentration are plotted in Fig. 4.8, and their behavior can be explained as follows. The PL intensity is proportional to the front surface external PL quantum efficiency ($\eta_{ext,f}$), which is defined as shown in (4.3). It is related to spontaneous emission efficiency (η_{sp}) which is defined as the ratio of radiative recombination events to the total recombination events, as shown in (4.4). The total recombination consists of both radiative and non-radiative recombination which includes Shockley-Read-Hall (SRH) recombination in the CdTe bulk region, and an effective interface recombination at the CdTe/$Mg_{0.46}Cd_{0.54}Te$ interfaces. The radiative recombination rate is related to the doping concentration at low injection levels and is stronger with higher effective doping. The bulk SRH recombination is related to the quality of CdTe and with higher doping the quality of the sample may become worse and thus bulk SHR lifetime may decrease. The interface recombination lifetime is not only related to the interface quality, but also to the band bending at the CdTe/$Mg_{0.46}Cd_{0.54}Te$ interface region. With higher n-type doping concentrations, the band bending is stronger at the interface, and it is possible that the minority carrier (hole) is driven away from the interface resulting longer effective interface recombination lifetime.

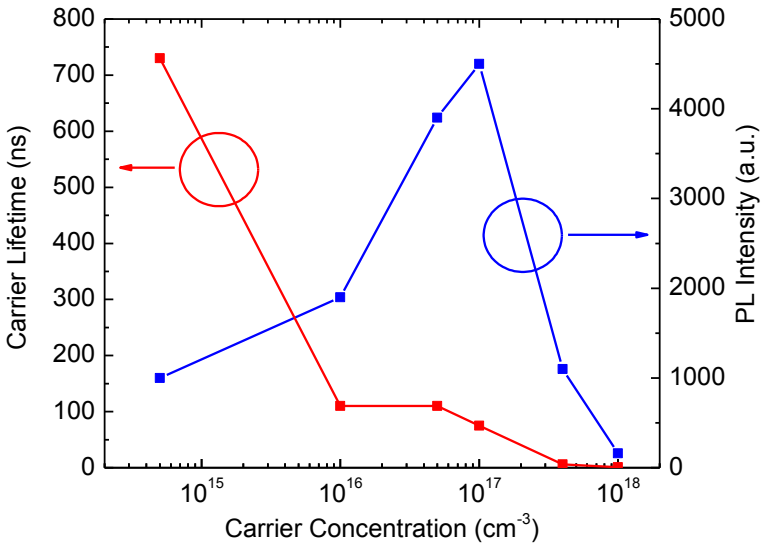

Fig. 4.8. Carrier Lifetime & Photoluminescence Peak Intensity of CdTe/$Mg_{0.46}Cd_{0.54}Te$ Double Heterostructures with Different Carrier Concentrations [18].

$$\eta_{ext,f} = \frac{\#\ photons\ emitted\ from\ the\ front\ surface\ into\ free\ space}{\#\ carriers\ generated\ in\ the\ active\ region} \tag{4.3}$$

$$\eta_{sp} = \frac{R_{Rad}}{R_{total}} = \frac{R_{Rad}}{R_{Rad}+R_{non}} = \frac{R_{Rad}}{R_{Rad}+R_{SRH,b}+R_{interface}} \tag{4.4}$$

$$\eta_{ext,f} = \frac{\gamma_{e,f}\eta_{sp}}{1-\gamma_r\eta_{sp}} \tag{4.5}$$

The $\eta_{ext,f}$ and η_{sp} can be related to each other by using (4.5), where γ_r is the photon recycling factor and $\gamma_{e,f}$ is the photon extraction factor at the front surface. Those two factors represent the average probability that a luminescence photon can be reabsorbed or escape the sample. Since all samples compared here have similar structures, the photon recycling and extraction factors are similar and thus higher $\eta_{ext,f}$ or stronger PL corresponds to higher η_{sp}.

When the doping concentration is below 1×10^{17} cm^{-3}, non-radiative lifetime may only decrease slightly while radiative lifetime decreases inversely with higher doping

concentration, resulting in an increased spontaneous emission efficiency and thus a stronger PL intensity. However, when the doping concentration is above the level of 1×10^{17} cm^{-3}, non-radiative lifetime starts to decrease dramatically, while radiative lifetime still decreases at the same rate. Thus, a weaker PL intensity is observed at higher doping concentrations. The dramatic decrease in non-radiative lifetime may be due to the formation of In-related defect states located within the bandgap. Further investigations are needed to confirm this. The relative constant carrier lifetime in the doping range of 1×10^{16} cm^{-3} ~ 1×10^{17} cm^{-3}, is probably due to the reason that interface recombination lifetime may have increased with stronger band bending, which offsets the effect of decreasing bulk SRH and radiative lifetime.

4.4 External Luminescence Quantum Efficiency and Implied V_{oc}

Thermodynamic theory can correlate the front surface External Luminescence Quantum Efficiency ($\eta_{ext,f}$) with the implied V_{oc}. Assuming that a piece of semiconductor material is placed in the dark environment, as shown in the top of Fig. 4.9, the sample absorbs blackbody radiations from the surroundings (J_o) and at the same time emits the same amount of light back into the environment. Thus the sample is at equilibrium state. As shown in (4.6), J_o is related to the angle averaged absorptance $A_2(E)$ for blackbody radiation $b(E)$ (#/(cm^2·s·eV)). While in the bottom of the figure, the same material is illuminated under direct sun light. The absorption is represented by J_{sc} and the emission is represented by $J_{emitted}$. J_{sc} can be calculated as shown in (4.7), where $A_1(E)$ is the absorptance of the active layer for direct sunlight and $S(E)$ is the solar photon flux density.

$$J_0 = \int A_2(E)b(E)dE \tag{4.6}$$

$$J_{sc} = \int A_1(E)S(E)dE \tag{4.7}$$

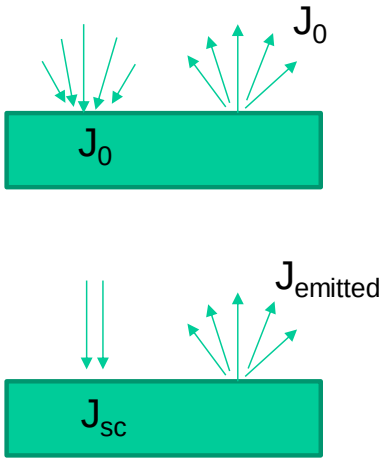

Fig. 4.9. (Top) a Semiconductor Material in Dark Environment, and (Bottom) under One Sun Illumination.

Under Boltzmann statistics, the emitted light ($J_{emitted}$) under illumination is related to J_o by a chemical potential μ (which is the quasi-Fermi level separation) as shown in (4.8) [59]. It means that the stronger the emission, the larger the quasi-Fermi level separation is in the sample.

$$J_{emitted} = J_0 \exp(\frac{q\mu}{kT}) \tag{4.8}$$

When the sample could emit the same number of photons back to the environment as it absorbs ($J_{emitted} = J_{sc}$), the chemical potential is the Detailed-Balance voltage (V_{DB}) (4.9). The material has to be 100% dominated by radiative recombination, and a perfect back mirror has to be presented to reach Detailed-Balance condition.

$$\mu = \frac{kT}{q} \ln\left(\frac{J_{sc}}{J_0}\right) = V_{DB} \tag{4.9}$$

However, in most cases, the emitted photon number is only a fraction ($\eta_{ext,f}$) of the absorbed photon number and thus the chemical potential is less than V_{DB} as shown in (4.10).

$$\mu = \frac{kT}{q}\ln\left(\frac{\eta_{ext,f}J_{sc}}{J_0}\right) = V_{DB} - \frac{kT}{q}\left|\ln(\eta_{ext,f})\right| \tag{4.10}$$

According to Ref. [28, 29], the quasi-Fermi level separation of the absorber region of a solar cell is the implied open circuit voltage ($V_{i,OC}$):

$$V_{i,OC} = V_{DB} - \frac{kT}{q}\left|\ln(\eta_{ext,f})\right| \tag{4.11}$$

High $\eta_{ext,f}$ is therefore needed to realize high implied V_{oc}. The calculation of V_{DB} is tricky and will be discussed in the next section.

It seems counter-intuitive to understand that high $\eta_{ext,f}$ is needed for a high efficiency solar cell, which means that the solar cell should emit as much light as possible under open circuit conditions. However, we could understand it in the following ways. At open circuit condition, the current flow of a solar cell is zero, namely all the photo-generated electron-hole pairs recombine inside the solar cell. From material quality point of view, non-radiative recombination is a loss mechanism and it decreases the excess carrier densities and quasi-Fermi level separation. Thus the radiative recombination efficiency should be as high as possible. From the structure point of view, rather than losing the luminescence photons from the back surface (which occurs in solar cells with absorptive substrates), it is preferred to have them reflected back from the back surface and recycled again. Thus, the conclusion is that highest PL intensity is needed for high efficiency solar cells instead of longest carrier lifetime and from the previous results, it is best to dope CdTe between 5×10^{16} cm^{-3} and 1×10^{17} cm^{-3} levels for solar cell applications.

The external luminescence quantum efficiency η_{ext} is dependent on the material quality (Internal Quantum Efficiency η_{int} or Spontaneous Emission Efficiency η_{sp}) and the photon recycling γ_r and extraction γ_e factor of the structure. The Internal Quantum Efficiency (η_{int}) is defined as:

$$\eta_{int} = \frac{(1-\gamma_r)Bnp}{(1-\gamma_r)Bnp+R_{non}}, \tag{4.12}$$

and the Spontaneous Emission Efficiency (η_{sp}) is defined as follow:

$$\eta_{sp} = \frac{Bnp}{Bnp+R_{non}}. \tag{4.13}$$

The relation between η_{ext}, η_{int} *and* η_{sp} is as follows [60]:

$$\eta_{ext} = \frac{\gamma_e\eta_{int}}{1-\gamma_r} = \frac{\gamma_e\eta_{sp}}{1-\gamma_r\eta_{sp}}, \tag{4.14}$$

For the structure shown in Fig. 4.1, the $\gamma_{e,f}$ (= γ_e, there is no extraction from the back) and γ_r of the CdTe absorber layer are calculated to be 0.95 ± 0.1% and 80 ± 2% according to the method depicted in Ref. [37]. V_{DB} is calculated to be 1.22 V. Fig. 4.10 plots $\eta_{ext,f}$ vs η_{sp}, and it shows that even if η_{sp} is 100%, the $\eta_{ext,f}$ is less than 5%, due to the fact that the substrate is very absorptive. Table 4.1 shows the measured $\eta_{ext,f}$, calculated η_{sp} and $V_{i,oc}$ for CdTe/$Mg_{0.46}Cd_{0.54}Te$ DH samples with different doping concentrations. The highest $\eta_{ext,f}$ of 3.0% is observed, when the doping concentration is 1×10^{17} cm^{-3}. The highest spontaneous emission efficiency is 90%, which means that it is close to radiative limited conditions. The very high $V_{i,oc}$ also indicates its potential application in high efficiency solar cells.

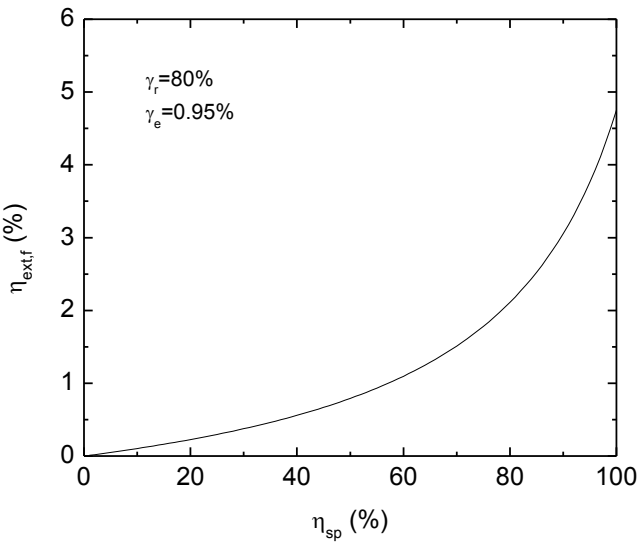

Fig. 4.10. $\eta_{ext,f}$ vs η_{sp} When γ_e = 0.95% and γ_r = 80%.

Table 4.1. Measured $\eta_{ext,f}$, Calculated η_{sp} and $V_{i,oc}$ for CdTe/$Mg_{0.46}Cd_{0.54}Te$ Double Heterostructures with Different Doping Concentrations.

Doping Concentration (cm^{-3})	undoped	1×10^{16}	6×10^{16}	1×10^{17}	6×10^{17}	1×10^{18}
τ_{eff} (μs)	0.73	0.11	0.11	0.075	0.006	0.0007
$\eta_{ext,f}$ (%)	0.68	1.5	2.1	3.0	0.54	0.09
η_{sp} (%)	45±3	71±4	80±4	90±4	39±3	8.9±0.9
$V_{i,oc}$ (V)	1.09	1.11	1.12	1.13	1.09	1.04

4.5 Optical Simulations in Solar Cells

This section talks about how to calculate the transmission, reflection and absorption in a solar cell structure using wave optics. Based on that, photon recycling and extraction factors in the absorber region can be calculated using ray-tracing method. With known optical properties of a solar cell structure, the performance such as External Quantum Efficiency (EQE) and $V_{i,OC}$ can be predicted. It is also possible to enhance the solar cell

efficiency by proper light management, such as using an anti-reflection coating, textured surface, and back reflector etc. Thus optical simulations provide very important guidance for solar cell designs.

Wave optics is a result of solving Maxwell's equations. In thin films, with known optical constants (complex refractive index), the tangential component of electric and magnetic field at each interface can be solved. The detailed theoretical derivations can be found in Ref. [61]. Here a few important equations are shown and their physical meanings are explained. The figure below shows a situation when a beam of light is shining onto the top surface of a multi-layer structure deposited onto an optically thick substrate. The arrows represent the direction of the light transmission through each layer. The + sign represents light traveling to the bottom layers and the – sign represents light traveling to the top layers. Since the substrate is thick, it is assumed that there is no light coming from the back side of the substrate. The numbers 0, 1, 2, etc. are the index numbers of each medium and there are in total N layers on top of the substrate. The letters a, b, c, etc. represent the interfaces between each two layers.

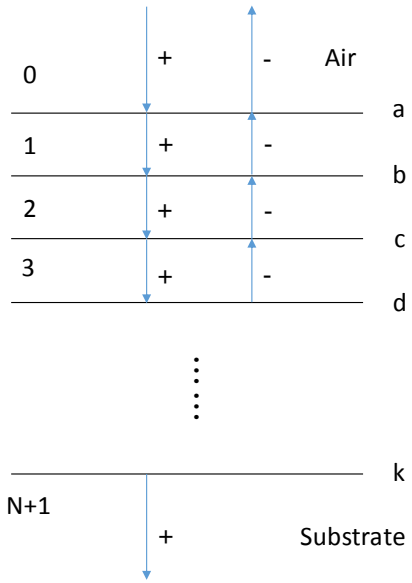

Fig. 4.11. A Diagram Illustrating How Light is Transmitted Through a Multi-layer Structure.

The tangential component of electric and magnetic field at any of the adjacent interfaces can be correlated as shown in the equation below:

$$\begin{bmatrix} E_a \\ H_a \end{bmatrix} = \begin{bmatrix} cos\delta_1 & isin\delta_1/\eta_1 \\ i\eta_1 sin\delta_1 & cos\delta_1 \end{bmatrix} \begin{bmatrix} E_b \\ H_b \end{bmatrix} \tag{4.15}$$

where E_a, H_a, E_b and H_b are the total tangential components of electric and magnetic field at interface a and b, respectively. $\delta_1 = 2\pi N_1 d_1 cos\theta_1/\lambda$ is the phase shift factor, $\eta_1 = \frac{N_1 \mathcal{y}}{cos\theta_1}$ is the tilted optical admittance for p-polarized waves, and $\eta_1 = N_1 \mathcal{y} cos\theta_1$ is for s-polarized waves. $N_1 = n_1 - ik_1$ represents the complex refractive index, θ_1 is the incident angle, d_1 is the layer thickness, and $\mathcal{y} = 2.6544\times10^{-3}\ S$ is a constant which is ratio of magnetic and electric field in free space.

The matrix in equation (4.15) is called the characteristic matrix, which is very important to the entire thin film optics theory. Similar to the relation in (4.15)

$$\begin{bmatrix} E_b \\ H_b \end{bmatrix} = \begin{bmatrix} cos\delta_2 & isin\delta_2/\eta_2 \\ i\eta_2 sin\delta_2 & cos\delta_2 \end{bmatrix} \begin{bmatrix} E_c \\ H_c \end{bmatrix} \tag{4.16}$$

……

$$\begin{bmatrix} E_{k-1} \\ H_{k-1} \end{bmatrix} = \begin{bmatrix} cos\delta_N & isin\delta_N/\eta_N \\ i\eta_N sin\delta_N & cos\delta_N \end{bmatrix} \begin{bmatrix} E_k \\ H_k \end{bmatrix} \tag{4.17}$$

Thus the electric and magnetic field can be correlated between interface a and k.

$$\begin{bmatrix} E_a \\ H_a \end{bmatrix} = M_1 M_2 \cdots M_N \begin{bmatrix} E_k \\ H_k \end{bmatrix}, \tag{4.18}$$

$$\begin{bmatrix} E_a \\ H_a \end{bmatrix} = M_1 M_2 \cdots M_N \begin{bmatrix} 1 \\ \eta_{N+1} \end{bmatrix} E_k \tag{4.19}$$

$$\begin{bmatrix} E_a/E_k \\ H_a/E_k \end{bmatrix} = M_1 M_2 \cdots M_N \begin{bmatrix} 1 \\ \eta_{N+1} \end{bmatrix} = \begin{bmatrix} B_a \\ C_a \end{bmatrix} \tag{4.20}$$

where M_i is the characteristic matrix. Similarly, for interface b

$$\begin{bmatrix} E_b/E_k \\ H_b/E_k \end{bmatrix} = M_2 \cdots M_N \begin{bmatrix} 1 \\ \eta_{N+1} \end{bmatrix} = \begin{bmatrix} B_b \\ C_b \end{bmatrix} \tag{4.21}$$

To calculate the total reflectance (fraction of light that is reflected back to free space) and transmittance (fraction of light that is absorbed by the substrate):

$$R = \left(\frac{\eta_0 B_a - C_a}{\eta_0 B_a + C_a}\right)\left(\frac{\eta_0 B_a - C_a}{\eta_0 B_a + C_a}\right)^* \tag{4.22}$$

$$T = \frac{4\eta_0 Re(\eta_{N+1})}{(\eta_0 B_a + C_a)(\eta_0 B_a + C_a)^*} \tag{4.23}$$

To calculate the absorptance in each individual layer, the Poynting Vector has to be used. The Poynting Vector ($\boldsymbol{S}$) represents the instantaneous rate of the energy flow of an electromagnetic wave across unit area:

$$\boldsymbol{S} = \boldsymbol{E} \times \boldsymbol{H} \tag{4.24}$$

where ***E*** and ***H*** are electric and magnetic field vector respectively. For a harmonic wave, it is found that the irradiance *I*, which is the average intensity of the Poynting Vector, is in the following simple form:

$$I = \frac{1}{2} Re(EH^*) \tag{4.25}$$

where *E* and *H* are the amplitudes of electric and magnetic fields respectively. With equation (4.25), light irradiance at each interface can be calculated and the absorptance of each layer can be calculated based on the irradiance difference at two adjacent interfaces. For example, for layer 1, the aborptance is in the following form:

$$A_1 = \frac{I_a - I_b}{I_a/(1-R)} \tag{4.26}$$

Similarly,

$$A_2 = \frac{I_b - I_c}{I_a/(1-R)} \tag{4.27}$$

$$A_3 = \frac{I_c - I_d}{I_a/(1-R)} \tag{4.28}$$

……

In a solar cell structure, once the absorptance is calculated against energy, EQE can be simulated as will be shown in the next section. The V_{DB} can also be calculated according to (4.9). Here the equation is shown again:

$$V_{DB} = \frac{kT}{q} \ln(\frac{J_{sc}}{J_0}) = \frac{kT}{q} \ln(\frac{\int A_1(E)S(E)dE}{\int A_2(E)b(E)dE}), \tag{4.9}$$

where $A_1(E)$ represents the normal incidence absorptance and can be calculated easily using wave optics. The solar spectrum $S(E)$ of AM1.5G can be found online and the background blackbody radiation can be represented using the following equation:

$$b(E) \approx \frac{2\pi n^2 E^2}{h^3 c^2} \exp(-\frac{E}{kT}) \tag{4.29}$$

$A_2(E)$ represents the incident angle averaged absorptance, since J_0 is the dark current due to absorption of background photons from all directions [29].

$$J_0 = q \iiint A(E,\theta)\Phi_b(E,\theta)(sin\theta d\theta d\varphi)dE \tag{4.30}$$

$$\Phi_b(E,\theta) \approx \frac{2n^2E^2}{h^3c^2}\exp(-\frac{E}{kT})cos\theta \tag{4.31}$$

where $A(E,\theta)$ is the angle dependent absorptance, $\Phi_b(E,\theta)$ is the photon flux density per unit energy per solid angle (#/(cm^2·s·eV·sr)). Since the irradiance distribution of the surface of a black body is Lambertian, there is a term of $cos\theta \cdot sin\theta \cdot d\theta \cdot d\varphi$ is the differential element of solid angle. According equation (4.6) and (4.29) ~ (4.31), $A_2(E)$ is thus in the following form:

$$A_2(E) = \int_0^{\pi/2} A(E,\theta)\, cos\theta sin\theta d\theta / \int_0^{\pi/2} cos\theta sin\theta d\theta \tag{4.32}$$

The wave optics provides a way to calculate the total reflectance and transmittance of a multi-layer structure, and it is also useful for the calculation of photon recycling and extraction factors. These two factors (γ_r and γ_e) represent the average probability of radiative recombination generated photons in the absorber region to be reabsorbed and extracted respectively. Since they are averaged values, photons with different energies, emitted at different positions and directions have to be accounted for. The detailed calculations used in the ray-tracing method are described in Ref. [37]. A brief discussion below is used to help the reader(s) understand the calculations used in the ray-tracing method.

Fig. 4.12 shows a schematic structure of the absorber region of a solar cell. Radiative recombination generated photons at a volume dV can be emitted in any direction. The red line represents a situation when a photon is emitted in direction θ, reflected back from the

front surface and then re-absorbed. The blue arrow represents another photon that is emitted at a different position in direction θ', this photon was able to escape the front surface of the solar cell after being reflected twice within the absorber region.

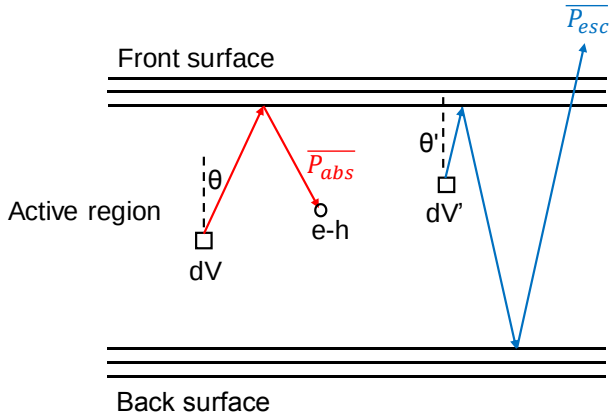

Fig. 4.12. Schematic Diagram of the Absorber Region of a Solar Cell.

The reflectance and transmittance at the top and bottom surfaces can be calculated using wave optics. The escape and re-absorption probability of a photon, with energy E, emitted in location x, and in direction θ, can be calculated using ray-tracing. The photon recycling and extraction factor is then the average value of the escape and re-absorption probability, represented by the following equations:

$$\gamma_e = \int_0^\infty \hat{S}(E) \int_0^{\pi/2} \frac{T_f}{2\alpha L} \frac{(1-e^{-\alpha L/cos\theta})(1+R_b e^{-\alpha L/cos\theta})}{1-R_f R_b e^{-2\alpha L/cos\theta}} cos\theta sin\theta d\theta dE \tag{4.33}$$

$$\gamma_r = 1 - \int_0^\infty \hat{S}(E) \int_0^{\frac{\pi}{2}} \frac{(1-e^{-\alpha L/cos\theta})}{\alpha L} \{1 - \frac{1}{2}(1 - e^{-\alpha L/cos\theta})(\frac{R_f+R_b+2R_f R_b e^{-\alpha L/cos\theta}}{1-R_f R_b e^{-2\alpha L/cos\theta}})\} cos\theta sin\theta d\theta dE \tag{4.34}$$

where $\hat{S}(E)$ is the normalized PL emission spectrum, T_f, T_b and R_f, R_b are the transmittance and reflectance at the front and back surfaces.

4.6 Application in CdTe Solar Cells

With such a high $V_{i,oc}$ in n-type CdTe/$Mg_{0.46}Cd_{0.54}Te$ DHs, a solar cell with efficiency as high as 17.0% , and a record breaking V_{oc} of 1.096 V was demonstrated [19]. Due to the limitations of our MBE chamber, we have to rely on other groups to grow the p-type contact layer on top of our n-type absorber materials.

An initial effort was attempted [62], with a ZnTe(p)/CdTe(p)/CdTe(n)/$Mg_{0.24}Cd_{0.76}Te$(n)/CdTe(n)/InSb(n) structure, in which the ZnTe(p)/CdTe(p) contact layers were grown at Rensselaer Polytechnic Institute. Its efficiency was 10.9% and its V_{oc} was only 0.759 V. Such a low V_{oc} is in contradictory with the high implied V_{oc} for n-type CdTe/$Mg_xCd_{1-x}Te$ DHs, and theoretical simulation indicates that it is due to the strong recombination at the p-n junction interfaces. This means that even if the absorber material has very high quality, a poor p-n junction region could dramatically decrease the SRH recombination lifetime and thus the device performance.

Therefore, a new structure is proposed, which adds a thin intrinsic $Mg_xCd_{1-x}Te$ layer between the p-n junction to reduce the junction recombination. The device structure is like this, ITO/a-Si:H(p)/$Mg_xCd_{1-x}Te$(i)/CdTe(n)/$Mg_yCd_{1-y}Te$(n)/CdTe(n)/InSb(n) [19]. The ITO/a-Si:H(p) contact layers are deposited by Prof. Holman's group at Arizona State University. The interface between ITO and a-Si:H(p) is a tunnel junction. The band edge alignment of the device under equilibrium is shown in the below figure. During the operation of this device, the thin intrinsic $Mg_xCd_{1-x}Te$ layer acts as a hole selective layer, which blocks the majority carriers (electrons) and allow minority carriers (holes) in the absorber to either tunnel or thermionically emit over the small valance band barrier

potential to the p-type emitter. The interface quality between CdTe and $Mg_xCd_{1-x}Te$ is high, which prevents the recombination of minority carriers in the p-n junction region. Once the minority carriers transport through the $Mg_xCd_{1-x}Te$(i) layer, they become majority carriers on the a-Si:H(p) side. This idea is very similar to that in HIT (Heterostructure with Intrinsic Thin Layer) solar cells, where the combination of doped a-Si:H/intrinsic a-Si:H layers act as selective contacts to extract minority carriers.

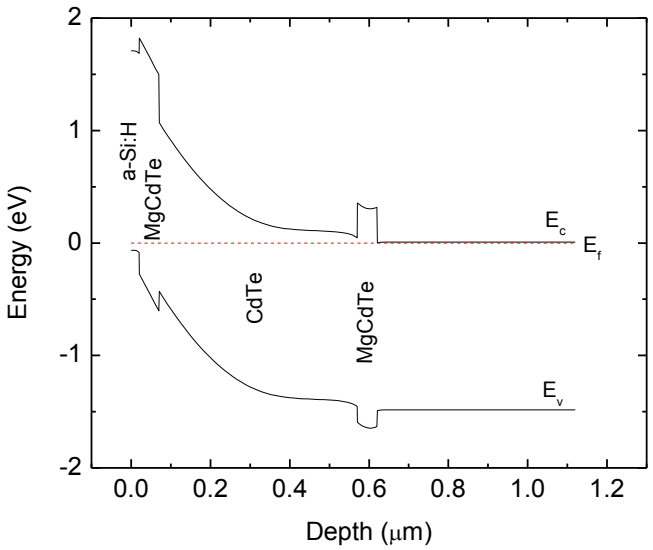

Fig. 4.13. Equilibrium Band Edge Diagram of an ITO/a-Si:H(p)/$Mg_xCd_{1-x}Te$(i)/CdTe(n)/$Mg_yCd_{1-y}Te$(n)/CdTe(n)/InSb(n) Solar Cell Device.

Fig. 4.14. shows the current density (J) vs voltage (V) curve of the most efficient cell at the time of writing this dissertation. The efficiency is 18.5%, with J_{sc}=22.4 mA/cm^2, V_{oc}=1.089 V and FF=75.7%. Such a high V_{oc} is in agreement with the high implied V_{oc} measured for CdTe/$Mg_xCd_{1-x}Te$ DHs and is also the highest ever reported for CdTe solar

cells. Fig. 4.15 shows the measured EQE and simulated photon current losses by the absorptance calculation method as discussed above. It can be seen that the measured EQE curve agrees very well with the calculated one, meaning that all the carriers generated in the CdTe active layer are effectively collected. This cell utilizes a double layer anti-reflection coating (80 nm SiO_x/55 nm ITO) and the reflection loss is thus only 0.5 mA/cm^2; the parasitic absorption loss by ITO, a-Si:H and top $Mg_xCd_{1-x}Te$ layers could be reduced by improving the material quality, optimizing their thickness, or using a wider band gap p-type contact material; transmission loss can be reduced by growing thicker CdTe absorber layer.

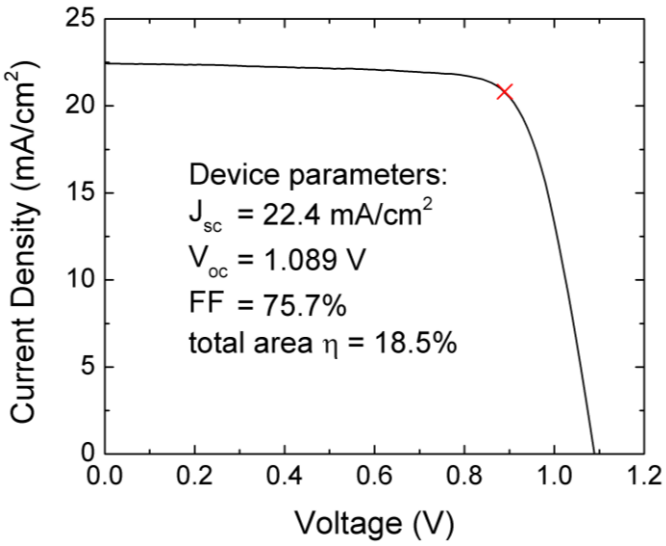

Fig. 4.14. Light J-V Curve of the Most Efficient Cell.

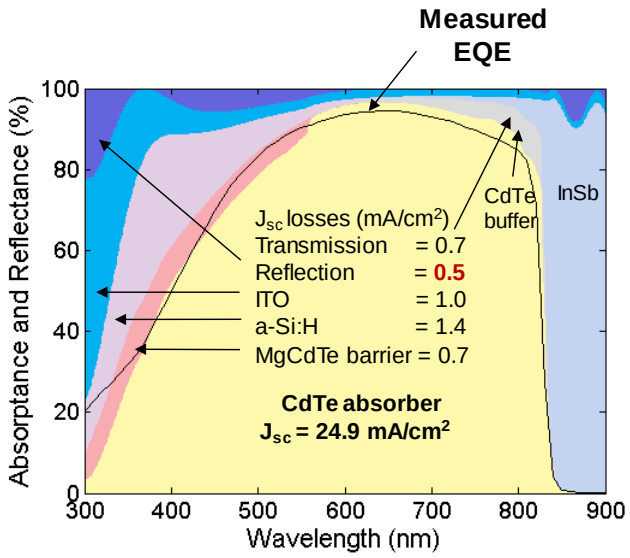

Fig. 4.15. Measured EQE and Calculated Absorptance Spectrum for the Highest Performing CdTe Solar Cell Device.

There is a trade-off between having thicker and higher $Mg_xCd_{1-x}Te$ barrier layer vs. having thinner and lower $Mg_xCd_{1-x}Te$ barrier. With the former case, the carrier confinement is better which could enable higher implied V_{oc}, but the carrier transport will be worse which could result in smaller FF and lower output voltage. Thus optimizing the thickness and composition of the $Mg_xCd_{1-x}Te$ barrier layer is needed to have both high V_{oc} and FF. It may be hard for $Mg_xCd_{1-x}Te$, since it has a type-I band alignment with CdTe, i.e. it is hard to optimize the confinement of one type of carrier while optimizing the transport of the other type of carrier at the same time. Thus we have to use a different p-type contact material in the future, which has a lower valance band edge compared with a-Si:H, to improve the transport of holes at the p-n junction region. It is also needed to dope the $Mg_yCd_{1-y}Te$ bottom barrier heavily to improve the transport of electrons at the back surface field layer.

4.7 Conclusions

This chapter summarizes the study of optical (photoluminescence, carrier lifetime, and external luminescence quantum efficiency) and electrical (carrier vs. doping concentration) properties of In-doped CdTe/$Mg_{0.46}Cd_{0.54}Te$ double heterostructures, and how a full understanding of material properties leads to the development of a record breaking solar cell device with 18.5% efficiency and V_{oc}=1.089 V. This is a perfect example showing how material characterization can be beneficial for the design of devices and the prediction of device performance. V_{oc} of the cell is almost very close to the calculated implied V_{oc} and J_{sc} can be further improved by reducing parasitic absorptions. Both V_{oc} and FF can be enhanced by improving charge transport. In addition, important optical simulation methods are discussed for the calculation of absorptance, photon recycling and extraction factors in a solar cell structure.

Chapter 5

LUMINESCENCE REFRIGERATION IN CDTE

5.1 Materials for Luminescence Refrigeration

During luminescence refrigeration (or laser cooling) of a solid, heat is removed by the process of anti-Stokes fluorescence, when the average emitted photon energy exceeds the excitation photon energy. The emitted photon energy is higher, since the excited carriers need to absorb phonons in order to reach the thermal equilibrium state (Fermi Distribution). This idea was first proposed by Pringsheim in 1929 [63] and the first observation of luminescence refrigeration of solids is in ytterbium-doped fluorozirconate glass (Yb^{3+}:ZBLANP) in 1995 [64]. The high purity ZBLANP glass host, was originally developed for long-haul optical fiber applications. In 2005, using the same material, cooling to 208 K was realized [65]. Various Yb:host combinations have been reported to have cooling effect, and to find a complete list of the materials used please see Ref. [66, 67]. In addition, cooling in glass doped with rare-earth ions of thulium and erbium has been reported [68,69]. Among all the materials studied, Yb^{3+}:YLF (Yttrium-Lithium-Fluoride) exhibits the most promising properties and cooling results. The record cooling temperature has been pushed down from 155 K in 2010 [70], to 119 K in 2013 [71] and to 91 K in 2016 [72], by continuously optimizing host material purity, increasing the Yb doping concentration, optimizing laser absorption and minimizing heat loads. The potential application of luminescence refrigeration could be in space-based applications.

For semiconductors, luminescence refrigeration has been only observed in CdS nano-ribbons reported in 2013 [73]. The successful cooling by 40 K was attributed to the strong coupling between exciton and Longitudinal-Optical-Phonons, high external quantum

efficiency, and negligible background absorption for the CdS nano-ribbons. Despite many theoretical works [74, 75], no luminescence refrigeration effect has been realized in other semiconductor materials such as GaAs, even though high internal (99.7%) and external (96%) quantum efficiencies have been reported for GaAs/GaInP double heterostructures (DHs) [30, 76]. Similar to GaAs/GaInP DHs, CdTe/$Mg_xCd_{1-x}Te$ DHs exhibit great material qualities with ultra-long carrier lifetime (3.6 μs) and low interface recombination velocity (1 cm/s), which could potentially enable luminescence refrigeration. The following table compares the properties of 4 different materials that have enabled, or could potentially enable luminescence refrigeration effects.

Table 5.1. Comparison of 4 Different Materials That Have Been Used or Could Potentially Be Used for Luminescence Refrigeration.

Materials	Yb^{3+}:YLF [70, 72]	CdS nano-ribbon [73]	GaAs/$Ga_{0.51}In_{0.49}P$ [76]	CdTe/$Mg_{0.46}Cd_{0.54}Te$
Pump Wavelength (nm)	1020	514	888	840
Room Temperature λ_{PL} (nm)	998	506	866	820
Room Temperature α (cm^{-1})	1	NA	~2×10^2	~2×10^2
α_i (cm^{-1})	<1×10^{-4}	NA	NA	NA
η_{sp}	NA	NA	99.5% (Δn=8e17)	~99%
η_{ext}	99.6%	>99%	96%	NA
Lowest Temperature (K)	91	254	NA	NA

n	1.5	2.8	3.6	2.9

5.2 High Spontaneous Quantum Efficiency

To realize luminescence refrigeration in a solid, the necessary condition is that the average emitted photon energy must be larger than the excitation photon energy (anti-Stokes fluorescence). Also the external quantum efficiency (η_{ext}) has to be very high, which requires both high spontaneous emission efficiency (η_{sp}) and high photon extraction factor (γ_e). If one excited electron-hole pair recombines non-radiatively, it will generate heat (~E_g) inside the material, which is equal to many times the heat (~kT) taken away by anti-Stokes process. The cooling efficiency η_c is defined and derived as follows:

$$\eta_c = \frac{P_{out}-P_{in}}{P_{in}},$$

$$= \frac{\eta_{ext}P_{in}(\frac{\alpha}{\alpha_i+\alpha})(\frac{h\bar{\upsilon}_{out}}{h\nu_{in}})-P_{in}}{P_{in}},$$

$$= \eta_{ext}(\frac{\alpha}{\alpha_i+\alpha})\left(\frac{h\bar{\upsilon}_{out}}{h\nu_{in}}\right) - 1, \qquad (5.1)$$

where α and α_i are band to band and parasitic absorption coefficients, respectively. $h\nu_{in}$ and $h\bar{\upsilon}_{out}$ are input photon energy and average output photon energy, respectively. Thus high external quantum efficiency, strong band to band absorption and very week parasitic absorption are the keys to luminescence refrigeration in a solid.

Assuming α_i is negligible compared with α, to have cooling effect, η_c should be larger than zero and thus

$$\eta_{ext} > \frac{h\nu_{in}}{h\bar{\upsilon}_{out}}. \qquad (5.2)$$

For monocrystalline CdTe, the bandgap is 1.49 eV, and with excitation laser energy ½ *kT* smaller than the bandgap, and PL peak energy *kT* larger than the bandgap, to realize cooling,

$$\eta_{ext} > 97.5\%. \tag{5.3}$$

For CdTe/$Mg_xCd_{1-x}Te$ DHs grown on an InSb wafer, since the substrate is absorptive for the photons emitted by CdTe, it is impossible to have high η_{ext}, even if η_{sp} is 100%. However, it is still worth looking at the η_{ext} and η_{sp} of the best quality samples, since we can work on the optical design to enhance photon extraction factor and, therefore η_{ext} in the future.

Excitation-dependent quantum efficiency measurements are carried out for the sample below, shown in Fig. 5.1. According to recombination theory, the recombination rate of different mechanisms (SRH, radiative and Auger) change differently depending on excitation or excess carrier density. Therefore, excitation-dependent measurement is necessary to evaluate the proportion of the three recombination mechanisms and thus, spontaneous emission efficiency. The sample shown here has a record long carrier lifetime of 3.6 μs and is undoped with a background carrier concentration of ~10^{14} cm^{-3}. A 532 nm laser is used as an excitation source and its power density is varied from 0.8 to 80 sun. The absorptance of this sample at 532 nm is 70% (70% of the incident photons are absorbed in the CdTe middle layer). The photon recycling factor γ_r (70%) and photon extraction factor γ_e (1.4%) are calculated based on the ray-tracing method as discussed in the previous chapter [37].

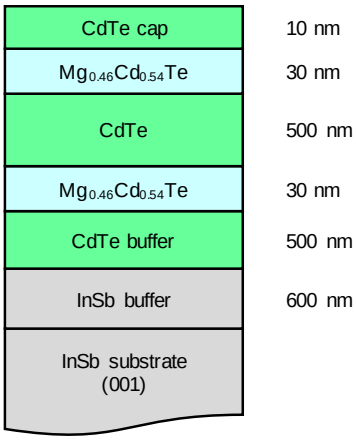

Fig. 5.1. The Hero CdTe/$Mg_{0.46}Cd_{0.54}Te$ Double Heterostructure with 3.6 μs Lifetime.

Fig. 5.2 shows the η_{ext} vs. η_{sp} curve based on the calculated γ_e and γ_r values, and Table 5.2 shows the measured η_{ext} and the corresponding η_{sp}. As the excitation power density increases, the external luminescence quantum efficiency η_{ext} increases and saturates at 4.6%. According to the calculated η_{ext} vs. η_{sp} curve, however, the highest η_{ext} is only 4.5% even when η_{sp} is 100%. The discrepancy could be due to the error bar of the calculated photon recycling and extraction factors (which is related to the optical constants used), and also error bar in the measurement of η_{ext} (which could be related to the errors bars of the detector responsivity curve and also calculated absorptance). Excess carrier density Δn is also estimated based on generation rate inside the CdTe layer. It is found that when power density increases by two orders of magnitude, the excess carrier density increases by only one order of magnitude indicating that radiative recombination dominates ($R_{rad}=B\Delta n^2$).

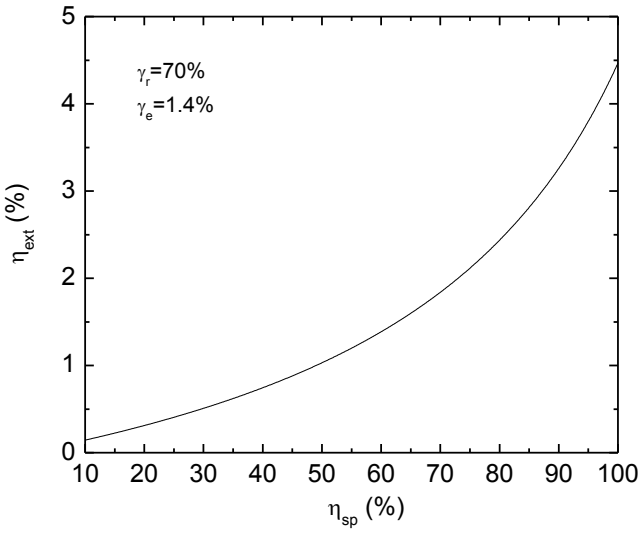

Fig. 5.2. External Luminescence Quantum Efficiency (η_{ext}) vs Spontaneous Emission Efficiency (η_{sp}) for the Structure Shown in Fig. 5.1.

Table 5.2. Excitation-Dependent External Luminescence Quantum Efficiencies for a $CdTe/Mg_{0.46}Cd_{0.54}Te$ Double Heterostructure with 3.6 μs Lifetime.

Power density (mW/cm^2)	79.6	159	478	1590	4780	7960
η_{ext} (%)	3.3	3.6	4.0	4.2	4.6	4.6
η_{sp} (%)	90	93	97	98	~100	~100
Estimated Δn (cm^{-3})	3×10^{15}	4×10^{15}	7×10^{15}	1×10^{16}	2×10^{16}	3×10^{16}

Fig. 5.3. shows the generation rate vs. PL intensity in a log-log scale. The generation rate is calculated based on the absorptance of the CdTe layer and the power density of the laser. According to the ABC model (introduced in the previous chapter), the recombination is 100% dominated by radiative recombination when the slope is 1, which demonstrates that the sample is radiative recombination dominated at an about 80 sun excitation level.

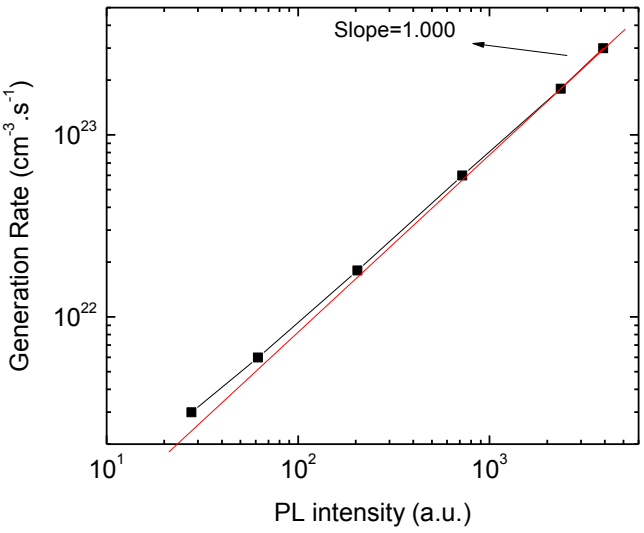

Fig. 5.3. Generation Rate vs. Photoluminescence Intensity for the CdTe/$Mg_{0.46}Cd_{0.54}Te$ Double Heterostructure with 3.6 μs Lifetime. According to ABC Model, the Recombination is ~100% Radiative Dominated When the Slope Is 1.

5.3 Optimal Injection Level

To achieve the highest external luminescence quantum efficiency, the spontaneous emission efficiency should be maximized first. For an n-type semiconductor material, the spontaneous emission efficiency is expressed in the following equation:

$$\eta_{sp} = \frac{B(n_0+\Delta n)\Delta n}{A\Delta n+B(n_0+\Delta n)\Delta n} \tag{5.4}$$

At low injection level:

$$\eta_{sp} = \frac{Bn_0}{A+Bn_0} \tag{5.5}$$

At high injection level:

$$\eta_{sp} = \frac{B\Delta n}{A+B\Delta n} \tag{5.6}$$

The above equations ignored Auger recombination and η_{sp} increases as the injection level Δn increases. At high injection level, where the doping concentration doesn't affect η_{sp}, materials with lower doping concentrations have higher η_{sp} than those with higher doping concentrations, since A is smaller for lightly doped material. Thus the conclusion is that for luminescence refrigeration application, it is preferred to use undoped materials at high injection levels.

However, as mentioned above, Auger recombination will eventually kick in at a much higher injection level, which means that Δn should not be infinitely high. We can calculate η_{sp}, by assuming $\tau_{SRH} = 5\,\mu s$, $B = 10^{-9}\,cm^3.s^{-1}$, and $C = 10^{-29}\,cm^6.s^{-1}$ for an undoped CdTe sample. Fig. 5.4 shows the simulation results, which reveal η_{sp}=99.7% at a 10^{17} cm^{-3} injection level. The increase of η_{sp} when Δn increases from 10^{15} cm^{-3} to 10^{17} cm^{-3} is due to the increased radiative recombination rate, while the decrease of η_{sp} above the 10^{17} cm^{-3} injection level is due to Auger recombination. To achieve such a high Δn is not easy, since the absorption coefficient at 1/2 kT below the bandgap of CdTe is only 200 cm^{-1}. High power lasers with a well-focused beam size should be used and a cavity should be designed so that light could at least have multiple passes through the active region of the sample to ensure full absorption.

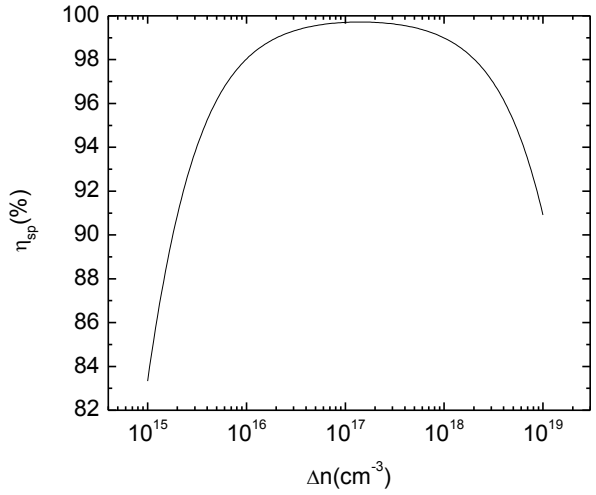

Fig. 5.4. Simulated η_{sp} as a Function of Injection Level Δn for an Undoped CdTe.

5.4 Enhancing Extraction Efficiency

Even with 99.7% spontaneous emission efficiency, external luminescence quantum efficiency can still be low if photons cannot be effectively extracted. To enhance photon extraction, methods such as adding back reflectors, textured surface, or adding a refractive index matching dome, could be used. In the following discussions, a series of structures are studied in order to understand how different optical designs could affect the photon recycling and extraction factor and thus, the external luminescence quantum efficiency.

Fig. 5.5 shows all the structures evaluated. Structure A is the as grown CdTe/$Mg_xCd_{1-x}Te$ DH. As already discussed previously, the substrate is absorptive for CdTe's luminescence, thus the external luminescence quantum efficiency could be very low (<10%) even when the CdTe middle layer is 100% dominated by radiative recombination. Structures B and C, which add a back reflector layer and textured surfaces, are compared with structure A. Structures D through H all used a refractive index matched

dome structure in order to enhance light extraction. The simulation results for each structure will be discussed in the following paragraphs.

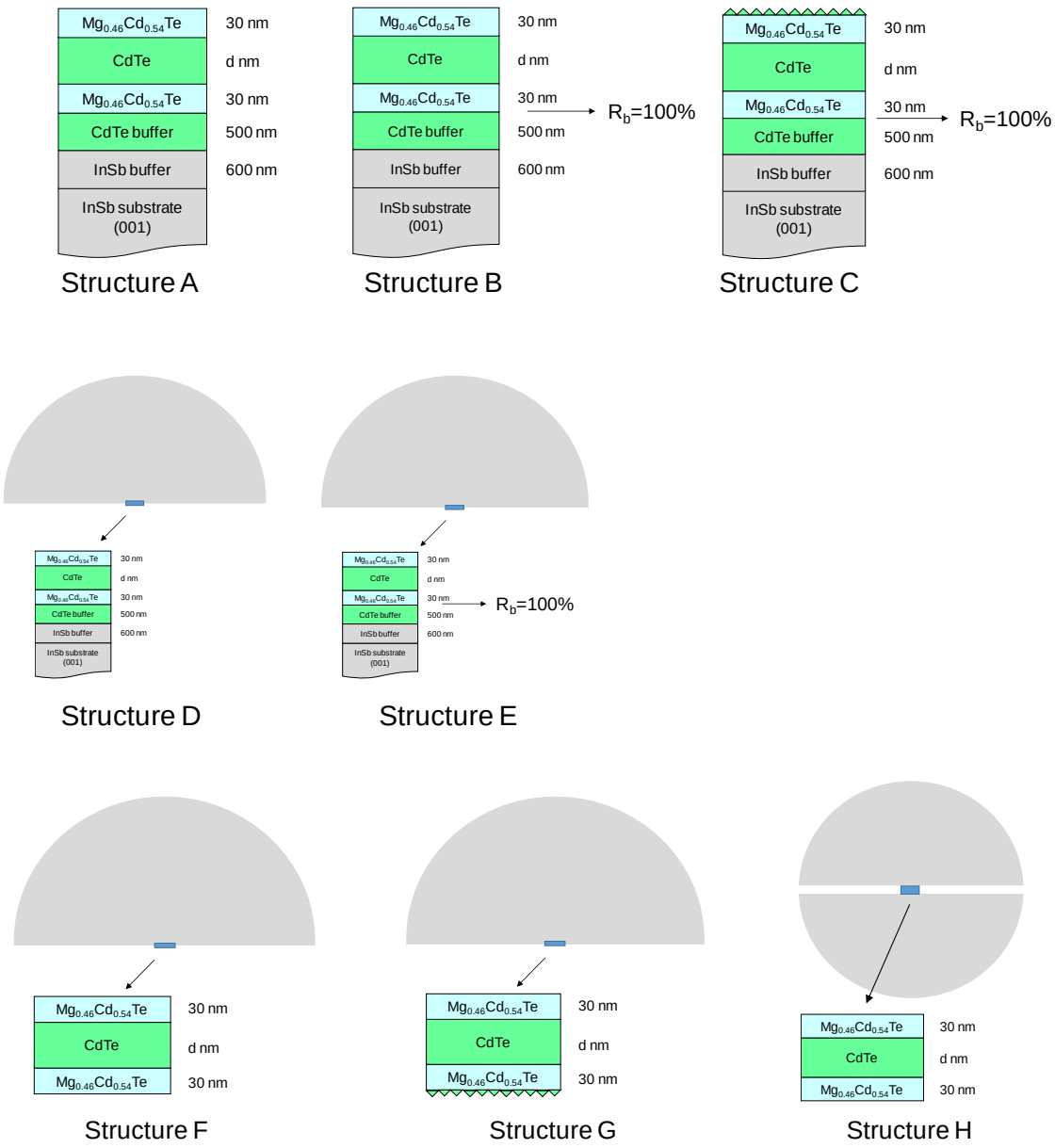

Fig. 5.5. Different Structures for External Luminescence Quantum Efficiency Evaluation.

For structure A, the reflectance (as a function of photon energy and incident angle) at the top and bottom surface of the CdTe middle layer is shown in Fig. 5.6 and Fig. 5.7. Since the refractive index of CdTe (2.9) is very different from that of air (1), the total internal reflection happens at an incident angle of around 20 degrees. Thus most of the light is reflected back when it is incident on the front surface. However, for the back surface, light can transmit more easily to the substrate, since the bottom layers have better index matching with CdTe. These illustrate why the external luminescence quantum efficiency is very low for our CdTe/$Mg_xCd_{1-x}Te$ DHs, even though the sample is dominated by radiative recombination.

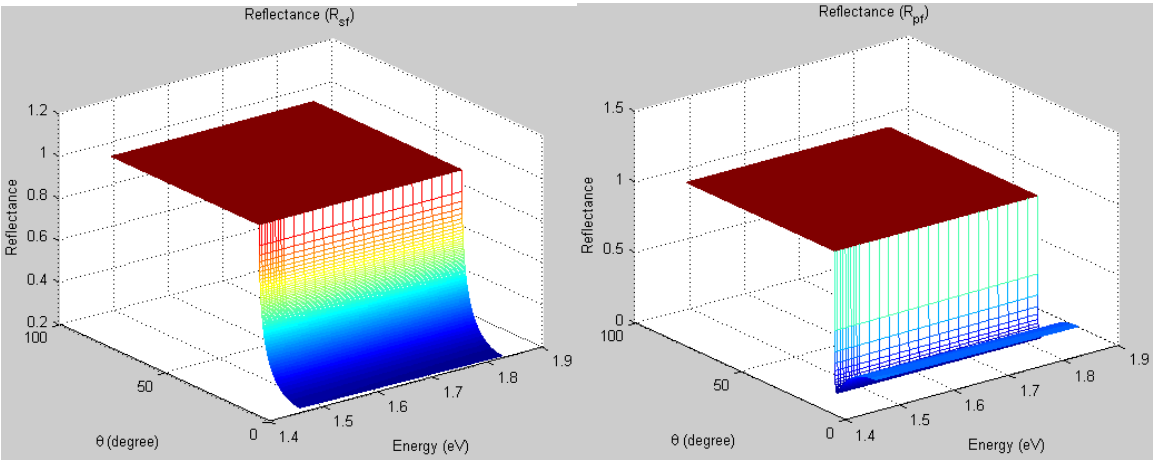

Fig. 5.6. Reflectance, S-polarized (Left) and P-polarized (Right), of the Top Surface of the CdTe Middle Layer in Structure A.

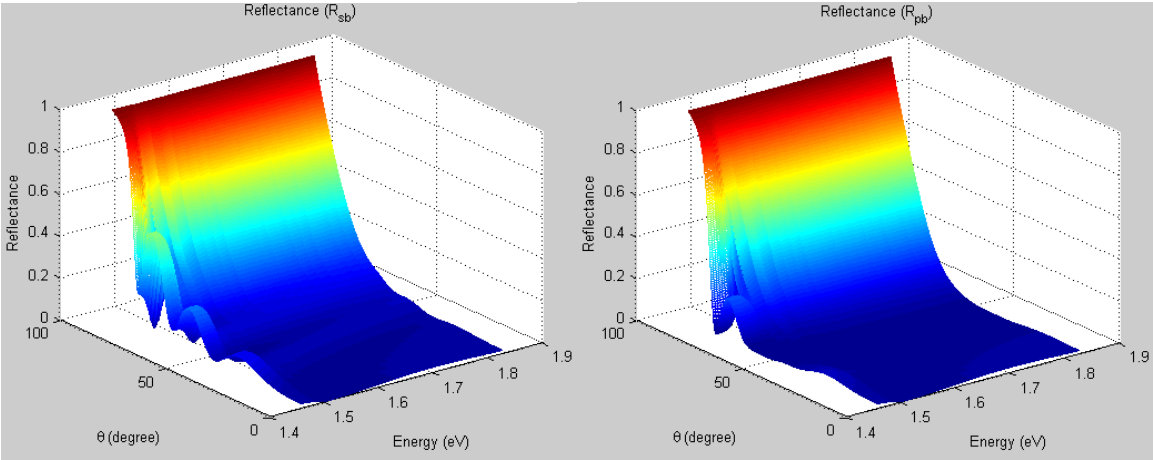

Fig. 5.7. Reflectance, S-polarized (Left) and P-polarized (Right), of the Bottom Surface of the CdTe Middle Layer in Structure A.

The front surface photon extraction ($\gamma_{e,f}$) and photon recycling (γ_r) factors are plotted vs. the middle CdTe layer thickness in Fig. 5.8. With a thicker layer, $\gamma_{e,f}$ becomes smaller and γ_r becomes bigger, since the luminescence photons have a higher probability of being re-absorbed with a thicker CdTe layer. The $\gamma_{e,f}$ is only around 2% when the layer is infinitely thin, since that is the ratio of escape solid angle from the front surface to the total solid angle in all directions ($1/4n^2$).

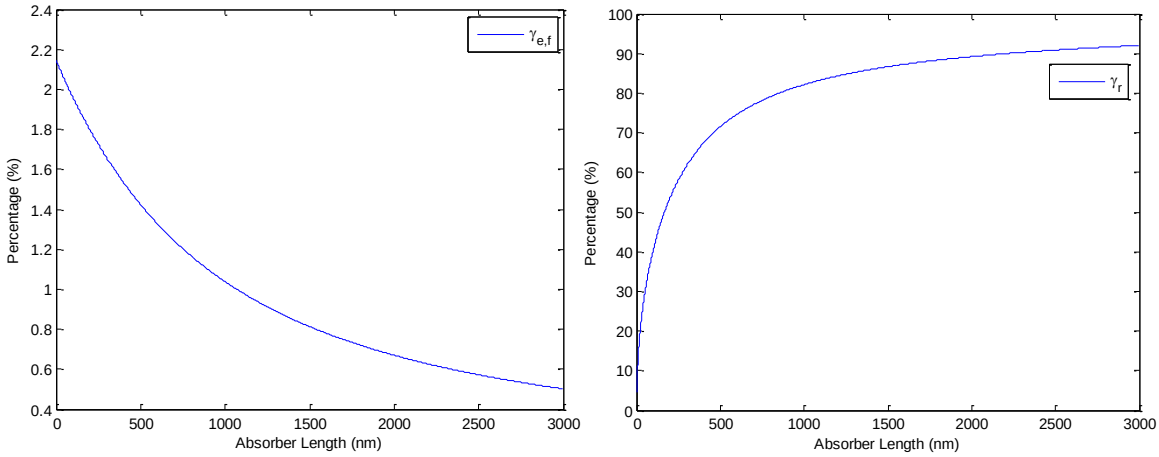

Fig. 5.8. Photon Extraction (Left) and Recycling (Right) Factor vs. Middle CdTe Layer Thickness for Structure A.

Fig. 5.9 shows the external luminescence quantum efficiency (η_{ext}) vs. the CdTe layer thickness for structure A. The left shows the case when η_{sp}=99.9%, and it is found that η_{ext} increases as the CdTe layer increases. That's because, since the material is almost perfect (without SRH recombination), thicker CdTe helps to increase the percentage of photons emitting in top direction. According to thermodynamics, when the CdTe layer is infinitely thick, and without SRH recombination, the ratio of radiation to the top surface and to the bottom substrate is 1:n^2. Thus the maximum η_{ext} should not be higher than 10% for structure A. The right shows the case when η_{sp}=99%, and η_{ext} has a peak value at CdTe layer thickness of ~1500 nm. Non-radiative recombination is the reason that η_{ext} starts to decrease when CdTe is thicker. For both cases, the η_{ext} is much less than 10%, since the substrate of the structure is absorptive. Thus it is not possible to directly use the CdTe/$Mg_xCd_{1-x}Te$ DH on InSb structure for luminescence refrigeration.

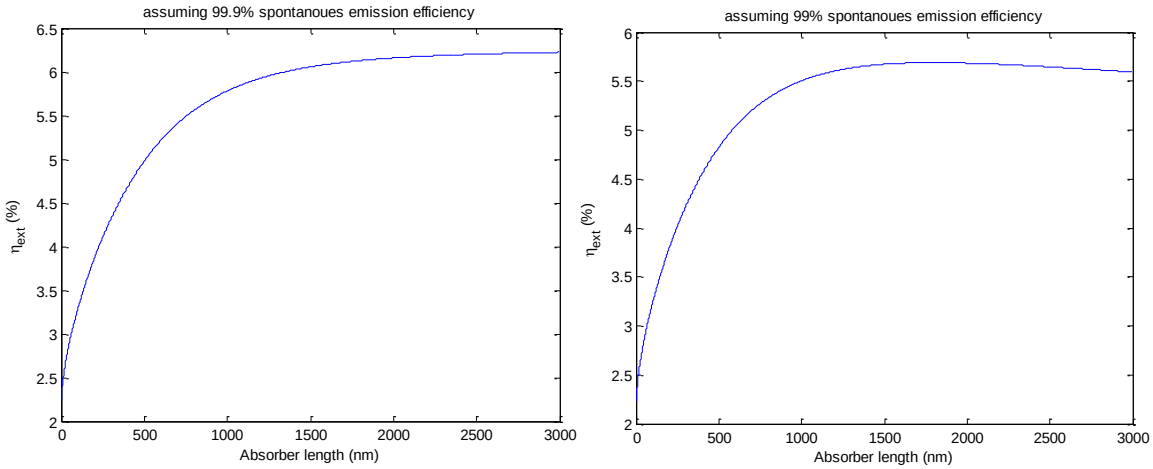

Fig. 5.9. External Luminescence Quantum Efficiency vs. CdTe Middle Layer Thickness of Structure A. Left Assumes the Spontaneous Emission Efficiency Is 99.9%, While Right Assumes That It Is 99%.

Compared with structure A, structure B added a 100% perfect reflector to the back of the CdTe/$Mg_xCd_{1-x}Te$ DH. Both $\gamma_{e,f}$ and γ_r are greatly enhanced as is shown in Fig. 5.10, since there is no loss to the substrate. The η_{ext} is plotted in Fig. 5.11, and it decreases with thicker CdTe layer, due to non-radiative recombination. The η_{ext} can meet the cooling condition (>97.5%), only when the CdTe layer is very thin with η_{sp}=99.9%.

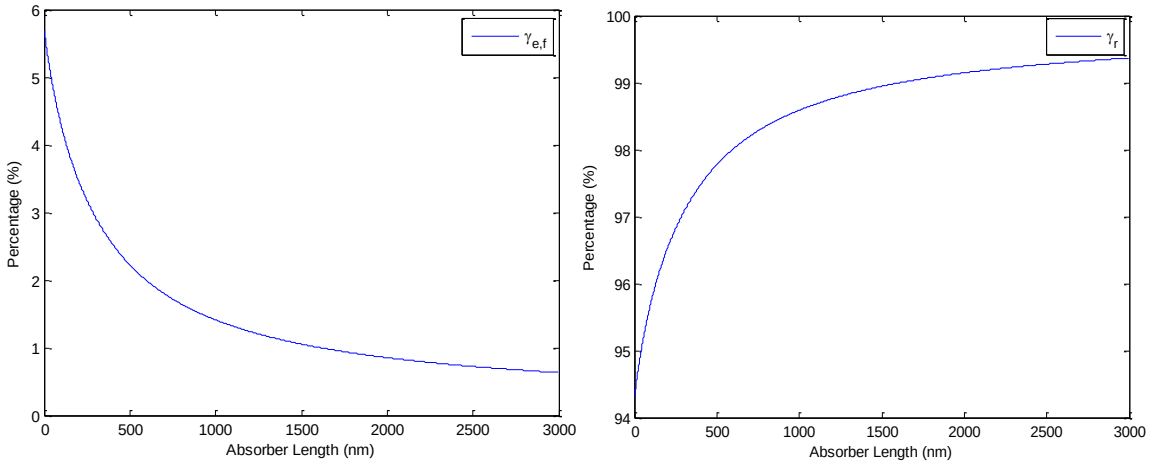

Fig. 5.10. Photon Extraction (Left) and Recycling (Right) Factor vs. Middle CdTe Layer Thickness for Structure B.

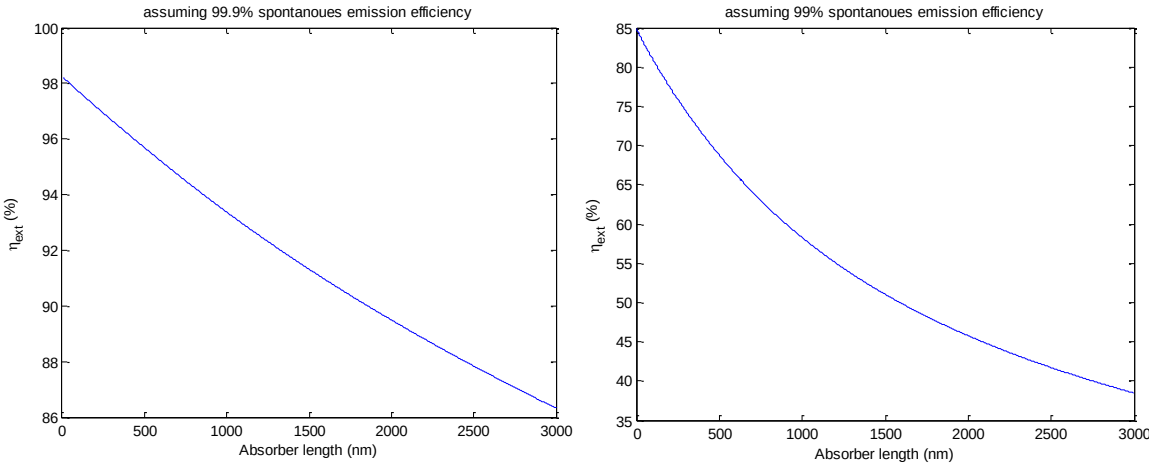

Fig. 5.11. External Luminescence Quantum Efficiency vs. CdTe Middle Layer Thickness of Structure B. Left Assumes the Spontaneous Emission Efficiency is 99.9%, While Right Assumes That It Is 99%.

Compared with structure B, structure C added a Lambertian textured surface to the top of the CdTe/$Mg_xCd_{1-x}Te$ DH. The Lambertian textured surface reflects any incident light with a Lambertian distribution (cosine law), and it helps to randomize the direction of

luminescence photons inside CdTe. It could improve the extraction of light from the front surface, since randomized light can escape more easily from the top surface (compared with light trying to escape a flat top surface, which is restricted by total internal reflection). The $\gamma_{e,f}$ is greatly enhanced compared with structure B as shown in Fig. 5.12. The η_{ext} is plotted in Fig. 5.13, and it decreases with a thicker CdTe layer, due to non-radiative recombination. Compared with structure B, there is some improvement for η_{ext}.

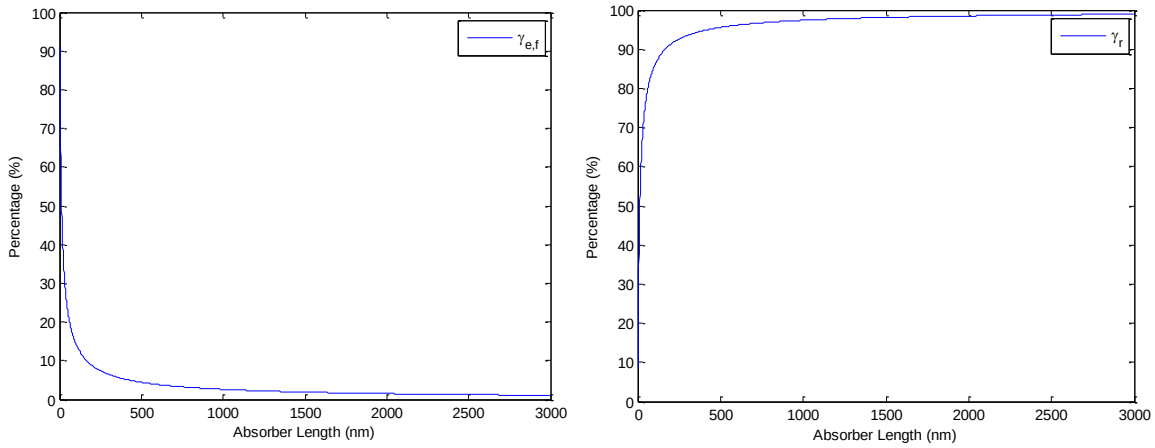

Fig. 5.12. Photon Extraction (Left) and Recycling (Right) Factor vs. Middle CdTe Layer Thickness for Structure C.

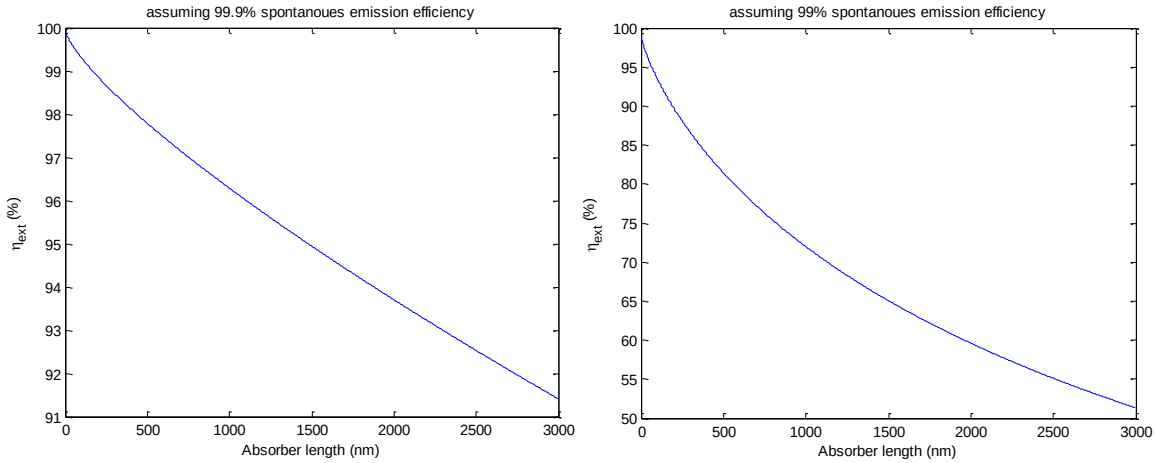

Fig. 5.13. External Luminescence Quantum Efficiency vs. CdTe Middle Layer Thickness of Structure C. Left Assumes the Spontaneous Emission Efficiency Is 99.9%, While Right Assumes That It Is 99%.

Structures D-H utilize a refractive index matching dome with an ideal anti-reflection coating on the surface. Thus, luminescence light reaching the top surface of the sample can directly escape the dome without any loss.

For structure D, a CdTe/$Mg_xCd_{1-x}Te$ DH is directly attached to the dome. Its $\gamma_{e,f}$ and γ_r are plotted in Fig. 5.14. When the CdTe layer is very thin, the $\gamma_{e,f}$ is close to 50%, since half of the luminescence directly escapes through the dome. The η_{ext} is around 50% when the sample quality is high as shown in Fig. 5.15, since the photons will either be absorbed in the substrate or escape through the top surface. η_{ext} is also not very sensitive to the sample thickness, since multiple reflection events are not significant.

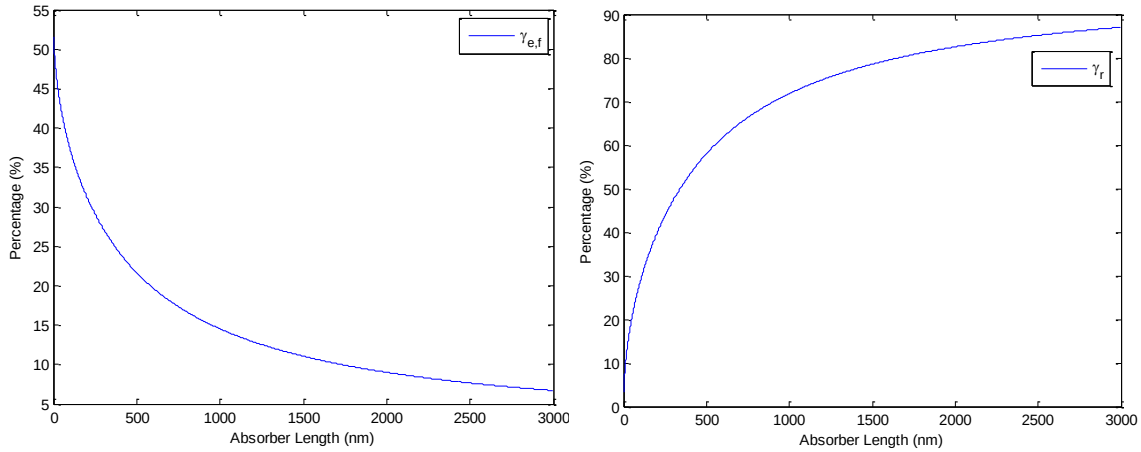

Fig. 5.14. Photon Extraction (Left) and Recycling (Right) Factor vs. Middle CdTe Layer Thickness for Structure D.

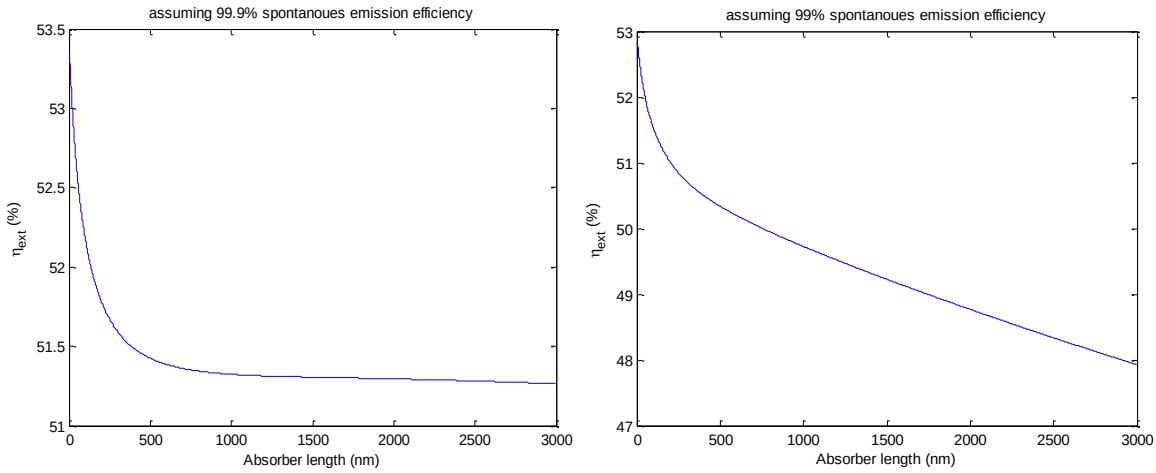

Fig. 5.15. External Luminescence Quantum Efficiency vs. CdTe Middle Layer Thickness of Structure D. Left Assumes the Spontaneous Emission Efficiency is 99.9%, While Right Assumes That It Is 99%.

Compared with structure D, structure E added a perfect back reflector to the CdTe/ $Mg_xCd_{1-x}Te$ DH. The $\gamma_{e,f}$ is almost 100% when the CdTe middle layer is very thin as shown

in Fig 5.16. The η_{ext} is also very high (>98.5%) when the spontaneous emission efficiency is high (99.9%) as shown in Fig. 5.17.

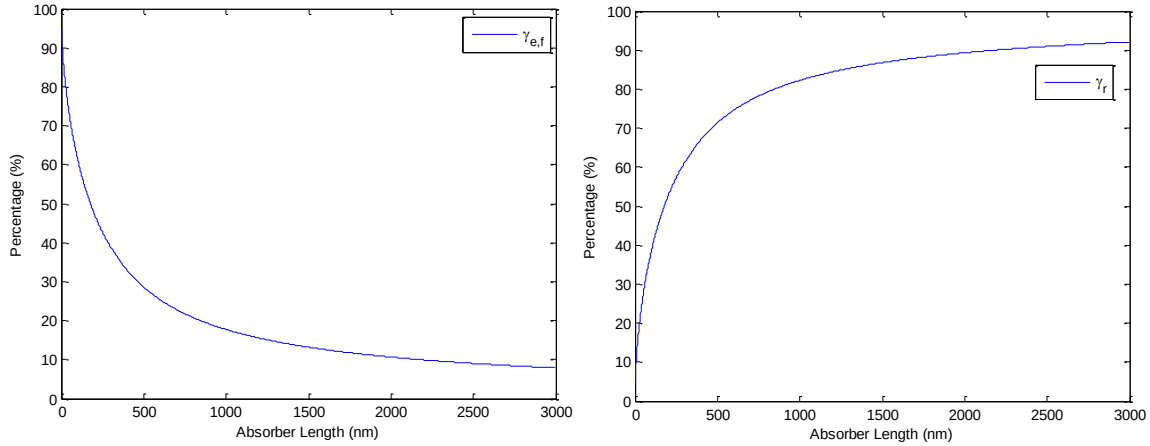

Fig. 5.16. Photon Extraction (Left) and Recycling (Right) Factor vs. Middle CdTe Layer Thickness for Structure E.

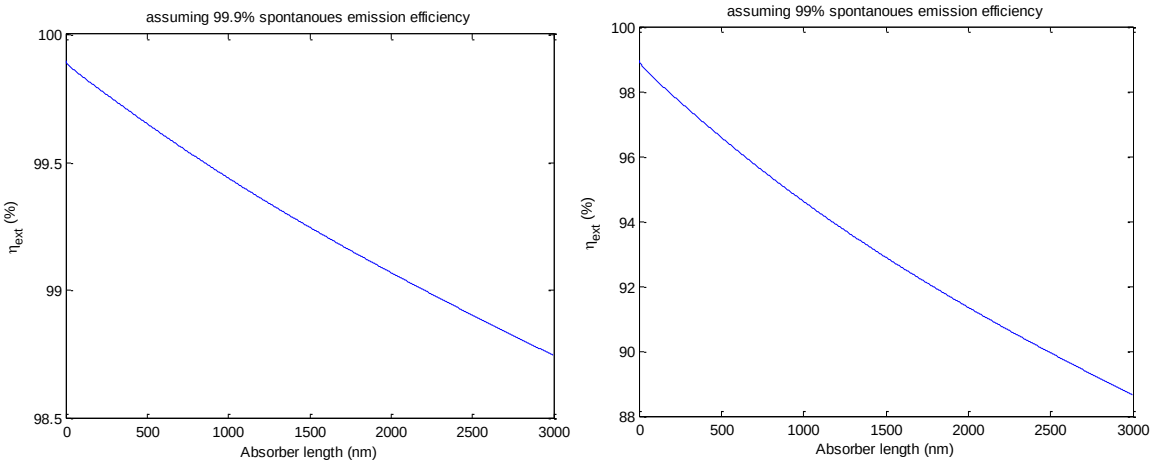

Fig. 5.17. External Luminescence Quantum Efficiency vs. CdTe Middle Layer Thickness of Structure E. Left Assumes the Spontaneous Emission Efficiency Is 99.9%, While Right Assumes That It Is 99%.

Assuming that the CdTe/$Mg_xCd_{1-x}Te$ DH can be lifted off the CdTe buffer, structure F can be made by attaching the DH to a dome. The advantage of lifting off the active region is that light can also be extracted from the back surface of the DH. Fig. 5.18 shows the front and back surface extraction factor ($\gamma_{e,f}$ and $\gamma_{e,b}$) as a function of the CdTe middle layer thickness, and it shows that still most of the light will escape from the front surface rather than the back surface, because of the total internal reflection beyond the critical angle. Its other optical properties, as shown in Fig. 5.19 and Fig. 5.20, are thus almost identical to having a 100% back reflector.

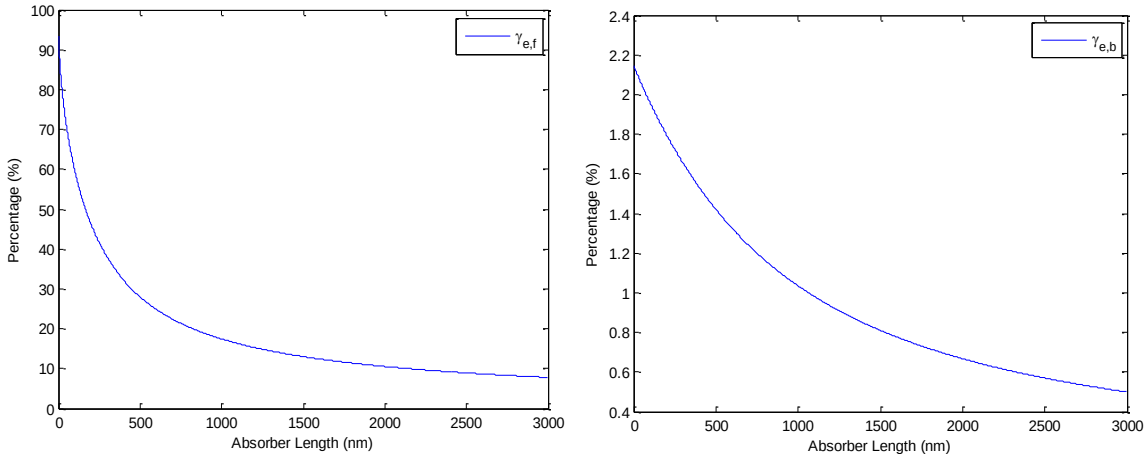

Fig. 5.18. Front(Left) and Back(Right) Surface Photon Extraction Factor vs. Middle CdTe Layer Thickness for Structure F.

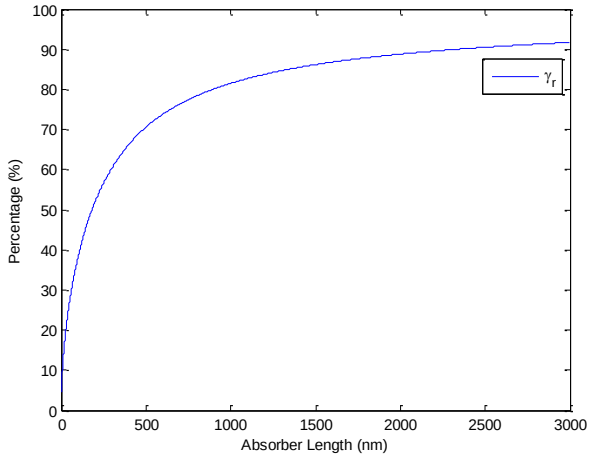

Fig. 5.19. Photon Recycling Factor vs. Middle CdTe Layer Thickness for Structure F.

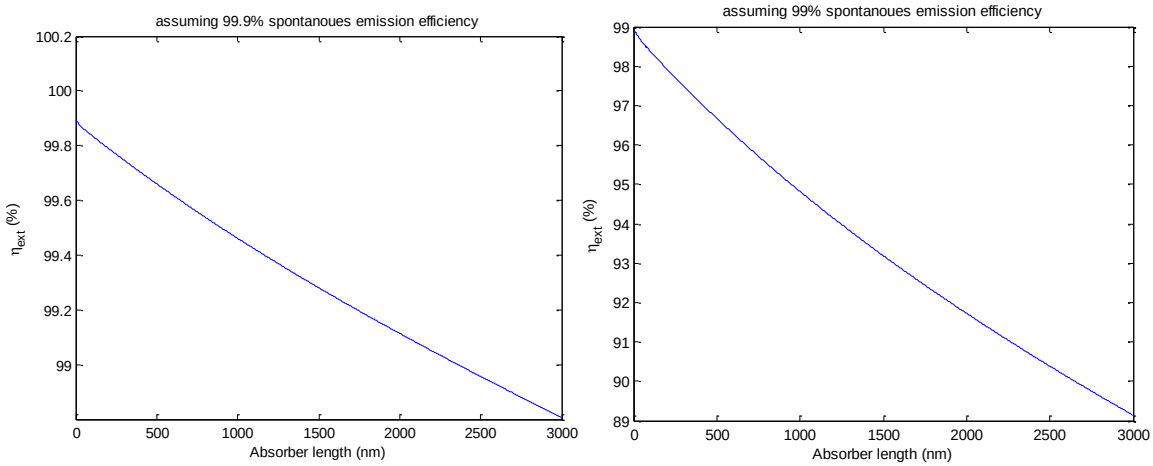

Fig. 5.20. External Luminescence Quantum Efficiency vs. CdTe Middle Layer Thickness of Structure F. Left Assumes the Spontaneous Emission Efficiency Is 99.9%, While Right Assumes That It Is 99%.

Structure G has a textured back surface compared with structure F. The photon extraction factor at the back surface is slightly enhanced as shown in Fig. 5.21. The photon recycling factor as shown in Fig. 5.22 is similar to structure F and η_{ext} is plotted in Fig. 5.23.

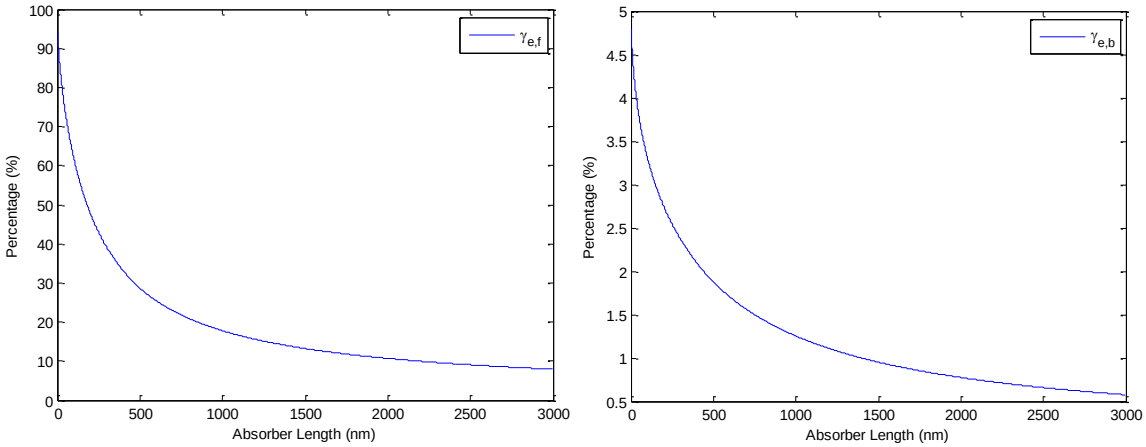

Fig. 5.21. Front(Left) and Back(Right) Surface Photon Extraction Factor vs. Middle CdTe Layer Thickness for Structure G.

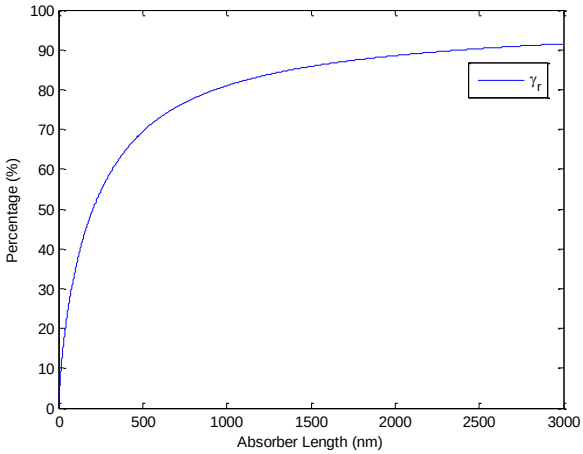

Fig. 5.22. Photon Recycling Factor vs. Middle CdTe Layer Thickness for Structure G.

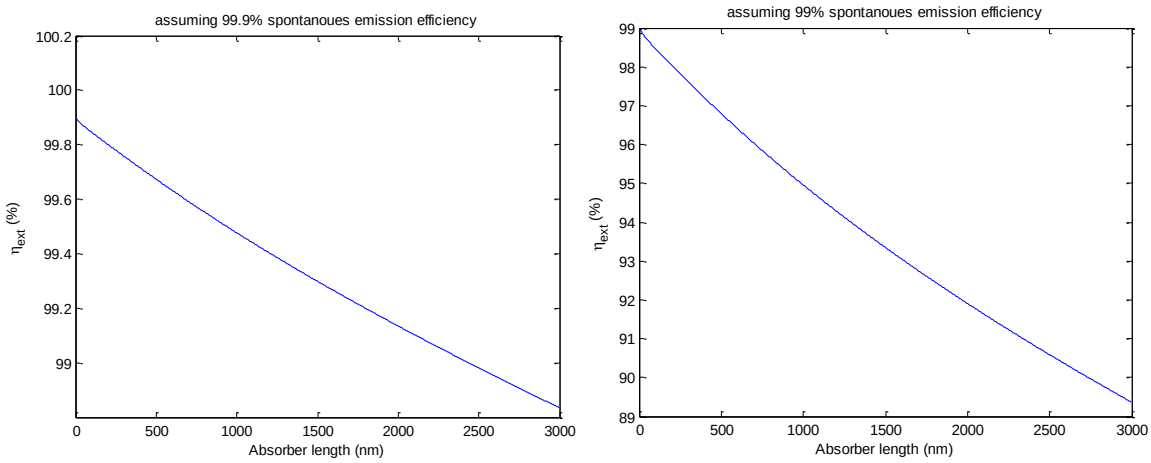

Fig. 5.23. External Luminescence Quantum Efficiency vs. CdTe Middle Layer Thickness of Structure G. Left Assumes the Spontaneous Emission Efficiency is 99.9%, While Right Assumes That It Is 99%.

Finally, structure H shows an ideal case, when both the top and bottom surface of the CdTe/$Mg_xCd_{1-x}Te$ DH are attached to a dome. Fig. 5.24 and 5.25 show the photon extraction and recycling factor (the front and back surface extraction factors are the same), and the η_{ext}. In this case, η_{ext} is the highest.

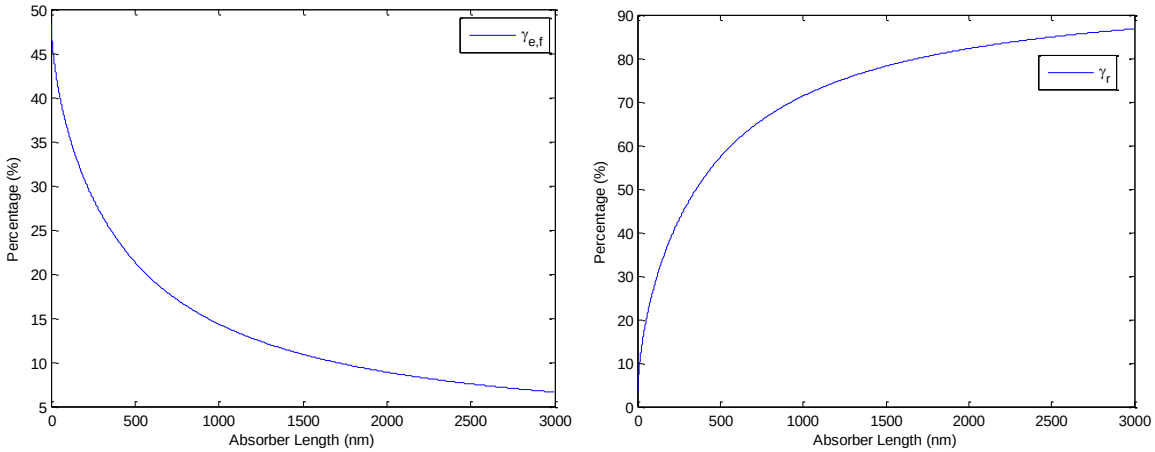

Fig. 5.24. Photon Extraction (Left) and Recycling (Right) Factor vs. Middle CdTe Layer Thickness for Structure H.

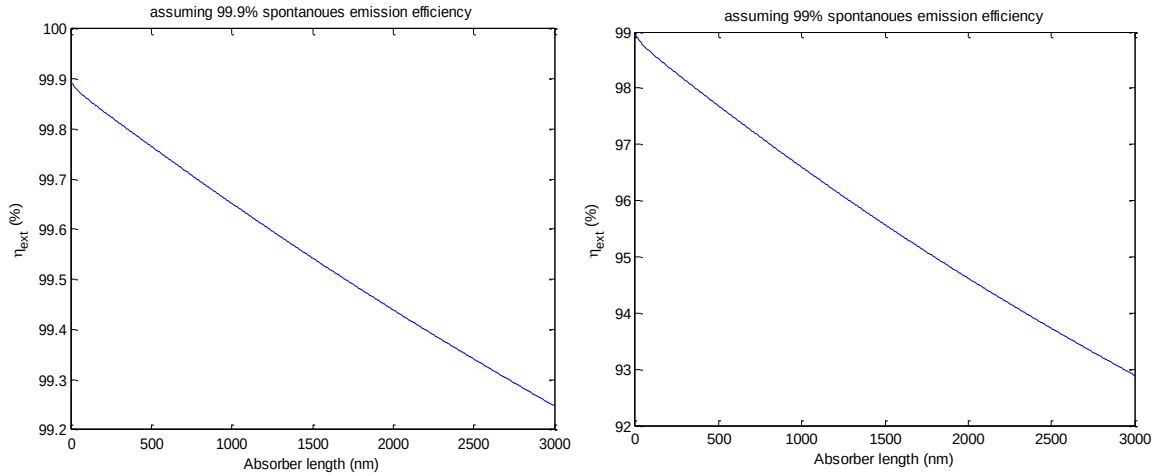

Fig. 5.25. External Luminescence Quantum Efficiency vs. CdTe Middle Layer Thickness of Structure H. Left Assumes the Spontaneous Emission Efficiency Is 99.9%, While Right Assumes That It Is 99%.

5.5 Future Work

It is experimentally demonstrated that the hero CdTe/$Mg_{0.46}Cd_{0.54}Te$ DH has very high spontaneous emission efficiency which is close to 100% at injection levels of 10^{16} cm^{-3}. Theoretically it is calculated to be 99.7% at $\Delta n=1\times10^{17}$ cm^{-3}. Different optical designs are evaluated for the maximum photon extractions. For example, structures similar to that in Ref. [76], could greatly enhance the photon extraction factor and thus external luminescence quantum efficiency. Experimentally, the epitaxial lift-off process is the most important step that needs to be developed to obtain a cooling effect. If this can be realized, high external luminescence quantum efficiency is expected from the CdTe/$Mg_{0.46}Cd_{0.54}Te$ DHs.

Chapter 6

$MG_XCD_{1-X}TE$ (1.7 EV) FOR TANDEM SOLAR CELLS

6.1 Introduction

Crystalline silicon is the most successfully commercialized photovoltaic technologies taking up 90% of the market share [77]. The record efficiency of 25.6% is approaching its practical efficiency limit [78, 79], and further efficiency improvement is more and more challenging. Achieving higher efficiencies is critical to lowering down the cost of electricity generated by photovoltaic (PV) systems, because cell encapsulation cost and balance of system (BOS) cost are the largest cost contributors [77] and these costs are proportional to the area of solar cell modules.

Dual-junction 1.1eV/1.7eV tandem cell has a theoretical limiting efficiency of 45% under one-sun AM1.5G spectrum [80, 81]. Combining an efficient 1.7 eV bandgap top solar cell with silicon cell may further improve the cost-effectiveness of solar panels. However, only a handful of wide-bandgap PV absorbers have demonstrated a high enough efficiency to provide efficiency gain in tandem-configuration, among them are GaInP [82] and lead halide perovskites [83, 84].

Thin-film poly-CdTe is the second most successful PV technology with a record efficiency of 22.1% [2] and the open-circuit voltage of record-efficient poly-CdTe cell is only 0.5 V below the absorber bandgap [85]. Monocrystalline CdTe/MgCdTe double heterostructures (DH) have demonstrated impressively long 3.6 μs carrier lifetimes and ~1 cm/s interface recombination velocities, achieving an open-circuit voltage (V_{oc}) of near 1.1 V [19]. Incorporating Mg into CdTe increases the bandgap and $Mg_{0.13}Cd_{0.87}Te$ alloy has a bandgap of 1.7 eV, if assuming that MgTe has a bandgap of 3.0 eV [86].

In this chapter, a high quality MBE grown monocrystalline 1.7 eV bandgap $Mg_{0.13}Cd_{0.87}Te$ absorbers, and 11.2% efficient solar cell based on this material are demonstrated. The knowledge and technologies may enable mass producible 1.7 eV bandgap $Mg_{0.13}Cd_{0.87}Te$ top cells.

6.2 Material Growth and Characterization

The $Mg_{0.13}Cd_{0.87}Te/Mg_{0.5}Cd_{0.5}Te$ DHs were grown using MBE on lattice matched InSb (001) substrate. A schematic structure is shown in Fig. 6.1. The detailed growth method and conditions are similar to that reported before [14]. The $Mg_{0.5}Cd_{0.5}Te$ is the barrier layer for the 1.7 eV bandgap $Mg_{0.13}Cd_{0.87}Te$ absorber.

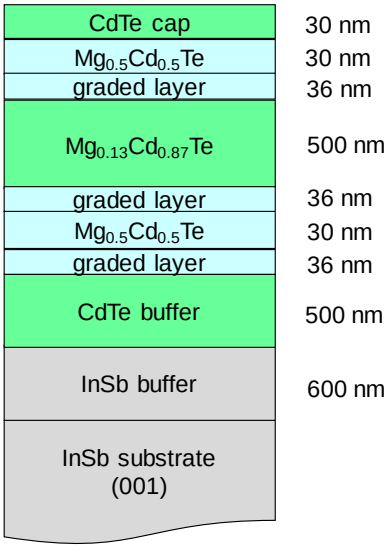

Fig. 6.1. A Schematic Diagram of $Mg_{0.13}Cd_{0.87}Te/Mg_{0.5}Cd_{0.5}Te$ DH Sample.

Photoluminescence (PL) and Time-Resolved Photoluminescence (TRPL) measurements are carried out to evaluate the optical properties of the

$Mg_{0.13}Cd_{0.87}Te/Mg_{0.5}Cd_{0.5}Te$ DH. In Fig. 6.2 (left), the PL spectrum shows that the PL peak wavelength is at 716 nm which corresponds to a bandgap energy of 1.71 eV, considering the 1 *kT* difference between the bandgap energy and PL peak energy. The PL spectrum of a high quality $GaAs/Al_{0.25}Ga_{0.75}As$ DH is also shown for comparison indicating that the PL intensity of $Mg_{0.13}Cd_{0.87}Te/Mg_{0.5}Cd_{0.5}Te$ DH is very high. Fig. 6.2 (right) shows that the sample has a very long carrier lifetime of 0.56 μs. The strong PL intensity and long carrier lifetime indicate that the material quality both for the $Mg_{0.13}Cd_{0.87}Te$ bulk region and at the $Mg_{0.13}Cd_{0.87}Te/Mg_{0.5}Cd_{0.5}Te$ interfaces are very high.

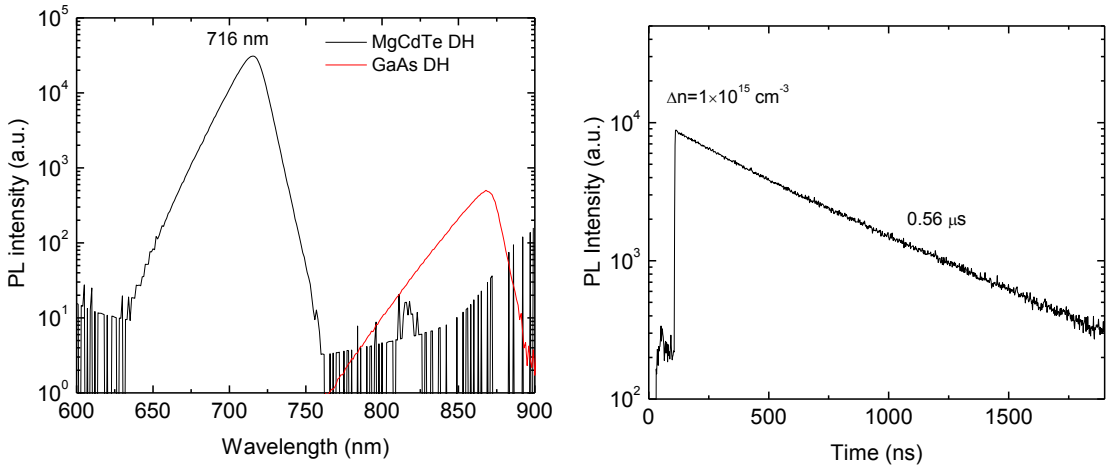

Fig. 6.2. (Left) PL and (Right) TRPL Results of a $Mg_{0.13}Cd_{0.87}Te/Mg_{0.5}Cd_{0.5}Te$ DH Sample.

The front surface external luminescence quantum efficiency ($\eta_{ext,f}$) is measured using the method presented in [30, 31]. This is an important figure of merit to quantify the material quality of a photovoltaic absorber, because $\eta_{ext,f}$ is related to the implied open-circuit voltage $V_{i,oc}$ of a solar cell through the formula [28, 29]:

$$V_{i,oc} = V_{DB} - \frac{kT}{q}\left|\ln\left(\eta_{ext,f}\right)\right| \tag{6.1}$$

where V_{DB} is the detailed-balance open circuit voltage, and it is calculated to be 1.4 V for the DH shown above. $\eta_{ext,f}$ as a function of excitation current density(J_{sc}) is shown in Fig. 6.3. $\eta_{ext,f}$ is 1.2% under one-sun condition, i.e. a carrier injection current density of ~20 mA/cm^2. The implied open-circuit voltage is 1.3 V according to (6.1).

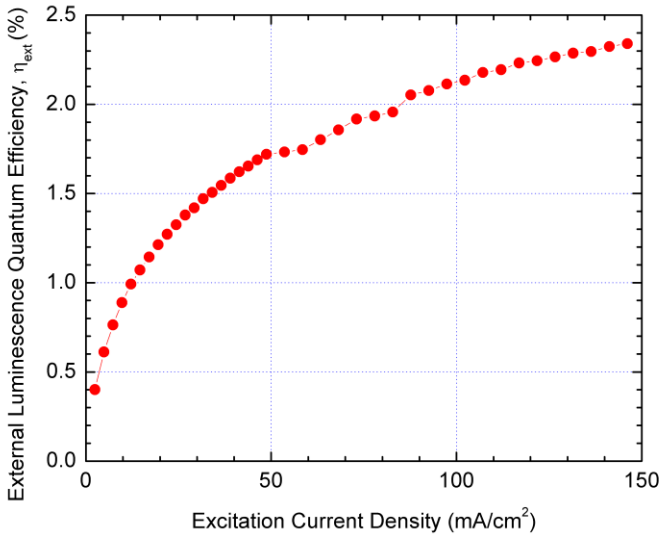

Fig. 6.3. Front Surface External Luminescence Quantum Efficiency ($\eta_{ext,f}$) as a Function of Excitation Current Density.

6.3 $Mg_xCd_{1-x}Te$ (1.7 eV) Solar Cell

The solar cell design principles are similar to CdTe/$Mg_xCd_{1-x}Te$ DH solar cells as discussed in the previous chapter. The cell structure, shown in Fig. 6.4 (left), consists of a MBE grown $Mg_{0.13}Cd_{0.87}Te$/ $Mg_{0.5}Cd_{0.5}Te$ DH on an InSb substrate, a PECVD (Plasma-enhanced chemical vapor deposition) deposited p-type hydrogenated amorphous silicon (a-Si:H) contact layer, and an Indium Tin Oxide (ITO) top electrode. The doping

concentrations are in the unit of cm^{-3}, and the n-type dopant is indium for CdTe and p-type dopant is boron for a-Si:H. Indium dopant may diffuse from the CdTe buffer to the $Mg_{0.5}Cd_{0.5}Te$ bottom barrier layer, facilitating the electron transport. The $Mg_{0.13}Cd_{0.87}Te$ active region were undoped, because it was found that undoped sample has the strongest PL intensity. Shown in Fig. 6.4 (right), is the equilibrium state band edge alignment. The conduction and valance band offset ratio between CdTe and MgTe is assumed to be 70:30 [23]. The p-type a-Si:H layer on top of the DH induces band-bending in the $Mg_{0.13}Cd_{0.87}Te$ absorber. The small valance band offset at the front $Mg_{0.13}Cd_{0.87}Te/Mg_{0.5}Cd_{0.5}Te$ interface allows holes to be selectively extracted out of the $Mg_{0.13}Cd_{0.87}Te$ absorber region during the operation of the solar cell, while the large conduction band offset prevent electrons from going to the p-type contact region.

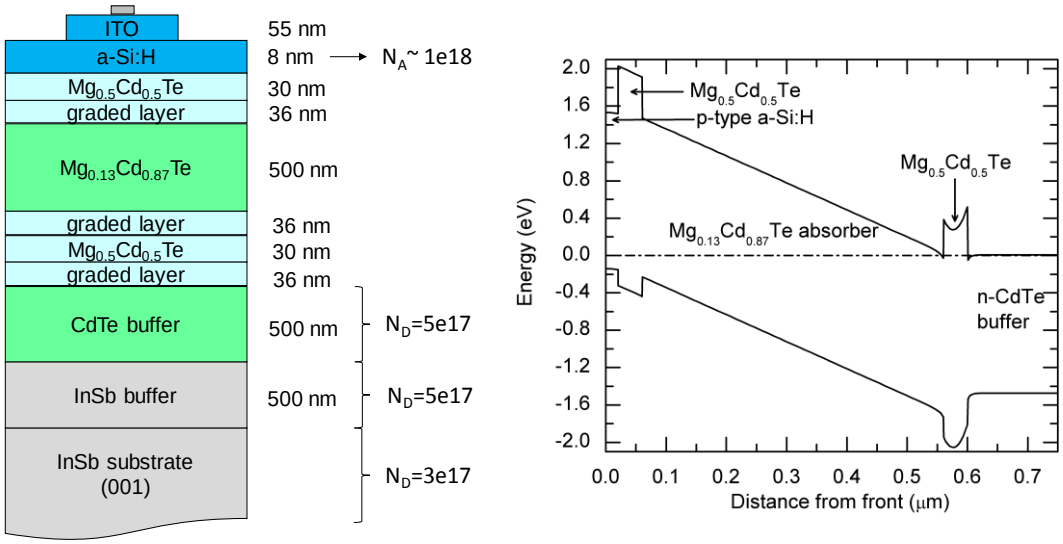

Fig. 6.4. Solar Cell Device Structure (Left) and Band Diagram at Equilibrium (Right).

The p-type a-Si:H covers the entire sample, while the 55-nm-thick ITO are deposited in small patches on top of the a-Si:H layer. The conductivity of the p-type a-Si:H is low, thus the cell area is defined by the conductive ITO, which has a sheet resistance of 100 Ω/sq. The ITO layer also plays the roles of anti-reflection coating. During the light-JV and External Quantum Efficiency (EQE) measurements, the wafers are mounted onto a gold coated Si substrate and the measurements are done by probing silver metal contacts on top of the ITO patches and the gold Si substrate. The results are shown in Fig. 6.5. J_{sc} could not be accurately determined from light-JV measurement, since the cell areas are not very well defined by the ITO patches (carriers generated from around the cells can contribute to the total current). Thus J_{sc} is calculated by integrating the EQE curve with the AM1.5G spectrum and it is determined to be 15.0 mA/cm^2 for the solar cell measured. The directly measured JV curve is scaled to match the 15.0 mA/cm^2 J_{sc}. 11.2% is the active area efficiency and considering the ~10% metal coverage, the total area efficiency is 10.1%.

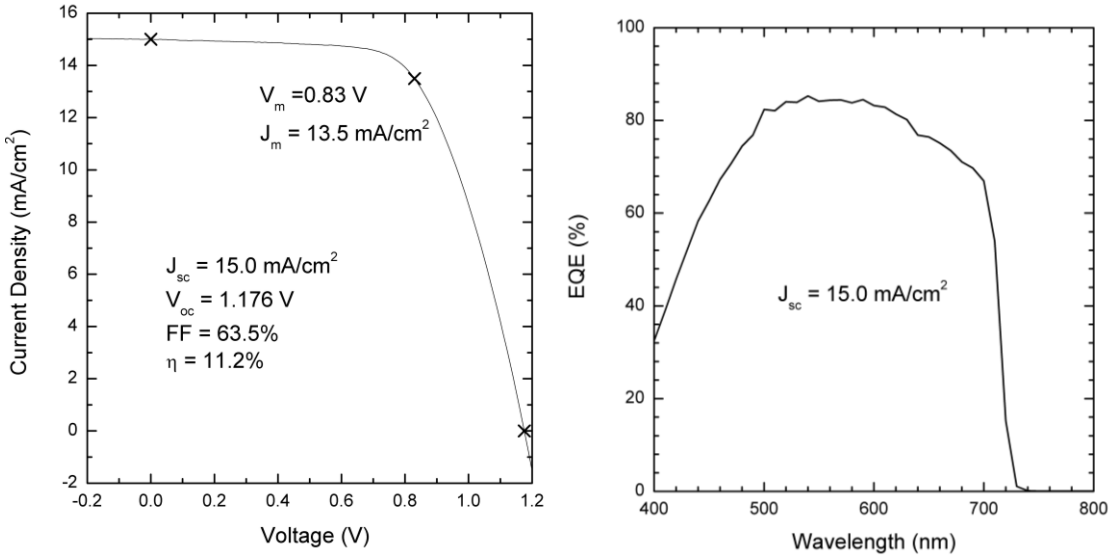

Fig. 6.5. Device Performance of the Most Efficient Cell with Area of 5 mm by 5 mm. (Left) Light-JV Curve under AM1.5G 0.1 W/cm^2 Spectrum Measured In-house. (Right) External Quantum Efficiency.

The V_{oc} of 1.176 V is much lower than the calculated implied V_{oc} (1.3 V), which means that the device did not efficiently convert the quasi-Fermi level separation into output voltage. Simulations (will be described later in details) show that it is very possible that the bottom barrier layer ($Mg_{0.5}Cd_{0.5}Te$) has a potential that is too high for the transport of majority carriers (electrons). As shown in Fig. 6.6, at open circuit condition, both electrons and holes will diffuse to the bottom CdTe/InSb interface to recombine (the total current is zero). The charge transport is determined by the charge density, mobility and the gradient of quasi-Fermi level ($J_e = n\mu_e E_n'$). Since the bottom barrier is too high for electrons (n is very small), there is an electron Fermi level drop at the bottom $Mg_{0.5}Cd_{0.5}Te$ barrier to facilitate the transport of electrons. Thus V_{oc} is lower than the implied V_{oc}. The low Fill Factor (FF) of 63.5%, also implies the poor charge transport in this solar cell structure.

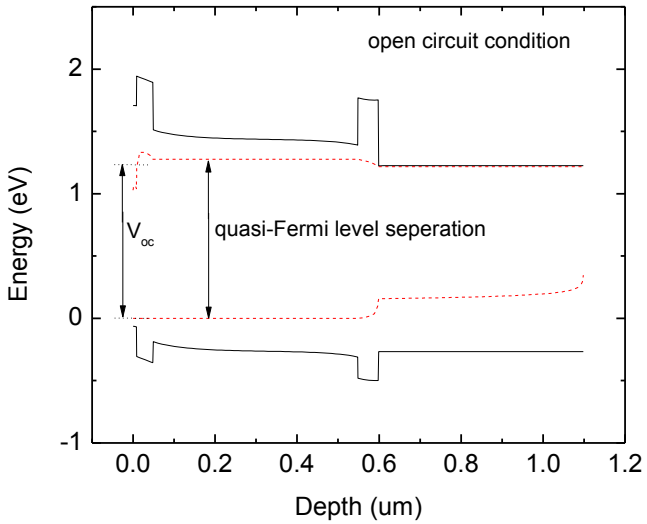

Fig. 6.6. Band Diagram at Open Circuit Condition for The Solar Cells in Fig. 6.4.

To further evaluate the loss of V_{oc} and FF, the following simulations have been performed using PC1D. The baseline solar cell is based on the one shown in Fig. 6.4 with 1 cm^2 surface area. The band offsets of the top and bottom barriers (relative to the 1.7 eV $Mg_{0.13}Cd_{0.87}Te$ absorber) are varied, in order to distinguish how the conduction (ΔE_c) and valance band offsets (ΔE_v) affect the cell performance.

As shown in Fig. 6.7, the top barrier's ΔE_v is set to 0 eV for effective hole transport, while the ΔE_c is varied from 0.1 eV to 0.5 eV. The most significant change is the V_{oc}, as also shown in Table 6.1, and it increases as ΔE_c increases. That's because higher conduction band offset can effectively prevent electrons from recombining with holes at the p-n junction region. V_{oc} saturates as ΔE_c increases beyond 0.3 eV, which means that 0.3 eV band offset is sufficient for the confinement of electrons. FF also increases slightly with ΔE_c due to less recombination.

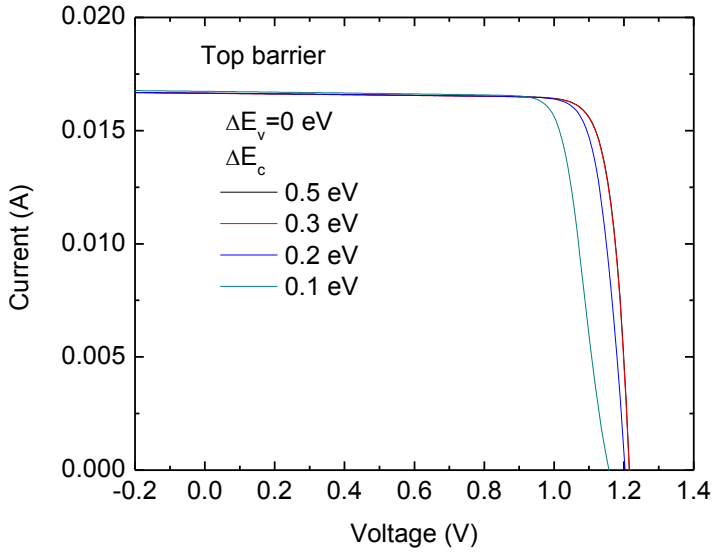

Fig. 6.7. Simulated I-V Curve of $Mg_{0.13}Cd_{0.87}Te$ (1.7 eV) Solar Cells, with ΔE_v=0 eV and ΔE_c Varied for The Top Barrier.

Table 6.1. The Device Parameters of $Mg_{0.13}Cd_{0.87}Te$ (1.7 eV) Solar Cells Shown in Fig. 6.7.

ΔE_c (eV)	**0.1**	**0.2**	**0.3**	**0.5**
J_{sc} (mA)	16.7	16.7	16.6	16.7
V_{oc} (V)	1.157	1.204	1.215	1.216
P_{max} (mW)	15.8	16.9	17.2	17.2
FF	0.82	0.84	0.85	0.85

In Fig. 6.8, ΔE_c is set to 0.3 eV for the top barrier layer (sufficient electron confinement), while ΔE_v is varied from 0 eV to 0.5 eV. As ΔE_v increases, FF decreases and the curve eventually becomes S-shaped at 0.5 eV, which is due to the poor transport of holes. Table 6.2. shows that as long as the ΔE_v is smaller than 0.3 eV, the hole transport and thus FF, is not affected.

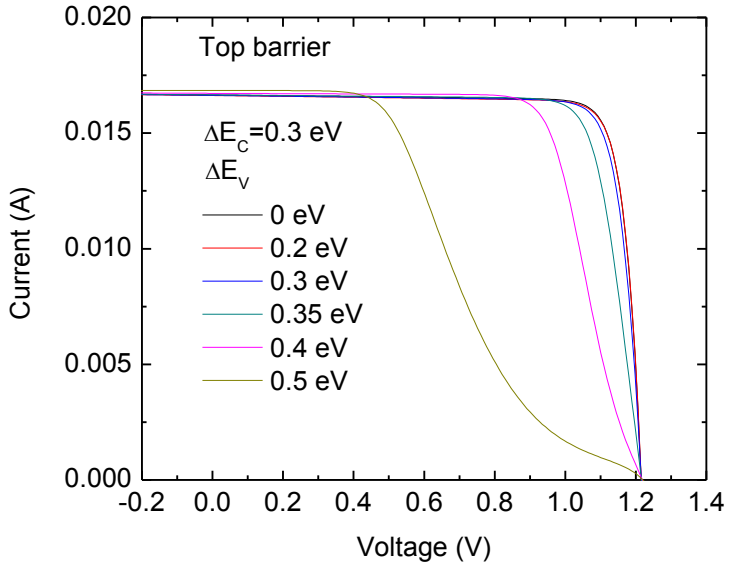

Fig. 6.8. Simulated I-V Curve of $Mg_{0.13}Cd_{0.87}Te$ (1.7 eV) Solar Cells, with ΔE_c=0.3 eV and ΔE_v Varied for The Top Barrier.

Table 6.2. The Device Parameters of $Mg_{0.13}Cd_{0.87}Te$ (1.7 eV) Solar Cells Shown in Fig. 6.8.

ΔE_v (eV)	**0**	**0.2**	**0.3**	**0.35**	**0.4**	**0.5**
J_{sc} (mA)	16.6	16.6	16.6	16.7	16.7	16.8
V_{oc} (V)	1.215	1.216	1.216	1.216	1.219	1.220
P_{max} (mW)	17.2	17.2	17.0	16.3	14.7	7.9
FF	0.85	0.85	0.84	0.80	0.72	0.39

In Fig. 6.9, ΔE_c is set to 0 eV for the bottom barrier layer (for ideal electron transport), while ΔE_v is varied from 0.1 eV to 0.4 eV. The open circuit voltage increases as the minority carrier (hole) confinement becomes better and 0.3 eV is high enough for sufficient hole confinement (parameters shown in Table 6.3).

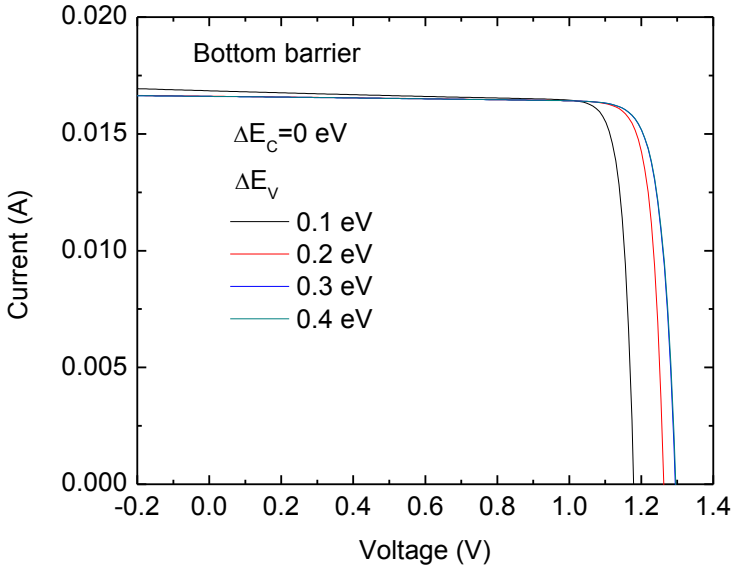

Fig. 6.9. Simulated I-V Curve of $Mg_{0.13}Cd_{0.87}Te$ (1.7 eV) Solar Cells, with ΔE_c=0 eV and ΔE_v Varied for The Bottom Barrier.

Table 6.3. The Device Parameters of $Mg_{0.13}Cd_{0.87}Te$ (1.7 eV) Solar Cells Shown in Fig. 6.9.

ΔE_v **(eV)**	0.1	0.2	0.3	0.4
J_{sc} (mA)	16.8	16.6	16.6	16.6
V_{oc} (V)	1.179	1.262	1.295	1.296
P_{max} (mW)	17.3	18.3	18.6	18.6
FF	0.87	0.87	0.87	0.86

In Fig. 6.10, ΔE_v is set to 0.2 eV for the bottom barrier layer, while ΔE_c is varied from 0 eV to 0.5 eV. In this case both FF and V_{oc} become smaller with higher ΔE_c. The decrease of FF is due to worse majority carrier (electron) transport and the decrease of V_{oc} is due to the electron Fermi level drop across the bottom barrier (already seen in Fig 6.6). The reason is explained as follows: Since ΔE_v is not ideal for hole confinement, at open circuit condition, photo-generated holes will leak to the bottom CdTe buffer layer and recombine

at the CdTe/InSb interface. For net current to be zero, electrons will also diffuse over the bottom barrier layer. With ΔE_c too high (over 0.3 eV), there will be an electron Fermi level drop to facilitate the transport of electrons and thus the output voltage is lowered.

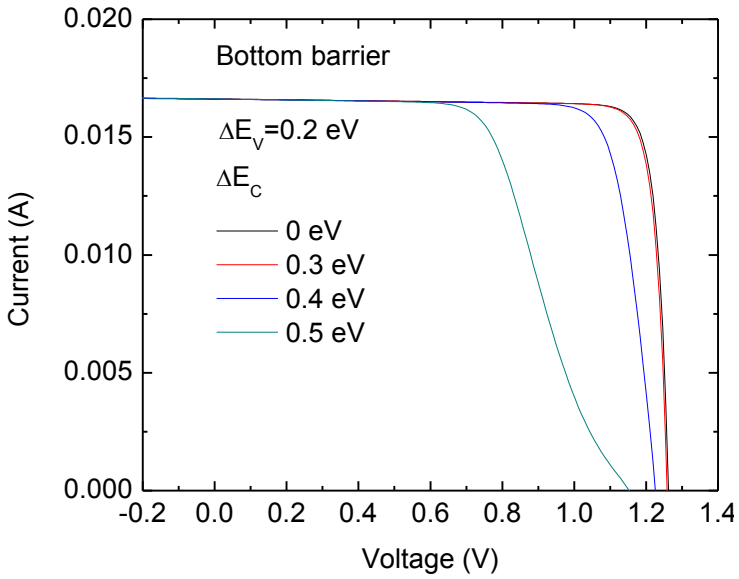

Fig. 6.10. Simulated I-V Curve of $Mg_{0.13}Cd_{0.87}Te$ (1.7 eV) Solar Cells, with ΔE_v=0.2 eV and ΔE_c Varied for The Bottom Barrier.

Table 6.4. The Device Parameters of $Mg_{0.13}Cd_{0.87}Te$ (1.7 eV) Solar Cells Shown in Fig. 6.10.

ΔE_c (eV)	0.0	0.3	0.4	0.5
J_{sc} (mA)	16.6	16.6	16.6	16.6
V_{oc} (V)	1.262	1.258	1.226	1.152
P_{max} (mW)	18.3	18.2	16.6	11.7
FF	0.87	0.87	0.82	0.61

To summarize the above simulations, 0.3 eV is a critical value for both carrier transport and confinement. For carrier transport, ideally the band offset should be lower than 0.3 eV,

while for carrier confinement, the band offset should be larger than 0.3 eV. For the solar cell structure in Fig 6.4, ΔE_c = 0.385 eV and ΔE_v = 0.165 eV at the $Mg_{0.13}Cd_{0.87}Te/Mg_{0.5}Cd_{0.5}Te$ interfaces and thus the lower than predicted V_{oc} and FF is most probably due the high conduction band offset of the bottom barrier. It is thus reasonable to slightly reduce the Mg composition (ideally to 35%) in the bottom barrier for future device designs.

To analyze the loss mechanisms of photocurrent, the reflectance and absorptance spectrum of each layer is calculated using wave-optics, as shown in Fig. 6.11. The absorptance of the $Mg_{0.13}Cd_{0.87}Te$ absorber layer resembles the measured EQE closely, indicating that the carrier collection efficiency in the solar cell is close to unity, which is expected since the minority carrier lifetime in $Mg_{0.13}Cd_{0.87}Te/Mg_{0.5}Cd_{0.5}Te$ DH is measured to be very long, indicating a long diffusion length. Integrating the absorptance of the CdTe absorber with the AM1.5 spectrum gives a J_{sc} of 15.3 mA/cm^2. The losses of photocurrent due to reflectance and parasitic absorptions are also shown in Fig. 6.11. J_{sc} can be further improved by employing double-layer antireflection coatings, wider-bandgap hole contact layers and a thicker $Mg_{0.13}Cd_{0.87}Te$ absorber.

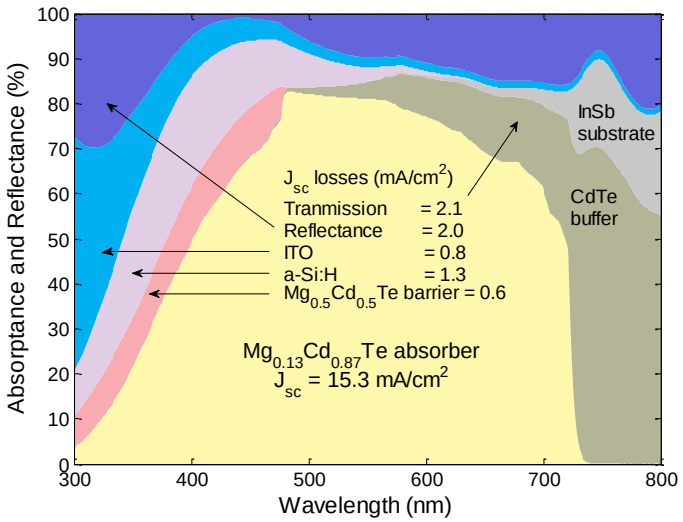

Fig. 6.11. Calculated Reflectance, Transmittance and Absorptance Spectra of $Mg_{0.13}Cd_{0.87}Te/Mg_{0.5}Cd_{0.5}Te$ Double-Heterostructure Solar Cell.

6.4 Conclusions

1.7 eV $Mg_{0.13}Cd_{0.87}Te$ solar cells have been fabricated with 11.2% efficiency and V_{oc} of 1.176 V. The materials studies have shown that the $Mg_{0.13}Cd_{0.87}Te/Mg_{0.5}Cd_{0.5}Te$ DH has very strong PL intensity and long minority carrier lifetime of 0.56 μs and calculation shows an implied V_{oc} of 1.3 eV is possible based on this material. However our fabricated devices shows a V_{oc} much lower than this value and the FF is also low (only 63.5%). It is possible to further increase V_{oc} and FF by optimizing carrier transport. The J_{sc} can be further improved by minimizing the reflection and parasitic absorptions and by increasing the absorber layer thickness. To have an efficiency gain in a tandem configuration with Si solar cell (even with 25.6% efficiency), the 1.7 eV $Mg_{0.13}Cd_{0.87}Te$ solar cell efficiency should be as least 13%.

REFERENCES

[1] A. Luque and S. Hegedus, Chapter 14, Handbook of Photovoltaic Science and Engineering, John Wiley & Sons, 2003.

[2] First Solar Press Release, published in February, 2016. investor.firstsolar.com/releasedetail.cfm?releaseid=956479.

[3] A. P. Kirk, M. J. DiNezza, S. Liu, X.-H. Zhao, and Y.-H. Zhang, the Proceeding of the 39th IEEE Photovoltaic Specialists Conference, 2515 (2013).

[4] J. J. Loferski, J. Appl. Phys. **27**, 777 (1956).

[5] T. Nakazawa, K. Takamizawa, and K. Ito, App. Phys. Lett. **50**, 279 (1987).

[6] J. Britt and C. Ferekides, Appl. Phys. Lett. **62**, 2851 (1993).

[7] X. Wu, J. C. Keane, R. G. Dhere, C. DeHart, D. S. Albin, A. Duda, T. A. Gessert, S. Asher, D. H. Levi, and P. Sheldon, the Proceeding of 17th European PVSEC, 995 (2001).

[8] X. Wu, Sol. Energy **77**, 803 (2004).

[9] Research cell efficiency record by NREL. www.nrel.gov/ncpv/images/efficiency_chart.jpg.

[10] M. Gloeckler, I. Sankin, and Z. Zhao, IEEE J. Photovoltaics **3**, 1389 (2013).

[11] M. A. Green, K. Emery, Y. Hishikawa, W. Warta, E. D. Dunlop, Prog. Photovolt: Res. Appl. **22**, 701 (2014).

[12] M. A. Green, K. Emery, Y. Hishikawa, W. Warta, E. D. Dunlop, Prog. Photovolt: Res. Appl. **23**,1 (2015).

[13] J. Sites, J. Pan, Thin Solid Films, **515**, 6099 (2007).

[14] M. J. DiNezza, X.-H. Zhao, S. Liu, A. P. Kirk, and Y.-H. Zhang, Appl. Phys. Lett. **103**, 193901 (2013).

[15] X.-H. Zhao, M. J. DiNezza, S. Liu, C. M. Campbell, Y. Zhao, and Y.-H. Zhang, Appl. Phys. Lett. **105**, 252101 (2014).

[16] S. Liu, X.-H. Zhao, C. M. Campbell, M. B. Lassise, Y. Zhao, and Y.-H. Zhang, Appl. Phys. Lett. **107**, 041120 (2015).

[17] X.-H. Zhao, S. Liu, C. M. Campbell, Y. Zhao, M. B. Lassise, and Y.-H. Zhang, the Proceeding of the 43rd IEEE Photovoltaic Specialists Conference, 2016.

[18] X.-H. Zhao, S. Liu, Y. Zhao, C. M. Campbell, M. B. Lassise, Y.-S. Kuo, and Y.-H. Zhang, IEEE J. Photovoltaics **6**, 552 (2016).

[19] Y. Zhao, M. Boccard, S. Liu, J. Becker, X.-H Zhao, C. M. Campbell, E. Suarez, M. B. Lassise, Z. Holman and Y.-H. Zhang, Nature Energy, art. no. 16067 (2016).

[20] Photovoltaics Report, prepared by Fraunhofer Institute for Solar Energy Systems, 2015.

[21] First Solar Press Release, published in June, 2015. investor.firstsolar.com/releasedetail.cfm?ReleaseID=917926.

[22] The figure is from ASU MBE Optoelectronics group, asumbe.eas.asu.edu/images/research/multijunction/Colorspectrum_Eg_a.jpg

[23] B. KuhnHeinrich, W. Ossau, H. Heinke, F. Fischer, T. Litz, A. Waag, and G. Landwehr, Appl. Phys. Letter. **63**, 2932 (1993).

[24] P. Kidd, XRD of gallium nitride and related compounds: strain, composition and layer thickness, from PANalytical.

[25] Bruker's webnar, High Resolution X-ray Difractometry, May 2011.

[26] X.-H. Zhao, M. J. DiNezza, S. Liu, S. Lin, Y. Zhao, and Y.-H. Zhang, J. Vac. Sci. & Technol. B **32**, 040601 (2014).

[27]X.-H. Zhao, M. J. DiNezza, S. Liu, P. A. R. D. Jayathilaka, O. C. Noriega, T. H. Myers, Y.-H. Zhang, the Proceeding of the 40th IEEE Photovoltaic Specialist Conference, 3272 (2014).

[28] U. Rau, Phys. Rev. B **76**, 085303 (2007).

[29] O. D. Miller, E. Yablonovitch, and S. R. Kurtz, IEEE J. Photovoltaics **2**, 303 (2012).

[30] I. Schnitzer, E. Yablonovitch, C. Caneau, and T. J. Gmitter, Appl. Phys. Lett. **62**, 131 (1993).

[31] Y. Zhao, X.-H. Zhao, Y.-H. Zhang, the proceeding of the 43rd IEEE Photovoltaic Specialists Conference 2016.

[32] W. Becker, The Becher & Hickl TCSPC Handbook, 3rd Edition (2008).

[33] E. F. Schubert, Light-Emitting Diodes, 2nd Edition, Cambridge University Press, 2006.

[34] W. Shockley and W. T. Read, Jr., Phys. Rev. **87**, 835 (1952).

[35] D. K. Schroder, IEEE T. Electron. Dev. **44**, 160 (1997).

[36] J. Nelson, The Physics of Solar Cells, pp. 106, Imperial College Press, 2004.

[37] M. A. Steiner, J. F. Geisz, I. García, D. J. Friedman, A. Duda, and S. R. Kurtz, J. Appl. Phys. **113**, 123109 (2013).

[38] R. K. Ahrenkiel, B. M. Keyes, D. L. Levi, K. Emery, T. L. Chu, and S. S. Chu, Appl. Phys. Lett. **64**, 2879 (1994).

[39] R. Cohen, V. Lyahovitskaya, E. Poles, A. Liu, and Y. Rosenwaks, Appl. Phys. Lett. **73**, 1400 (1998).

[40] S. Adachi, Handbook on Physical Properties of Semiconductors Vol 3: II-VI Compound Semiconductors, Springer US, 2004.

[41] S. Adachi, Optical Constants of Crystalline and Amorhpous Semiconductors: Numerical Data and Graphical Information, Kluwer Academic Publishers, 1999.

[42] R. J. Nelson and R. G. Sobers, Appl. Phys. Lett. **32**, 761 (1978).

[43] L. W. Molenkamp and H. F. J. van't Blik, J. Appl. Phys. **64**, 4253 (1988).

[44] G. B. Lush, M. R. Melloch, M. S. Lundstrom, D. H. Levi, R. K. Ahrenkiel, and H. F. MacMillan, Appl. Phys. Lett. **61**, 2440 (1992).

[45] G. D. Gilliland, D. J. Wolford, T. F. Kuech, J. A. Bradley, and H. P. Hjalmarson, J. Appl. Phys. **73**, 8386 (1993).

[46] J. M. Olson, R. K. Ahrenkiel, D. J. Dunlavy, B. Keyes, and A. E. Kibbler, Appl. Phys. Lett. **55**, 1208 (1989).

[47] R. K. Ahrenkiel, J. M. Olson, D. J. Dunlavy, B. M. Keyes, and A. E. Kibbler, J. Vac. Sci. Technol., A **8**, 3002 (1990).

[48] D. Kuciauskas, A. Kanevce, J. M. Burst, J. N. Duenow, R. Dhere, D. S. Albin, D. H. Levi, and R. K. Ahrenkiel, IEEE J. Photovoltaics **3**, 1319 (2013).

[49] K. W. Mitchell, A. L. Fahrenbruch, and R. H. Bube, J. Appl. Phys. **48**, 4365 (1977).

[50] E. Marin, J. Santoyo, A. Calderon, O. Vigil-Galan, and G. Contreras-Puente, J. Appl. Phys. **107**, 123701 (2010).

[51] D. K. Schroder, Semiconductor Material and Device Characterization, 3rd Edition, pp. 397, John Wiley and Sons, 2006.

[52] F. Bassani, S. Tatarenko, K. Saminadayar, N. Magnea, R. T. Cox, A. Tardot, and C. Grattepain, J. Appl. Phys. **72**, 2927 (1992).

[53] S. R. Johnson, D. Ding, J.-B. Wang, S.-Q. Yu, and Y.-H. Zhang, J. Vac. Sci. & Technol. B, **25**, 1077, (2007).

[54] R. N. Bicknell, N. C. Giles, and J. F. Schetzina, Appl. Phys. Lett. **49**, 1095 (1986).

[55] D. E. Ashenford, J. H. C. Hogg, D. Johnston, B. Lunn, C. G. Scott and D. Staudte, J. Cryst. Growth **101**, 157 (1990).

[56] F. Bassani, S. Tatarenko, K. Saminadayar, J. Bleuse, N. Magnea, and J. L. Pautrat, Appl. Phys. Lett. **58**, 2651 (1991).

[57] G. Karczewski, A.K. Zakrzewski, L. Dobaczewski, W. Dobrowolski, E. Grodzicka, J. Jaroszynski, T. Wojtowicz, J. Kossut, Thin Solid Films **267**, 79 (1995).

[58] D. A. Porter, K. E. Easterling, and M. Y. Sherif, Phase transformations in metals and alloys, 3rd Edition, pp.76, CRC Press, 2009.

[59] R. T. Ross, J. Chem. Phys. **46**, 4590 (1967).

[60] J.-B. Wang, S. R. Johnson, D. Ding, S.-Q. Yu, and Y.-H. Zhang, J Appl. Phys. **100**, 043502 (2006).

[61] H. A. Macleod, Thin-Film Optical Filter, 4th Edition, Taylor & Francis Group, 2010.

[62] Y.-S. Kuo, J. Becker, S. Liu, Y. Zhao, X.-H. Zhao, P.-Y. Su, I. Bhat, and Y.-H. Zhang, the Proceeding of the 42nd IEEE Photovoltaic Specialists Conference (2015).

[63] P. Pringsheim, Z. Phys. **57**, 739 (1929).

[64] R. Epstein, M. Buchwald, B. Edwards, T. Gosnell, and C. E. Mungan, Nature **377**, 500 (1995).

[65] J. Thiede, J. Distel, S. R. Greenfield, and R. I. Epstein, Appl. Phys. Lett. **86**, 154107 (2005).

[66] R. Epstein and M. Sheik-Bahae, Optical Refrigeration, Wiley-VCH, 2009.

[67] G. Nemova and R. Kashyap, Rep. Prog. Phys. **73**, 086501 (2010).

[68] C. Hoyt, M. Sheik-Bahae, R. Epstein, B. Edwards, and J. Anderson, Phys. Rev. Lett. **85**, 3600 (2000).

[69] J. Fernandez, A. Garcia-Adeva, and R. Balda, Phys. Rev. Lett. **97**, 033001 (2006).

[70] D. V. Seletskiy, S. D. Melgaard, S. Bigotta, A. D. Lieto, M. Tonelli and M. Sheik-Bahae, Nat. Photonics **4**, 161 (2010).

[71] S. D. Melgaard, D. V. Seletskiy, A. D. Lieto, M. Tonelli, and M. Sheik-Bahae, Opt. Lett. **38**, 1588 (2013).

[72] S. D. Melgaard, A. R. Albrecht, M. P. Hehlen and M. Sheik-Bahae, Scientific Reports **6** (2016).

[73] J. Zhang, D. Li, R. Chen and Q. Xiong, Nature **493**, 504 (2013).

[74] J.-B. Wang, S. R. Johnson, D. Ding, S.-Q. Yu, and Y.-H. Zhang, J. Appl. Phys. **100**, 043502 (2006).

[75] M. Sheik-Bahae and R. I. Epstein, Phys. Rev. Lett. **92**, 247403-1 (2004).

[76] H. Gauck, T. H. Gfroerer, M. J. Renn, E. A. Cornell, K. A. Bertness, Appl. Phys. A 64, **143** (1997).

[77] M. A. Green, Nature Energy, art no.15015 (2016).

[78] K. Masuko, et al., IEEE J. Photovoltaics, **4**, 1433 (2014).

[79] D. D. Smith, P. Cousins, S. Westerberg, R. D. J.-Tabajonda, G. Aniero, and Y.-C. Shen, IEEE J. Photovoltaics, **4**, 1465 (2014).

[80] W. Shockley and H. J. Queisser, J. Appl. Phys., **32**, 510 (1961).

[81] C. H. Henry, J. Appl. Phys., **51**, 4494 (1980).

[82] S. Essig, et al., IEEE J. Photovoltaics, **6**, 1012 (2016).

[83]J. Werner, C.-H. Weng, A. Walter, L. Fesquet, J. P. Seif, S. D. Wolf, B. Niesen, and C. Ballif, J. Phys. Chem. Lett., **7**, 161 (2016).

[84]C. M. S.-Fella, Y. Li, M. Amani, J. W. Ager, F. M. Toma, E. Yablonovitch, I. D. Sharp, and A. Javey, Nano Lett., **16**, 800 (2016).

[85] M. Gloeckler, the proceeding of the 43rd IEEE Photovoltaic Specialists Conference, 2016.

[86] A. Waag, F. Fischer, Th. Litz, B. Kuhn-Heinrich, U. Zehnder, W. Ossau, W. Spahn, H. Heinke, and G. Landwehr, J. Cryst. Growth **138**, 155 (1994).

APPENDIX A

THERMIONIC EMISSION INDUCED INTERFACE RECOMBINATION

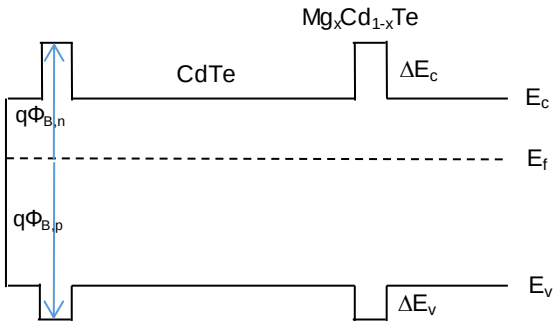

Fig. A.1. Band Diagram of CdTe/$Mg_xCd_{1-x}Te$ DH at Equilibrium.

Fig. A.1 shows the band diagram of CdTe/$Mg_xCd_{1-x}Te$ DH at equilibrium. The material is intrinsic n-type and thus the Fermi energy E_f at equilibrium is closer to the conduction band edge. ΔE_c and ΔE_v represent the conduction and valance band offset and $q\Phi_{B,n}$ and $q\Phi_{B,p}$ represent the potential difference between the equilibrium Fermi energy and the $Mg_xCd_{1-x}Te$ conduction and valance band edge.

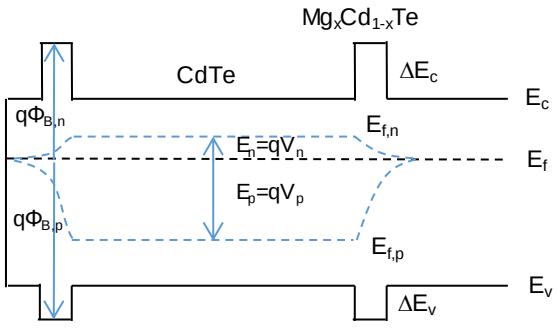

Fig. A.2. Band Diagram and Fermi Energies of CdTe/$Mg_xCd_{1-x}Te$ DH After Being Excited by a Laser Pulse.

Fig. A.2 shows Fermi energies CdTe/$Mg_xCd_{1-x}Te$ DHs after being excited by a laser pulse. Assume that the interface recombination velocity is sufficiently small so that the carriers can quickly distribute uniformly inside the CdTe layer. Thus, the electron and hole quasi-Fermi levels are flat in the CdTe layer. Assuming that carriers can quickly recombine when they reach the sample surface or bottom CdTe buffer layer, the quasi-Fermi level separation is then zero outside the CdTe/$Mg_xCd_{1-x}Te$ DH region. As carriers recombine, the quasi-Fermi level separation in the CdTe region will gradually decrease, until reaching zero when the sample reaches equilibrium state again.

From the classic thermionic emission theory [1], the current flows from the middle CdTe layer to the top or bottom layers are as shown below:

$$J_n = A^* T^2 \exp\left(-\frac{q\Phi_{B,n}}{kT}\right)\left(\exp\left(\frac{qV_n}{kT}\right) - 1\right) \tag{A.1}$$

$$J_p = A^* T^2 \exp\left(-\frac{q\Phi_{B,p}}{kT}\right)\left(\exp\left(\frac{qV_p}{kT}\right) - 1\right) \tag{A.2}$$

where A* is the Richardson constant.

$$A^* = \frac{4\pi q m_{e,h}^* k^2}{h^3} \tag{A.3}$$

J_n and J_p represents the electron and hole current density, respectively. The barrier potential ($q\Phi_{B,n}$ and $q\Phi_{B,p}$) limits the dark current and the quasi Fermi energy (qV_n and qV_p) act as a driving force to J_n and J_p. Under Boltzmann statistics:

$$\begin{aligned} J_n &= A^* T^2 \exp\left(-\frac{q\Phi_{B,n}}{kT}\right)\left(\exp\left(\frac{qV_n}{kT}\right) - 1\right) \\ &= A^* T^2 \exp\left(-\frac{\Delta E_c}{kT}\right)\exp\left(-\frac{E_c - E_f}{kT}\right)\left(\exp\left(\frac{qV_n}{kT}\right) - 1\right) \\ &= A^* T^2 \exp\left(-\frac{\Delta E_c}{kT}\right)\frac{n_0}{N_c}\left(\frac{n_0 + \Delta n}{n_0} - 1\right) \\ &= A^* T^2 \exp\left(-\frac{\Delta E_c}{kT}\right)\frac{\Delta n}{N_c} \end{aligned} \tag{A.4}$$

Since

$$R = \frac{\Delta n}{\tau_{therm,n}} = \frac{2J_n}{qd} = 2A^*T^2 \exp\left(-\frac{\Delta E_c}{kT}\right)\frac{\Delta n}{qdN_C} \tag{A.5}$$

Then

$$\tau_{therm,n} = \frac{qdN_c}{2A^*T^2 \exp\left(-\frac{\Delta E_c}{kT}\right)} = d\sqrt{\frac{\pi m_e^*}{2kT}}\exp(\frac{\Delta E_c}{kT}) \tag{A.6}$$

Similarly

$$\tau_{therm,p} = \frac{qdN_v}{2A^*T^2 \exp\left(-\frac{\Delta E_v}{kT}\right)} = d\sqrt{\frac{\pi m_h^*}{2kT}}\exp(\frac{\Delta E_v}{kT}) \tag{A.7}$$

It should be noted that $\tau_{therm,n}$ and $\tau_{therm,p}$ should have the same value, otherwise, charge can build up at the surface and bottom layers. Thus equation (A.6) and (A.7) may not be suitable in a real photoluminescence decay process. A more generalized equation should be in the following form, where ΔE should be a value between conduction and valance band offset.

$$\tau_{therm} = d\sqrt{\frac{\pi m^*}{2kT}}\exp(\frac{\Delta E}{kT}) \tag{A.8}$$

References:

[1] S. M. Sze, Physics of Semiconductor Devices, Third Edition, pp 154, John Wiley & Sons, Inc., Hoboken, New Jersey, 2007.

APPENDIX B

PHOTON RECYCLING & EXTRACTION FACTORS OF TEXTURED STRUCTURE

The below figure shows a solar cell structure with a Lambertian textured top surface. Assume a photon is emitted at a distance x from the top surface and at an angle θ relative to the direction normal to the surface. The escape probability from the front surface ($P_{e,f}$) of this particular photon is calculated in (B.1), considering that it can either travel in the top or to the bottom directions.

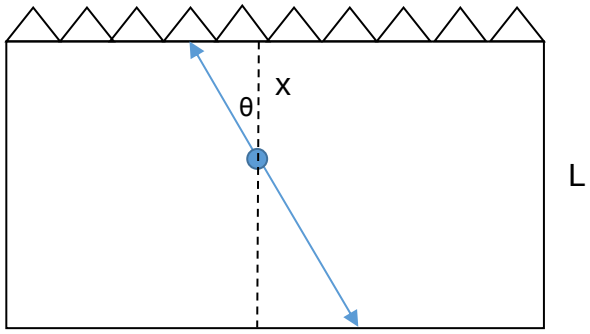

Fig. B.1. Schematic Diagram of a Solar Cell with Random Textured Surface.

$$P_{e,f} = \left(e^{-\alpha x/cos\theta} + R_b e^{-\alpha(2L-x)/cos\theta}\right) t_f \left[1 + r_f b + (r_f b)^2 + \cdots\right]$$
$$= \left(e^{-\alpha x/cos\theta} + R_b e^{-\alpha(2L-x)/cos\theta}\right) \frac{t_f}{1-r_f b} \quad \text{(B.1)}$$

where α is the absorption coefficient, L is the sample thickness, R_b is the back surface reflectance, t_f and r_f are the average front surface transmittance and reflectance, and b is the average probability of a photon to be able to travel from the top surface to the bottom surface and back to the top surface. (B.2), (B.3) and (B.4) show the calculation of t_f, r_f and b.

$$t_f = \frac{\int_0^{\pi/2} T_f cos\theta sin\theta d\theta}{\int_0^{\pi/2} cos\theta sin\theta d\theta} \quad \text{(B.2)}$$

$$r_f = \frac{\int_0^{\pi/2} R_f cos\theta sin\theta d\theta}{\int_0^{\pi/2} cos\theta sin\theta d\theta} \tag{B.3}$$

$$b = \frac{\int_0^{\pi/2} R_b e^{-2\alpha L/cos\theta} cos\theta sin\theta d\theta}{\int_0^{\pi/2} cos\theta sin\theta d\theta} \tag{B.4}$$

The front surface photon extraction factor ($\gamma_{e,f}$), is calculated in (B.5), by taking the average of the escape probability ($P_{e,f}$) of each photon.

$$\gamma_{e,f} = \frac{\iiint \hat{S}(E) P_{e,f} sin\theta d\theta d\varphi dE dx}{\int d\Omega \int dx} \tag{B.5}$$

$$= \int_0^{\infty} \hat{S}(E) \int_0^{\pi/2} \frac{t_f}{1-r_f b} \frac{(1-e^{-\alpha L/cos\theta})(1+R_b e^{-\alpha L/cos\theta})}{2\alpha L} cos\theta sin\theta d\theta dE$$

where $\hat{S}(E)$ is the normalized luminescence spectrum, φ is the azimuth angle, E is the photon energy, Ω is the solid angle and $sin\theta \cdot d\theta \cdot d\varphi$ is the derivative of solid angle.

Similarly, the re-absorption probability of a photon at a distance x from the top surface can be calculated as shown in (B.6) and (B.7), where $P_{abs,1}$ and $P_{abs,2}$ are for the photons traveling in the top and bottom directions respectively.

$$P_{abs,1} = \left(1 - e^{-\alpha x/cos\theta}\right) + e^{-\alpha x/cos\theta} r_f (a_1 + a_2)[1 + r_f b + \left(r_f b\right)^2 \dots] \tag{B.6}$$

$$= \left(1 - e^{-\alpha x/cos\theta}\right) + e^{-\alpha x/cos\theta} \frac{r_f (a_1 + a_2)}{1 - r_f b}$$

$$P_{abs,2} = \left(1 - e^{-\alpha (L-x)/cos\theta}\right) + e^{-\alpha (L-x)/cos\theta} R_b \left(1 - e^{-\alpha L/cos\theta}\right) \tag{B.7}$$

$$+ e^{-\alpha (2L-x)/cos\theta} R_b r_f (a_1 + a_2)[1 + r_f b + \left(r_f b\right)^2 \dots]$$

$$= \left(1 - e^{-\alpha (L-x)/cos\theta}\right) + e^{-\alpha (L-x)/cos\theta} R_b \left(1 - e^{-\alpha L/cos\theta}\right) +$$

$$e^{-\alpha (2L-x)/cos\theta} R_b \frac{r_f (a_1 + a_2)}{1 - r_f b}$$

a_1 and a_2 are the absorption probability of a photon when it is traveling from the top to the bottom surface and from the bottom to top surface respectively.

$$a_1 = \frac{\int_0^{\pi/2}(1-e^{-\alpha L/cos\theta})cos\theta sin\theta d\theta}{\int_0^{\pi/2} cos\theta sin\theta d\theta} \tag{B.8}$$

$$a_2 = \frac{\int_0^{\pi/2} e^{-\alpha L/cos\theta} R_b(1-e^{-\alpha L/cos\theta})cos\theta sin\theta d\theta}{\int_0^{\pi/2} cos\theta sin\theta d\theta} \tag{B.9}$$

The photon recycling factor γ_r is calculated by taking the average re-absorption probability of every photon as shown in (B.10).

$$\begin{aligned}\gamma_r &= \frac{\iiint \hat{S}(E)P_{abs} sin\theta d\theta d\varphi dE dx}{\int d\Omega \int dx} \\ &= 1 - \int_0^{\infty} \hat{S}(E) \int_0^{\pi/2} \frac{1-e^{-\alpha L/cos\theta}}{2\alpha L} \{2 - R_b - \frac{r_f(a_1+a_2)}{1-r_f b} \\ &\quad -R_b e^{-\alpha L/cos\theta}[\frac{r_f(a_1+a_2)}{1-r_f b} - 1]\} cos\theta sin\theta d\theta dE\end{aligned} \tag{B.10}$$